THE DEVELOPMENT OF A SIMPLIFIED MODELING TECHNIQUE FOR THE FINITE ELEMENT ANALYSIS OF REINFORCED MASONRY SHEAR WALLS

By

MOHAMMED IBRAHEM ABDELLATEF

A thesis submitted in partial fulfillment of
the requirements for the degree of

MASTER OF SCIENCE IN CIVIL ENGINEERING

WASHINGTON STATE UNIVERSITY
Department of Civil and Environmental Engineering

DECEMBER 2011

To the Faculty of Washington State University:

The members of the Committee appointed to examine the thesis of MOHAMMED IBRAHEM ABDELLATEF find it satisfactory and recommend that it be accepted.

William F. Cofer, Ph.D., Chair

David I. McLean, Ph.D.

James D. Dolan, Ph.D.

ACKNOWLEDGEMENT

I would like to express my sincere gratitude to Dr. William Cofer, my advisor and committee chair, for introducing me and Finite Element Analysis to each other, and adding it to my interests and research experience, and providing me with his knowledge, patience, time, advice, and guidance throughout this work.

I would like also to thank my committee members, Dr. David McLean and Dr. Daniel Dolan, for supporting me at several occasions, and for giving me some of their time for discussion when I asked for.

I would like also to thank my colleague, Jacob Sherman, for providing me with his testing data when I asked for. His first set of data showed me the right path to complete my work. I hope I did not overload him my many emails.

I would like also to thank all faculty members at WSU, who taugh to me or I worked with. They made me feel more than being comfortable; such that I felt I did not left my lovely hometown, Alexandria.

I extend a very special thank you to my family and friends, who have always believed in me, encourage me, and supported me.

Finally, I want to dedicate this work to the souls of brave Egyptian people, who were murdered while participating in the 25th January peaceful revolution.

THE DEVELOPMENT OF A SIMPLIFIED MODELING TECHNIQUE FOR THE FINITE ELEMENT ANALYSIS OF REINFORCED MASONRY SHEAR WALLS

Abstract

By Mohammed Ibrahem AbdElLatef, M.S.
Washington State University
December 2011

Chair: William F. Cofer

Reinforced masonry shear walls are structural elements that are commonly used in construction. It is important to properly model their contribution to the strength and stiffness of the structures in which they appear. Analysts typically represent these shear walls with deep beam elements within building models. However, the assumption that a shear wall behaves as a deep beam breaks down when shear failure occurs, and cracking starts to dominate the behavior of the wall. There is a need to develop a finite element model of these shear walls that is accurate but simple enough to be included as a part of a full building model.

A 2-D masonry shear wall model was developed to meet these requirements. To make it applicable within standard structural analysis software, the model does not require a detailed representation of each component of the wall separately. Instead, the reinforcing is smeared and overlaid with a plane stress masonry element. Plasticity is assumed for the steel and cracking/damage is assumed for the masonry. Reductions in masonry stiffness were applied to account for initial cracks, and artificial damping was added to stabilize the solution process after the occurrence of masonry damage.

Data from two experimental test programs were used to verify the proposed modeling technique along with comparisons with detailed finite element models. It was found that the behavior of the simplified models was quite close to that of the detailed finite element models for all cases considered. When compared to the peak values of cyclic load of the experimental specimens, it was found that initial stiffness, peak load, and displacement at final failure were well

predicted although, for short shear walls which are dominated by shear failure of the masonry, damage did not evolve as rapidly in the finite element models as was observed in the experimental specimens. The proposed modeling technique was therefore shown to reasonably predict reinforced masonry shear wall behavior, even with coarse meshing and smeared steel reinforcement, regardless of the wall aspect ratio, amount of axial vertical load applied to the wall, and reinforcement ratio.

TABLE OF CONTENTS

Page

LIST OF TABLES

Page

LIST OF FIGURES

Page

List of Symbols

A_{cr} Cracked Area of Masonry Section (in^2)

A_s Total Steel Area (in^2)

A_{sb} Area of Single Steel Bar (in^2)

A_{sx} Area of Reinforced Steel in X-Direction (in^2)

A_{sy} Area of Reinforced Steel in Y-Direction (in^2)

b Masonry Wall Width (in)

b' Smeared Steel Element Width (in)

$[C]$ Damping Matrix

d Depth of Steel Reinforcement Measured from Top Compression Fibers (in)

E_{eq} Equivalent Masonry Modulus of Elasticity (psi)

E_m Masonry Modulus of Elasticity (psi)

E_{sx} Equivalent Smeared Steel Modulus of Elasticity in X-Direction (psi)

E_{sy} Equivalent Smeared Steel Modulus of Elasticity in Y-Direction (psi)

E_s Steel Modulus of Elasticity (psi)

EI Flexural Stiffness

e Reinforcement Steel Bars Edge Distance (in)

f_m Compressive Stress in Masonry Top Fibers (psi)

f_m' Compressive Stress of Masonry Prism (psi)

f_s Tensile Stress of Steel Reinforcement (psi)

f_t Maximum Tensile Stress of Masonry (psi)

f_u Ultimate Steel Stress (psi)

f_y Yielding Steel Stress (psi)

H_B Concrete Beam Height (in)

H_L Masonry Wall Loading Height (in)

H_w Masonry Wall Height (in)

h_x' Smearing Width for X-Direction Steel (in)

h_y' Smearing Width for Y-Direction Steel (in)

I Dimensionless Constant Defined by Equation 7

I_{cr} Cracked Moment of Inertia of the Wall (in^3)

I_{eff} Effective Moment of Inertia of the Wall (in^3)

I_g Gross Moment of Inertia of the Masonry Wall (in^3)

I_g' Gross Moment of Inertia of the FE Model (in^3)

I_s Steel Bars Moment of Inertia (in^3)

I_s' Smeared Steel Moment of Inertia (in^3)

J Dimensionless Constant Defined by Equation 18

K Dimensionless Constant Defined by Equation 23

$[K]$ Stiffness Matrix

K_{sx} Equivalent Stiffness of X-Direction Steel (lb/in)

K_{sy} Equivalent Stiffness of Y-Direction Steel (lb/in)

L_w Masonry Wall Length (in)

L_x Element Length X-Direction (in)

L_y Element Length Y-Direction (in)

$[M]$ Mass Matrix

M_a Applied Moment ($lb.in$)

M_{cr} Cracking Moment ($lb.in$)

M_y Yielding Moment ($lb.in$)

N No. of Vertical Steel Bars

n Modeler Ratio

P Total Axial Load on the Wall, Including Own Weight (lb)

P_{sx} Axial Load in Equivalent X-Direction Spring (lb)

P_{sy} Axial Load in Equivalent Y-Direction Spring (lb)

S Vertical Steel Bars Spacing (in)

w_m Masonry Unit Weight (pcf)

x Position of the Neutral Axis Measured From Compression Top Fibers (in)

α_c Ratio of Mass Damping

α_m Coarse Meshing Masonry Scaling Factor

α_s Smeared Steel Scaling Factor

α_{sx} X-Direction Smeared Steel Scaling Factor

α_{sy} Y-Direction Smeared Steel Scaling Factor

β Stiffness Modification Factor

β_c Ratio of Stiffness Damping

Δ_x X-Direction Displacement (in)

Δ_y Y-Direction Displacement (in)

ε_m Compressive Stain in Masonry at the Top Fibers

ε_s Tensile Stain of Steel

ε_u Ultimate Steel Strain

ε_X X-Direction Strain

ε_Y Y-Direction Strain

ε_y Yielding Steel Strain

ν Poisson ratio

ρ_{VL} Vertical Steel Reinforcement Ratio

ρ_x' X-Direction Steel Reinforcement Ratio for Smearing Area

ρ_y' Y-Direction Steel Reinforcement Ratio for Smearing Area

σ_{sx} X-Direction Stresses in Smeared Steel (psi)

σ_{sy} Y-Direction Stresses in Smeared Steel (psi)

σ_x X-Direction Stresses in Masonry (psi)

σ_y Y-Direction Stresses in Masonry (psi)

CHAPTER ONE

INTRODUCTION

1.1 Historical Background

Since ancient times, masonry has been a common construction material for many types of structures, including buildings and bridges. This may be easily seen in the structures that remain from antiquity, such as those of the Romans. Although their construction might seem elementary, a good engineering sense was needed to design structures that have only compression internal forces, such as arched structures, since masonry does not have significant tensile resistance.

Masonry is still widely used in the U.S. as the basis of many structural elements, such as beams, columns, and walls. In order to enhance the tensile behavior and ductility of masonry structures, steel reinforcement is used to resist tensile stresses.

1.2 Masonry Wall Construction

In order to understand the behavior of masonry walls, it is necessary to discuss the elements that are used to construct the wall itself. Typically, masonry walls are composed of the following: masonry units, mortar joints, grout, and steel reinforcement, as shown in Figure 1.1 (Klingner, 2010)

1.2.1 Masonry Units

Masonry units are considered to be the main item in the wall composition. They are used to fill the space that is required to be filled architecturally and they provide the major contribution to the required compressive strength for resisting the structural loads. There are many types of these units. Examples include clay masonry units, which are formed from clay and sedimentary minerals with a compressive strength that varies from 1200 to 30,000 psi, and concrete masonry units, which are formed from zero-slump concrete with a compressive strength of 1500 to 3000 psi. (Klingner, 2010)

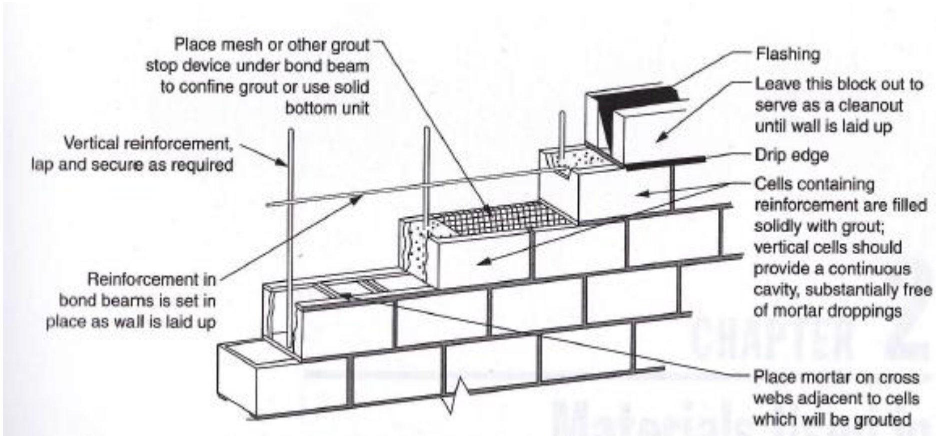

Figure 1.1 Basic Structural Configuration of Reinforced masonry walls (Klingner, 2010)

1.2.2 Mortar Joints

Mortar joints are used to hold masonry units together and also apart from each other due to dimensional tolerances. Horizontal joints are called bed joints and vertical joints are called head joints. There are three types of cementitious systems used as masonry mortar: Cement-Lime mortar, Masonry-Cement mortar, and Mortar-Cement mortar (Klingner, 2010). Mortar types are classified as: Type M which has high compressive and tensile bond strength, Type S which has moderate compressive and tensile bond strength, Type N which has low compressive and tensile bond strength, and Type O which has very low compressive and tensile bond strength. (Klingner, 2010)

1.2.3 Reinforcement

Reinforcement bars are used in masonry construction to resist tensile stress in the wall and increase wall ductility and resistance against vertical and lateral loads due to wind and earthquakes. Several kinds of reinforcement are commonly used: steel deformed bars, as shown in Figure 1.2(a), joint reinforcement, deformed reinforcing wires, steel welded wire reinforcement, as shown in Figure 1.2(b), and steel pre-stressing strands, as shown in Figure 1.2(c) (Klingner, 2010).

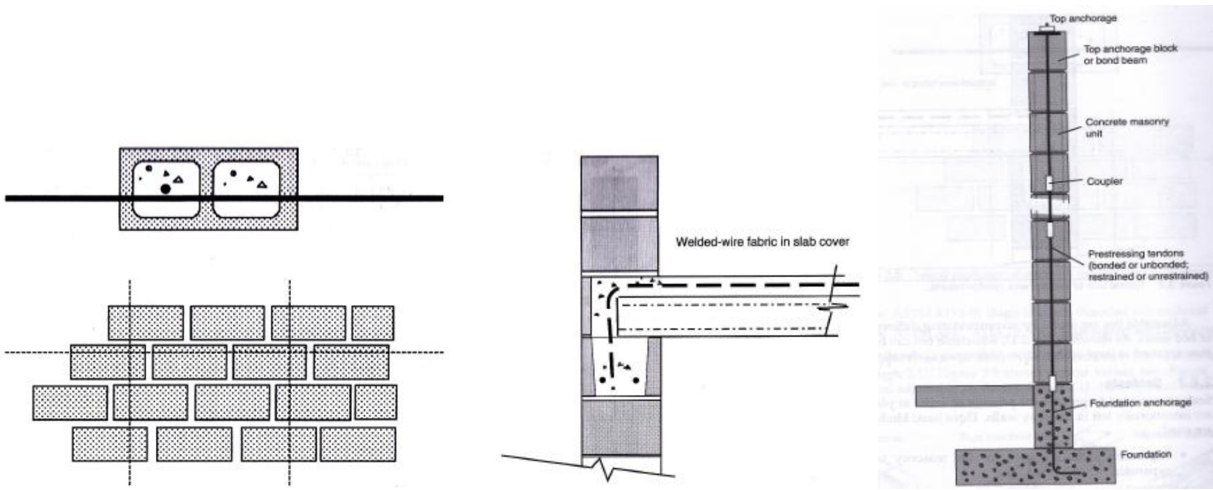

(a) (b) (c)

Figure 1.2 Typical Reinforcement in Masonry Walls (Klingner, 2010)

1.2.4 Grout

Grout is a cementitious fluid composed of Portland cement, sand, and pea gravel. It is used as a fluid to fill spaces in masonry and to surround reinforcement bars in order to enhance bond characteristics. (Klingner, 2010)

1.3 Masonry Research

As with any construction material, many studies have focused on the behavior of the masonry itself, and also on that of masonry structures.

1.3.1 Experimental Research

Early studies on masonry focused on the general behavior of either the masonry as a composite of several materials, or on each of its components separately. There are many uncertainties about the behavior of the individual masonry constituents. Therefore, the overall failure criteria for masonry structures are very complicated as their performance involves the interaction of several different components.

Other studies have focused on the behavior of masonry structures, especially masonry walls. These kinds of studies focused on the effect of wall dimensions and the use of different types of masonry, mortar, and/or grout on the bending and shear behavior of the wall, as is discussed in Chapter 2.

1.3.2 Modeling Research

In parallel with experimental studies, many models have been proposed to simulate the behavior of masonry materials and/or structures. These models have been formulated from different theoretical bases, including fracture energy, damage mechanics, and plasticity.

In general, there are two main approaches for the modeling of masonry structures: 1) to model each component of masonry separately, which is called micro modeling, and 2) to model the masonry structures using one equivalent material, which is called macro modeling.

1.4 Research Objectives

The main objective of this research is to simplify the nonlinear finite element modeling of masonry walls. The modeling simplification was based on two ideas, which are:

1) Developing a consistent approach for the masonry material in order to use it in macro-modeling, and
2) Using smeared reinforcing steel instead of discrete bars.

Also, coarse meshing and a relatively large time steps are considered in order to decrease the time and effort of analysis. The overall intent is to provide an accurate, but simplified, representation of reinforced masonry shear walls that can be used as part of a larger model of an entire structure.

CHAPTER TWO

LITERATURE REVIEW

2.1 Introduction

Although research on masonry started early in the twentieth century, there is great variation in the results of each research study, especially regarding the masonry material behavior itself. The reason is that masonry structures are constructed from different materials and the fact that the construction procedure itself leads to high variance due to human involvement. The main objective of this chapter is to review the previous work done in the following fields: 1) Masonry material behavior, 2) Masonry wall general behavior, and 3) modeling of masonry structures.

2.2 Masonry failure behavior

Failure behavior of masonry is very complicated and different from most other composite materials. Unlike other materials, failure of masonry can be caused by mortar joint failure, which is more like micro scale failure, or crushing of masonry units along with mortar, which is more like macro scale failure. This unique behavior implies that the general performance of masonry is strongly affected by the orientation of masonry and mortar, in addition to the behavior of the components. This leads to anisotropic behavior for masonry.

Many studies have focused on the in-plane behavior of concrete masonry under biaxial tension-compression, especially grouted masonry. The main conclusion was that grouted concrete masonry behaves as an anisotropic material, the properties of which depend on bed joint orientation (Drysdale and Khattab, 1995). However, this anisotropic behavior does not have a significant effect on the macro-scale behavior (Karapitta et al., 2011), so it can be reasonably represented as being orthotropic, similar to the orthotropic behavior of concrete.

2.2.1 Compressive behavior of masonry

The compressive behavior of masonry is very complicated because of the interaction of different materials, each having individual failure mechanisms. In order to monitor this behavior, masonry prisms with the same construction are often used. The major contribution to compressive resistance comes from the blocks, but there are other factors that also affect the compressive resistance, such as: block geometry, height to thickness ratio of the block, mortar bedding, and thickness of the mortar joint (Ramamurthy et al., 2000). Also, load eccentricity has a great effect on the compressive behavior, which increases with a decrease of the block solid percentage (Drysdale and Hamid, 1983).

In many studies, researchers attempted to idealize the compressive stress-strain curves for different types of masonry with different conditions: grouted, hollow, confined, and/or unconfined [(Priestley, 1986), (Cheema and Klingner, 1986), (Barbosa and Hanai, 2009)]. The results showed significant variation, as shown in Figures 2.1 and 2.2, due to the existence of different failure mechanisms of the concrete masonry prisms, which are: block splitting, block crushing, and mortar crushing (Cheema and Klingner, 1986).

One of the most common representations for grouted concrete masonry is a modification of the Kent-Park concrete curve, as shown in Figure 2.3 (Priestley and Elder, 1983), which has shown close agreement with test data. This approach was adopted by many authors in their studies after it was presented [(Priestley, 1986),(El-Metwally et al., 1991),(Dhanasekar and Shrive, 2002)].

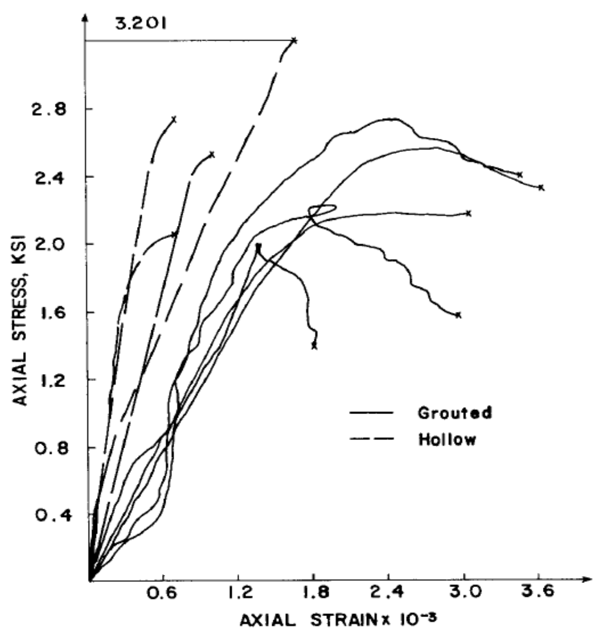

Figure 2.1 Experimental stress-stain curves for grouted/hollow concrete masonry (Cheema and Klingner, 1986)

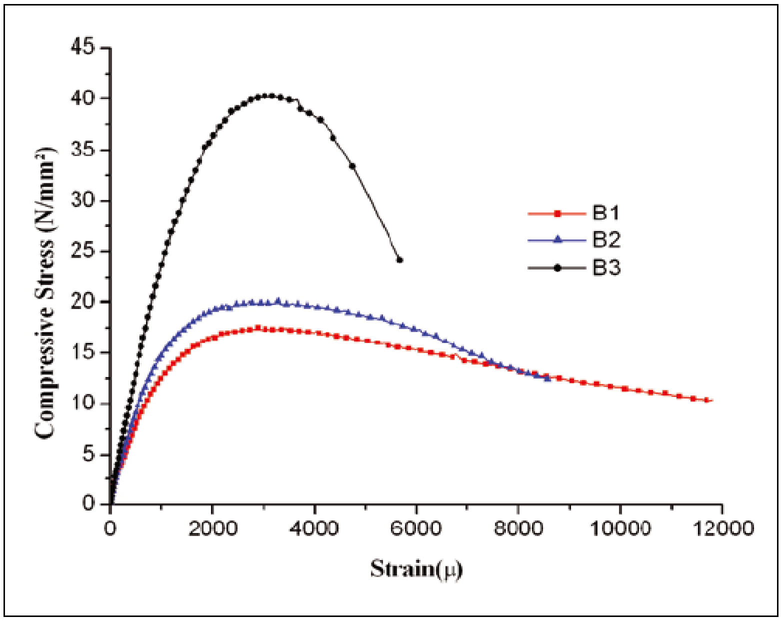

Figure 2.2 Experimental stress-stain curves for hollow concrete blocks (Barbosa and Hanai, 2009)

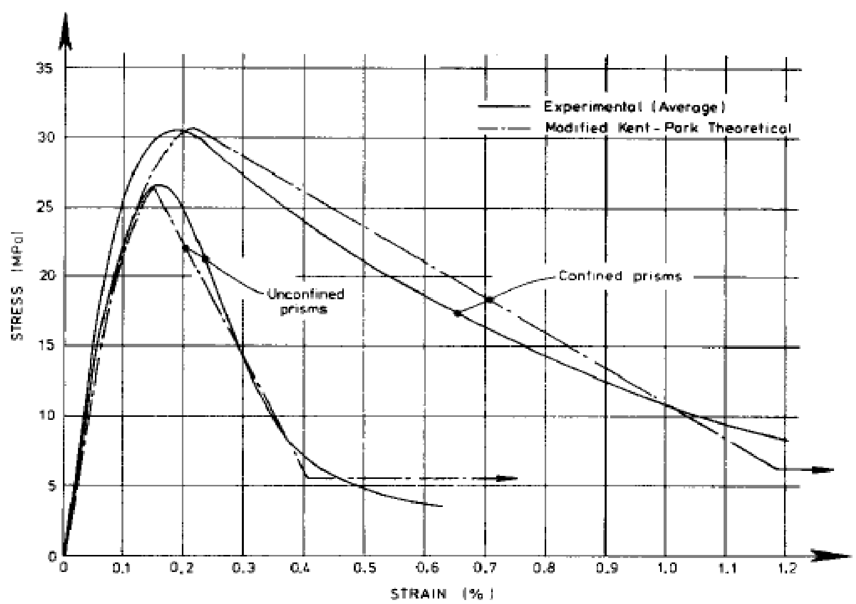

Figure 2.3 Experimental stress-stain curves for confined/unconfined concrete masonry compared to modified Kent-Park (Priestley, 1986)

2.2.2 Tensile Behavior of Masonry

Masonry has very low tensile strength, such that it can be ignored. Tensile behavior is mainly governed by mortar joint splitting. As the setup of a test is nearly impossible, no significant research has been done to monitor the tensile stress-strain behavior of masonry prisms using a direct tensile test. Most authors use the tensile stress-strain curve proposed for concrete (Haach et al., 2011), having both ascending and softening parts, with much lower tensile resistance as recommended by codes (Horton and Tadros, 1990) or obtained from indirect tensile tests (Drysdale et al., 1979).

2.3 Masonry Wall Lateral Behavior

The behavior of masonry walls can be described from the perspective of micro or macro behavior. The macro approach is most convenient for studying the overall behavior of the wall because it considers the wall as being constructed of one homogenous material. On the other hand, with the micro approach, the behavior of the wall is represented through localized cracking/crushing of the masonry units and failure at mortar joints. This approach is suitable for small structures, but it becomes very complicated with large ones.

2.3.1 In-Plane Behavior

The total lateral deformation of a masonry wall is the summation of four distinct mechanisms: base sliding, overall shear distortion, apparent flexural deformation which includes the base uplift due to bond slip and elongations of vertical steel, and flexural deformation calculated from section curvature, as shown in Figure 2.1. (Shing et al., 1990)

It is very difficult to measure the bond slip of the wall, so it is not usually possible to isolate the base uplift from the total flexural displacement. In reality, because it is very difficult to calculate the flexural deformation, it is usually obtained experimentally by subtracting shear base sliding and shear distortion from total displacement. For some cases, base sliding is insignificant, so it can be ignored for theoretical calculations of flexural displacement. However, in the case of low rise walls, it usually has a significant effect on overall displacement. (Shing et al., 1990)

For shear deformation calculations, the wall panel can be considered as a linear elastic section with the effect of reinforcement on shear stiffness being negligible until the occurrence of cracks. After flexural and shear cracks occur, shear stiffness experiences significant degradation, with horizontal and vertical reinforcement forming a truss mechanism to resist applied load. Once a major crack away from the main diagonal has occurred, a diagonal strut mechanism starts to resist the applied load (Shing et al., 1990).

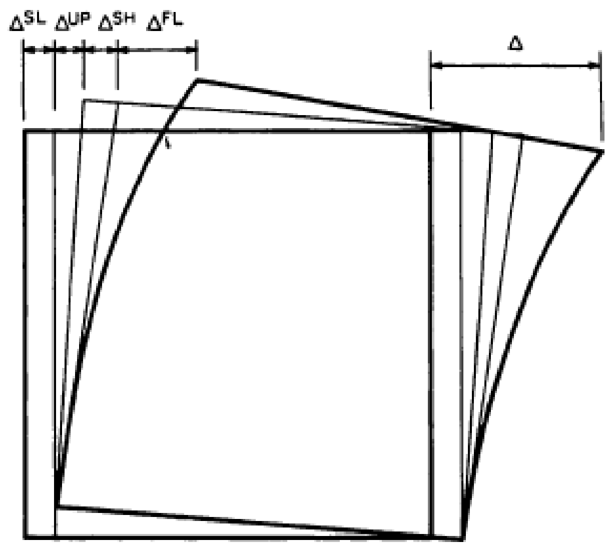

Figure 2.1 Reinforced Masonry Wall Deformation mechanisms (Shing et al., 1990)

Although these mechanisms describe clearly the behavior of the wall at the macro level, the eccentricity of the applied load could change the failure criteria at the micro level. The failure mode of the masonry could change from splitting of mortar joints to crushing when the applied vertical load has an out of plane eccentricity of about 1/20 of the thickness.(Hatzinikolas et al., 1980)

2.3.2 Out-of-Plane Behavior

Although it is not very common to load a masonry wall with out-of-plane loads, some researchers have studied this kind of behavior. In general, masonry walls act like shells under this kind of loading. The failure mode in this case is ductile, characterized by yielding of the reinforcement with spalling of the mortar and face shells on the compression face at the ultimate load. It has been noticed that grout affects the cracking capacity, while the vertical reinforcement ratio affects the ultimate capacity.(Abboud et al., 1996)

2.4 Modeling of Masonry walls

Many studies have focused on the different methods for modeling masonry structures but, as mentioned earlier, these studies can be categorized under two main approaches: Micro-Modeling and Macro-Modeling. In micro-modeling, it is considered as a discrete assembly of units with different, while in properties macro-modeling, masonry is considered to be a homogenous material with equivalent properties (Haach et al., 2011).

2.4.1 Micro-Modeling

Micro-modeling is the most common technique used for small structures and/or for studying the effect of each component's local failure mechanisms on the general behavior. It can be simply described as discretizing each component of the model, and using different elements and constitutive models for each one.

The same concept is used in masonry modeling, but it is not applicable to large structures due to the relatively small dimensions of the masonry and mortar compared with those of the structure, which requires a very fine mesh. The main elements used in this kind of modeling are masonry elements, mortar joint elements, and masonry-mortar interface elements.

However, most researchers do not apply such detail for their micro-modeling because it requires a very fine mesh due to the very small thickness of the mortar joints. The most common approach for the discretization is to use two different types of elements, one for the masonry units and mortar joints, as a homogenous material, and the other as zero thickness interface elements for potential cracks [(Loureco and Rots, 1997),(Gambarotta and Lagomarsino, 1997),(Chaimoon and Attard, 2007), (Da Porto et al., 2010), (Haach et al., 2011)]. With this approach, the effort required for computation is reduced because of the ability to use a coarser mesh.

Typically, the micro-modeling technique allows the use of different mechanical assumptions for materials, such as damage models (Gambarotta and Lagomarsino, 1997), cap models (Loureco and Rots, 1997), and/or fracture models (Chaimoon and Attard, 2007), to study the behavior of masonry , with monotonic (Haach et al., 2011) or cyclic loading (Da Porto et al., 2010).

2.4.2 Macro-Modeling

The macro-modeling approach is the most common technique used for large structures and/or for studying the effect of global parameters, such as compressive strength, reinforcement ratio, and structure dimensions, on the general structural behavior. It can be simply described as modeling the overall structure with one homogeneous material, which has properties that are equivalent to the sum of its components.

This method is convenient for both analytical and numerical modeling because it does not require the level of detailed discretization used for micro-modeling, which is based on individual material components.

2.4.2.1 Macro-Modeling for Concrete.

Macro-modeling is very common for concrete structures because it is very difficult to model the aggregates and the cementitious components separately. Many researchers have proposed constitutive relations and failure criteria for concrete [e.g. Modified compression field theory (Vecchio and Collins, 1986)] and have used these to model and predict the behavior of various concrete structures [e.g., (Vecchio, 1990), (Selby and Vecchio, 1997), (Vecchio and Selby, 1991)].

In addition, reinforcement has been treated on the macro-scale as individual embedded elements within concrete elements (Yamaguchi and Ohta, 1993) or through smearing the reinforcement properties within concrete elements (Kazaz et al., 2006).

Finally, for most studies, the smeared crack model has been used for equivalent cracking behavior (Balakrishnan and Murray, 1988), which can be developed with fracture energy (Feenstra and De Borst, 1995) in order to achieve mesh size independence.

2.4.2.2 Macro-Modeling for Masonry.

In parallel with the aforementioned concrete studies, many researchers have attempted to model masonry structures at the macro level. However, unlike concrete, macro-modeling of masonry structures is very complicated because of their anisotropic nature and the local failure mechanisms that govern their global failure.

As previously mentioned, both analytical and numerical models can be developed with macro-modeling. Analytical modeling is usually used to predict the general behavior of simple structures with simple types of loads. For example, Horton and Tadros (1990) used various approaches and methods for estimating effective stiffness, including the ACI formula for concrete, in order to calculate the deflection of masonry flexural members. El-Metwally et al. (1991) used a model of an equivalent plane strain beam column to model a strip of masonry wall subjected to eccentric uniform load. The predicted capacity was found to be very sensitive to end eccentricity, especially in short walls.

For more sophisticated structures and loading, numerical analysis based on the finite element method is used. For example, Afshari and Kaldjian (1989) used finite element analysis to predict the failure envelope for masonry walls. They used 8-node three dimensional elements for the wall, and they assumed linear analysis for brittle cementitious materials such as blocks, grout, and mortar. The proposed failure envelope, which is based on basic strength and geometric characteristic values of mortar joints and masonry units, showed good agreement with experimental results. Loureco et al. (1998) developed a continuum model for masonry. The model was based on orthotropic elasto-plasticity, such that uniaxial tension and compression behavior could be described. Two main failure mechanisms were assumed: localized and distributed fracture. Mojsilovic and Marti (1997) presented a sandwich model to predict the strength of masonry wall elements subjected to combined in-plane forces and moments. Legeron et al. (2005) used a finite element analysis based on multilayer elements with damage mechanics to model monotonic and cyclically loaded reinforced concrete structures. Sutcliffe et al. (2001) used the lower bound theory of classical plasticity to estimate the lower bound load of unreinforced masonry shear walls. Asteris and Tzamtzis (2003) developed a yielding surface, as a failure criterion, for macro-modeling of masonry walls. El-Dakhakhni et al (2006) used a multilaminate model for concrete masonry walls. The masonry was modeled as a homogenous medium, overlaid with two sets of planes of weakness, representing head and bed joints, and two sets of reinforcement. The effects of weakness planes and reinforcement were smeared within the masonry elements. Stavridis and Shing (2010) modeled masonry-infilled RC Frames considering a combination of the smeared and discrete crack approaches in order to capture the different failure modes. Karapitta et al (2011) used explicit dynamic analysis to model the cyclic behavior of unreinforced masonry. A micro-model was used based on a coaxial-total-based rotation smeared crack model. A material constitutive law based on fracture energy was also proposed.

CHAPTER THREE

DISCRETIZED STEEL MODEL

3.1 Introduction

In this chapter, the modeling of a masonry wall through the application of a macro approach with coarse meshing and smeared cracking for the masonry material and discretized axial elements for steel reinforcement is described. Although this model requires a high level of detail due to the representation of steel as a set of discretized axial elements, it is required to validate the modeling technique. The idea presented in this chapter is to scale the masonry constitutive relations so that they represent the stiffness degradation of the masonry wall due to crack propagation.

3.2 Material Assumptions

Within the modeling process, the constitutive relations of masonry at the macro scale and the model for the reinforcing steel have significant effects on the final results. The material assumptions used in the modeling are discussed in this section.

3.2.1 Masonry

As discussed in Chapter 2, the macro behavior of masonry is similar to the behavior of concrete in tension and compression. The initial tangent modulus of elasticity of masonry can be estimated as in Equation 1 (Holm, 1987), where a unit weight of 125 pcf is used, which is in a format similar to that for the initial tangent modulus of elasticity of concrete.

$$E_m = 22 * w_m^{1.5} * \sqrt{f_m'} \qquad [1]$$

In this research, the overall stress-strain curve of masonry is assumed to be a horizontal (strain) scaling of the stress-strain curve of concrete, with the scaling factor equal to the ratio of their initial tangent moduli of elasticity for the same stress, as shown in Figure 3.1.

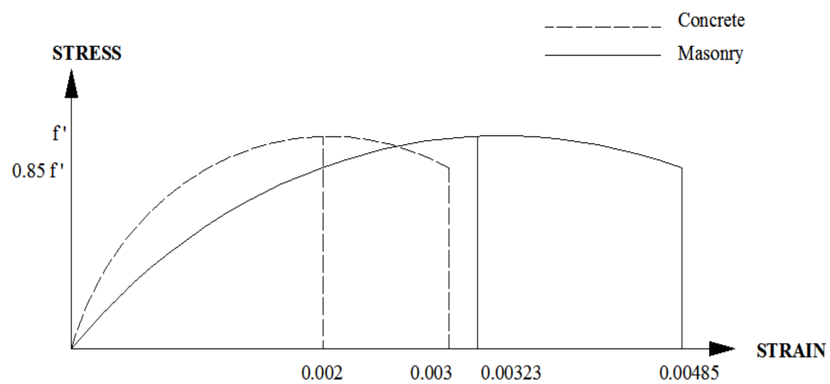

Figure 3.1 Scaling Relation of Stress-Strain in Compression between Masonry and Concrete

Also, tensile behavior is assumed to be the same as that of concrete, as shown in Figure3.2, with the same scaling as that used for compression. The ultimate cracking stress is reported to vary from $\sqrt{f_m'}$ to $5\sqrt{f_m'}$ (Horton and Tadros, 1990), based on masonry type, mortar, and grouting. The limit used in Equation 2 was recommended by the Uniform Building Code (Horton and Tadros, 1990).

$$f_t = 2.5\sqrt{f_m'} \qquad [2]$$

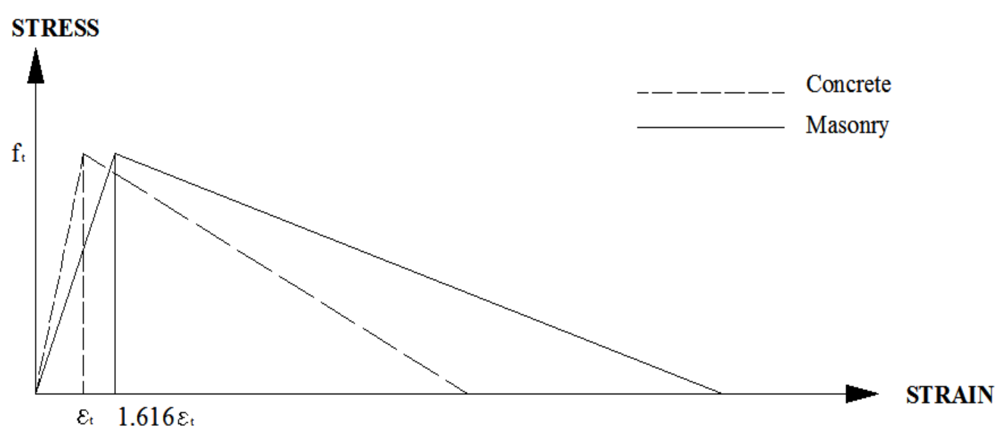

Figure 3.2 Scaling Relation of Stress-Strain in Tension between Masonry and Concrete

3.2.2 Reinforcement Steel

The constitutive relation used for steel is a bilinear representation with strain hardening, as shown in Figure 3.3. The ultimate strain is assumed to be 0.021, based on the tangent intersection of the typical stress-strain curves at the design ultimate stresses for most kinds of steel (Nilson, 1987).

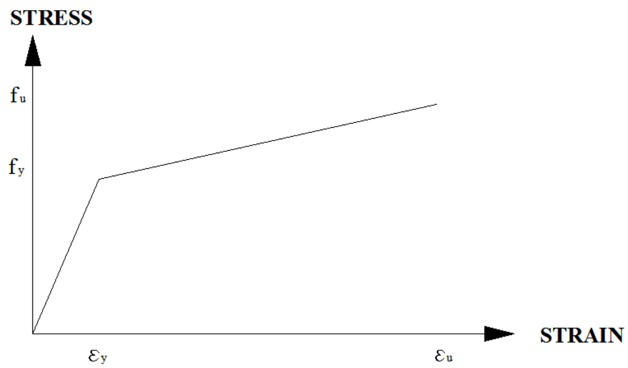

Figure 3.3 Bi-Linear Stress-Strain Representation of Reinforcement Steel

3.3 Scaling Technique

The technique proposed in this chapter can be simply described as scaling the constitutive relation by a factor, α_m, to represent the effect of cracking on stiffness of the masonry material when modeling a reinforced masonry wall. Because the tensile and compressive failure of masonry is dominated by limits of stress, the scaling factor was applied to strains, as shown in Figures 3.4 and 3.5.

Figure 3.4 Stress-Strain of Masonry in Compression for a Coarse Mesh

Figure 3.5 Stress-Strain of Masonry in Tension for a Coarse Mesh

3.3.1 Scaling due to Material Behavior

The scaling factor α_m is the reduction required to be applied to the initial modulus of elasticity acting with the gross overall moment of inertia of the wall, such that the flexural stiffness is equivalent to the initial modulus of elasticity acting on the cracked moment of inertia of the wall. This approach is necessary to properly consider the reduction in stiffness due to initial cracking of the wall, which is not considered in a finite element model. The reduction factor is defined on the basis of a cracked wall cross section.

Typically, masonry wall test specimens can be loaded through a concrete loading beam, as shown in Figure 3.6(a), or the load can be applied directly to the wall, as shown in Figure 3.6(b). For typical cantilever masonry walls, the cracked cross section of the base at working load is shown in Figure 3.7.

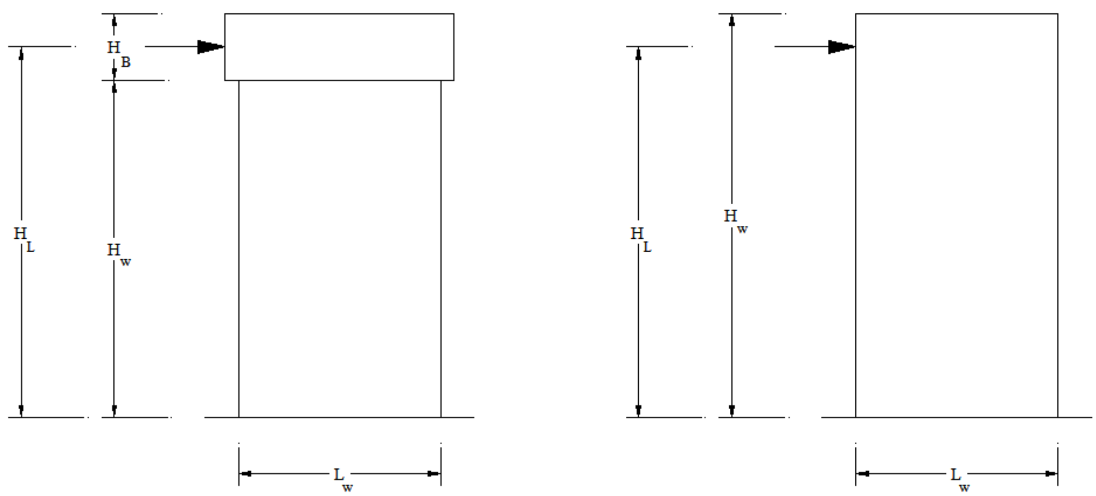

a) Masonry Wall with Concrete Beam b) Masonry Wall without Concrete Beam

Figure 3.6 Typical Cantilever Masonry Walls

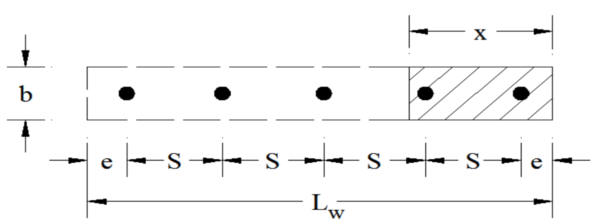

Figure 3.7 Masonry Wall Cracked Section

In the case of applied moment only, without axial load, the position of the neutral axis can be obtained by taking the moment of areas about the neutral axis.

$$\frac{bx^2}{2} + nA_{sb}\sum_{i=1}^{N}(e+(i-1)S) = (bx + nNA_{sb})x \qquad [3]$$

where

$$n = \frac{E_s}{E_m} \qquad [4]$$

The equation can be simplified as

$$\frac{b}{2}x^2 + nNA_{sb}x - nA_{sb}I = 0 \qquad [5]$$

where

$$I = (e-s)N + 0.5S(N+N^2) \qquad [6]$$

From the solution of the quadratic equation,

$$x = \frac{-nNA_{sb} + \sqrt{(nNA_{sb})^2 + 2bnA_{sb}I}}{b} \qquad [7]$$

However, in a general loading condition, the wall is subjected also to axial load. For the simple case of a beam subjected to both bending moment and axial load at the working stage, as shown in Figure 3.8, the position of the neutral axis can be obtained from internal force equilibrium.

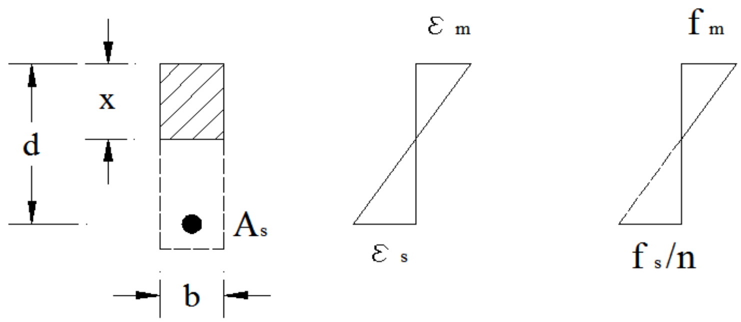

Figure 3.8 Beam Cracked Section

$$0.5f_m'bx - A_s f_s = P \qquad [8]$$

By replacing stresses with strains,

$$0.5E_m\varepsilon_m bx - A_s E_s \varepsilon_s = P \qquad [9]$$

From the plane section assumption,

$$\frac{\varepsilon_s}{\varepsilon_m} = \frac{d-x}{x} \quad [10]$$

By substituting into the internal force equation,

$$\varepsilon_m (0.5bx - nA_s \frac{d-x}{x}) = \frac{P}{E_m} \quad [11]$$

The final formula can be represented as

$$\frac{bx^2}{2} - nA_s(d-x) = \frac{P}{f_m} x \quad [12]$$

The previous equation is analogous to equation 5, which can be modified as

$$\frac{b}{2} x^2 + nNA_{sb} x - nA_{sb} I = \frac{P}{f_m} x \quad [13]$$

The position of the neutral axis is

$$x = \frac{-(nNA_{sb} + \frac{P}{f_m}) + \sqrt{(nNA_{sb} + \frac{P}{f_m})^2 + 2bnA_{sb} I}}{b} \quad [14]$$

In the previous equation, the maximum compressive stress f_m in masonry is required to find the position of the neutral axis. This stress value can be defined as

$$f_m = \frac{M_a}{I_{cr}} x + \frac{P}{A_{cr}} \quad [15]$$

The cracked moment of inertia is

$$I_{cr} = \frac{bx^3}{3} + nA_{sb} J \quad [16]$$

where

$$J = \sum_{i=1}^{N} (e + (i-1)S - x)^2 = (e - s - x)^2 N + (e - s - x)(N + N^2)S + (\frac{N}{6} + \frac{N^2}{2} + \frac{N^3}{3})S \quad [17]$$

and the cracked area is

$$A_{cr} = bx + nNA_{sb} \quad [18]$$

Also, the applied moment M_a is required. In the case of collapse analysis, yielding moment M_y should be used instead of applied moment, which can be calculated as

$$M_y = \frac{(\frac{f_y}{n} + \frac{P}{A_{cr}})I_{cr}}{(e + (N-1)S - x)} \qquad [19]$$

The previous set of equations requires an iterative process because the position of the neutral axis governs the moment of inertia, area, masonry compressive stress, and yielding moment calculations.

As masonry behaves like concrete, the stiffness of the wall passes through two stages: first, the wall behaves as an uncracked section until it reaches the cracking moment, at which point it behaves as a cracked section, as shown in Figure 3.9

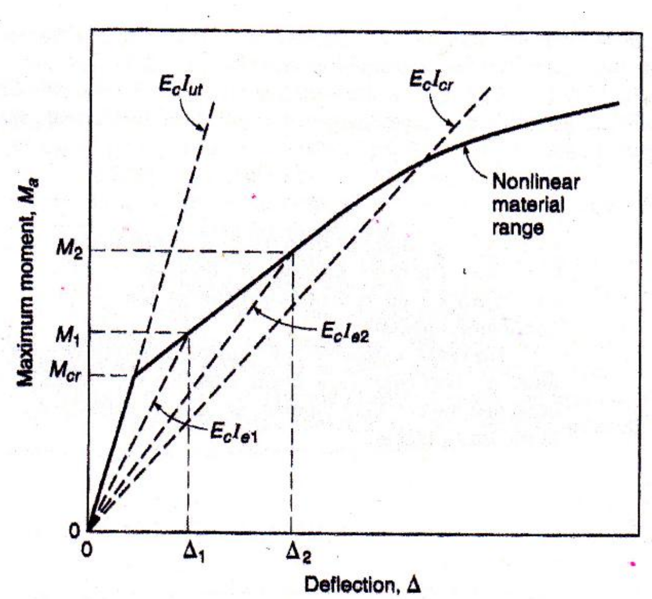

Figure 3.9 Deflection of Reinforced Concrete Beams (Nilson et al., 2003)

In order to represent this change in moment of inertia, an effective moment of inertia can be used. The ACI equation for effective moment of inertia in concrete sections is also applicable for masonry structures (Horton and Tadros, 1990).

$$I_{eff} = I_g (\frac{M_{cr}}{M_a})^3 + I_{cr}(1 + (\frac{M_{cr}}{M_a})^3) \leq I_g \qquad [20]$$

The gross moment of inertia can be calculated as

$$I_g = \frac{b(2e + (N-1)S)^3}{12} + nA_{sb}S^2K \qquad [21]$$

where

$$K = \sum (i - (\frac{N+1}{2}))^2 = \frac{N^3 - N}{12} \quad [22]$$

The cracking moment is

$$M_{cr} = \frac{2(f_t + \frac{P}{A_g})I_g}{(2e + (N-1)S)} \quad [23]$$

where the gross area of the section would be

$$A_g = b(2e + (N-1)S) + nNA_{sb} \quad [24]$$

The final step is to find an equivalent modulus of elasticity to combine with the finite element gross moment of inertia I_g', leading to the same flexural stiffness:

$$E_m I_{eff} = E_{eq} I_g' \quad [25]$$

where

$$I_g' = \frac{b(2e + (N-1)S)^3}{12} + \frac{E_s}{E_{eq}} A_{sb} S^2 K \quad [26]$$

By substituting from Equation 26 into Equation 25,

$$E_{eq} = \frac{E_m I_{eff} - E_s A_{sb} S^2 K}{b(2e + (N-1)S)^3 / 12} \quad [27]$$

Finally, the scaling factor due to material behavior can be calculated as

$$\alpha_m = \frac{E_{eq}}{E_m} = \frac{I_{eff} - nA_{sb} S^2 K}{b(2e + (N-1)S)^3 / 12} \quad [28]$$

3.4 Finite Element Model Description

In this study, the finite element program ADINA is used for modeling. In this section, the details of the finite element model are described.

3.4.1 Elements

There are two types of elements used in the model, as shown in Figure 3.10:

- Nine node 2-D solid plane stress element: to model the masonry wall and the concrete beam.

- 1-D axial truss element: to model the discretized steel reinforcement.

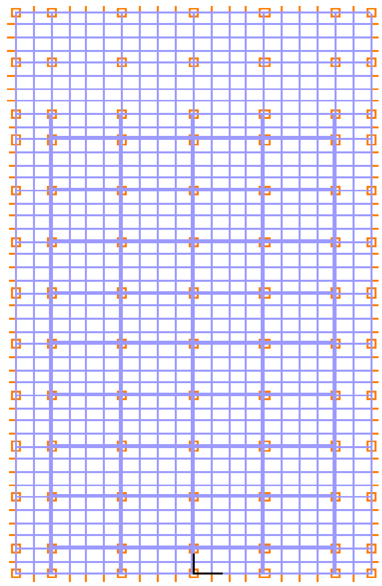

a) Masonry Walls with Concrete Beam

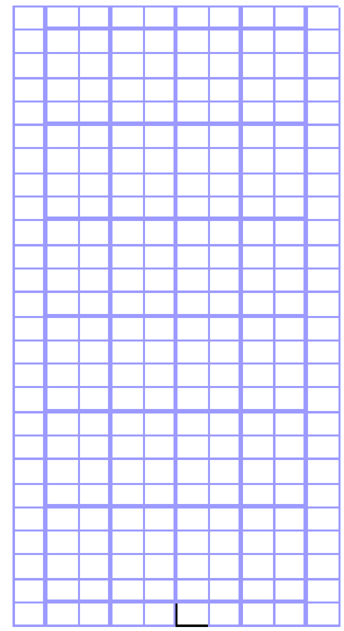

b) Masonry Walls without Concrete Beam

Figure 3.10 Masonry Wall FE Model.

3.4.2 Materials

Three types of material models were used:

- Concrete material: to model the masonry wall. The concrete model in ADINA allows the use of fracture energy to achieve mesh size independence.
- Elasto-plastic material: to model the reinforcement steel.
- Linear elastic material: to model the concrete loading beam, or the upper part of the masonry wall above the applied load. The main purpose of these elements is to prevent numerical local failure at the loading point.

3.4.3 Meshing

Different mesh sizes were considered for the models. To be consistent, mesh sizes of 1/4, 1/2, and 1 times the maximum reinforcement spacing were used, as shown in Figure 3.11.

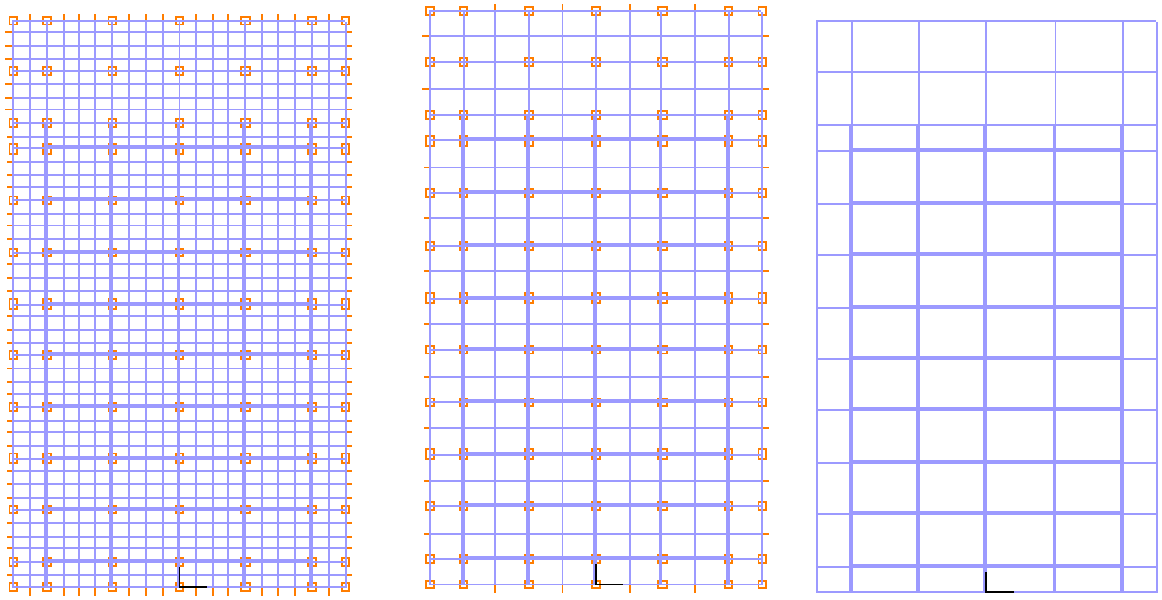

a) 1/4 Spacing Mesh Size a) 1/2 Spacing Mesh Size a) Spacing Mesh Size

Figure 3.11 Meshing of the FE Model.

3.4.4 Loading

Besides a constant vertical load, a displacement type of loading was applied to the top of the wall, as shown in Figure 3.12, with a step increment of 0.001 inch.

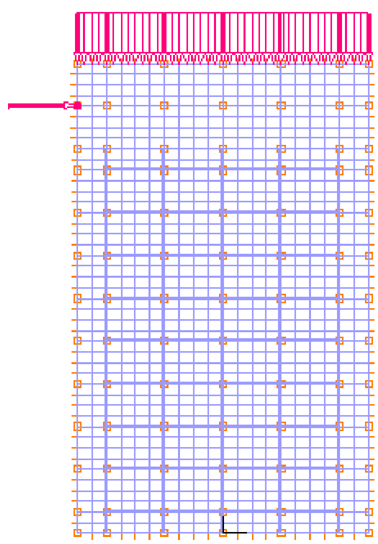

Figure 3.12 Loading of the FE Model.

3.4.5 Boundary Conditions

Vertical and horizontal displacements were constrained at the wall base to represent a full fixity condition. Although wall sliding is a possible failure mode, which requires a different type of boundary condition, this aspect of behavior was beyond the scope of this analysis, as it requires further experimental study.

3.4.6 Model Kinematics

Nonlinear analysis with a large displacement formulation was considered, and the lateral loading was applied through prescribed displacement for the purpose of expediting convergence.

3.4.7 Fictitious Dynamics

During an analysis, when the first element experiences cracking, its stiffness matrix is no longer positive definite, which often leads to nonconvergence in the solution. In order to continue with the analysis, the low speed dynamics (LSD) feature in ADINA was used. In that case, a fictitious damping matrix is added to the model, as defined in Equation 29.

$$[C] = \alpha_c [M] + \beta_c [K] \qquad [29]$$

Because the analysis is still static and no mass was applied to the model, the fictitious damping matrix only affects the stiffness matrix. The value of the coefficient β_c is *recommended* to be defined as in Equation 30, and its default value is 0.0001 (ADINA, 2010). As long as the fictitious dynamic force is less than 1% of the applied force, the static analysis is deemed to be unaffected by the addition of the artificial damping.

$$\beta_c \leq 10^{-5} \text{ of Time Step Size} \qquad [30]$$

For consistency in the results, the default value of 0.0001 was used for all specimen models with their different mesh sizes.

3.5 Modeled Specimens

Eight Specimens were modeled to investigate the validity of the proposed approach. The first two specimens were a part of an experimental program that is concurrently taking place (Sherman, 2011). The other six specimens were part of a previous experimental program (Eikanas, 2003). All specimens are described in Table 3.1, with reference to Figure 3.6.

Table 3.1 Modeled Specimens

Wall Specimen	H_w $(in.)$	H_L $(in.)$	L_w $(in.)$	H_L / L_w	Vert. Reinf.	Horiz. Reinf.	ρ_{VL}	$f_m'^{**}$ (Psi)	Axial Load*** (Kips)
1*	72	80	40	2.00	5#6@8"	9#4@8"	0.0072	2775	48
2*	72	80	40	2.00	5#4@8"	9#4@8"	0.0032	2775	95
3	72	52	55.625	0.93	4#5@16"	5#4@16"	0.0031	1630	11.4
4	104	84	55.625	1.50	4#5@16"	7#4@16"	0.0031	1630	11.4
5	72	52	55.625	0.93	7#5@8"	5#4@16"	0.0055	1630	11.4
6	104	84	55.625	1.50	7#5@8"	7#4@16"	0.0055	1630	11.4
7	104	84	39.625	2.10	5#5@8"	7#4@16"	0.0057	1630	8.13
8	72	52	71.625	0.72	5#5@16"	5#4@16"	0.0030	1630	14.7

***** Walls with concrete loading beam of 12 in width, 16 in height, and 44 in length.

** Average Prism Strength.

***Does not include self-weight of the wall.

All walls have thickness of 7.6 in

Grade 60 steel was used for reinforcement in all specimens, resulting in yield and ultimate stress values in the finite element analyses of 60 and 75 Ksi, respectively.

Peak loads and their associated displacements (PLD) from experimental data are presented in Table 3.2

Table 3.2 Experimental Peak Loads and Displacements

Specimen	1	2	3	4	5	6	7	8
Ultimate Load (Kips)	41.37	37.21	48.74	30.59	63.33	42.35	27.06	71.25
PLD (in)	1.1	0.55	0.7	0.59	0.57	0.95	0.58	0.27

For these specimens, nominal peak load was calculated using LRFD and presented in Table 3.3. By comparing the calculated and experimental peak loads, it was observed that the calculated peak load varies from the experimental data by 0.3-24.7%. This can be explained in terms of the variation of material properties.

Table 3.3 Peak Loads

Specimen		1	2	3	4	5	6	7	8
Peak Load (Kips)	Experimental	41.37	37.21	48.74	30.59	63.33	42.35	27.06	71.25
	Calculated (var. %)	37.04 (10.5)	31.65 (15.9)	42.61 (12.6)	29.5 (3.6)	63.53 (0.3)	39.33 (7.1)	20.38 (24.7)	68.78 (3.5)

All experimental specimens were cyclically loaded until failure. However, the FE analyses were monotonic. In order to compare numerical and experimental results, the load-displacement curves obtained from the FE model for each specimen were compared with the envelope defined by experimental cycle peaks.

For each specimen, the suggested methodology was followed to consider the reduction in stiffness from initial cracking. The Scaling factor α_m for each specimen, based on yield moment as applied moment, is presented in Table 3.4.

Table 3.4 Specimen Masonry Scaling Factors

Specimen	1	2	3	4	5	6	7	8
α_m	0.204159	0.413914	0.157824	0.157824	0.169664	0.169556	0.168239	0.164426

The calculated scaling factors are similar to the moment of inertia reduction factors used to estimate the actual cracked deflection of concrete members, which vary from 0.35 to 0.7 for compression and flexural members in ACI 318-08 (2008). As expected, masonry values are lower than concrete values because of lower masonry tensile strength, due to the interaction between masonry units and mortar, and modulus of elasticity.

3.6 Results

Selected results for representative specimens are presented in the figures below. For each case, the following items are shown:

- Deflected shape and crack pattern;
- Masonry principal stresses;
- Axial strain in steel; and

- Comparison between FE and experimental results.

Note that the “comparison between FE and experimental results” figures include two identical curves, labeled as Numerical and Numerical (M), which are mirror images of each other. These two curves are used to compare the numerical results with the experimental hysteresis results, which includes load/displacement in two opposite directions. Finally, the full results of all specimens are listed in Appendix A.

3.6.1 Results for Specimen 1

Figures 3.13, 3.14, and 3.15 show the results for Specimen 1 and three levels of mesh refinement. This specimen is mainly governed by flexural response, as it is loaded at a height of 80 in, with a width of 40 in. Also, it has the highest reinforcement ratio among the specimens. Finally, it has the middle value of axial load applied. This specimen was chosen to check the flexural response of the model.

The crack pattern shows crack propagation at the base, due to bending. Also, cracks followed the vertical steel as it developed large deformation due to yielding. Most of the cracks are horizontal, due to strain from bending. However, there are some cracks that are inclined due to the development of a local truss mechanism with the interaction between shear and moment. With coarse meshes, the crack pattern is relatively smeared compared with the localized cracking of the finest mesh.

Another way to evaluate the behavior of the model is to examine the principal stress pattern. It is obvious that the compression stresses are very high and localized at the far end of the wall, as expected for the bending behavior. The compressive maximum stresses are nearly vertical, and the tensile maximum stresses follow the cracking pattern. Also, tensile stresses are reduced and redistributed as cracks initiate and propagate. From the crack pattern in the coarsest mesh, it appears that the final failure results when vertical cracks initiate on the compression side, which would indicate crushing there.

The figures representing steel strain indicate the locations and extent of yielding, where yielding occurs at a strain value of approximately 0.002, shown as red in tension and blue in compression. All yielding occurs in the vertical reinforcing bars in tension along with the cracks and in compression along the compressive zone, as is expected for bending behavior. On the other hand, the horizontal steel bars did not yield until excessive deformation occurred because of the relatively small shear stresses in the tall specimen.

Finally, the load-deflection curves from the FE analysis match quite well with the experimental data points taken from hysteretic peaks. It is necessary to mention that the Low Speed Dynamics feature of ADINA is required to give the model the ability to continue after the numerical instability condition that occurs with the first crack. At that point, existing stress in the affected element is suddenly reduced and convergence is generally not attainable. Physically, the initiation of a crack causes the stresses to redistribute in the actual specimen and the loading continues. The small bit of artificial damping that is added to the finite element model enables this redistribution of stress to occur so that the solution may proceed. It is interesting to note that, even with the artificial damping, the models with the finest meshes experienced numerical failure prior to reaching a peak load. With the coarsest mesh, physical failure mechanisms, such as steel yielding and concrete crushing, appear to cause the instability of the model. As the fracture steel strain is very high, concrete crushing is the expected source of final failure.

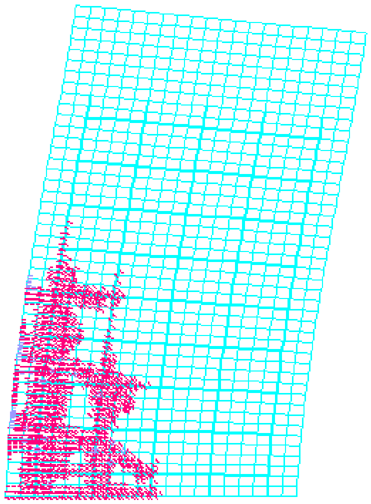

a) Deflected Shape and Crack Pattern

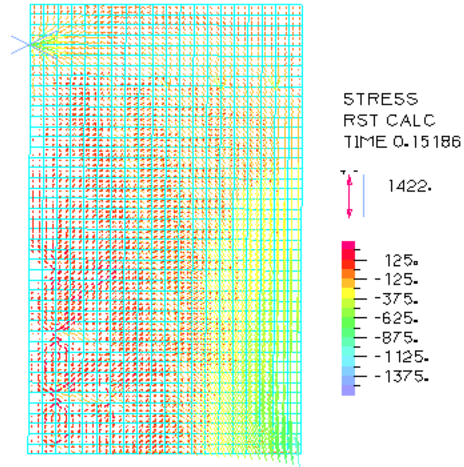

b) Masonry Principal Stresses

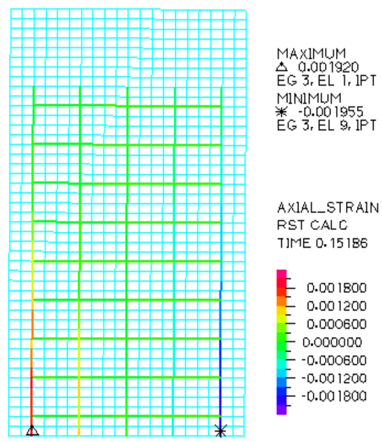

c) Axial Strain in Steel

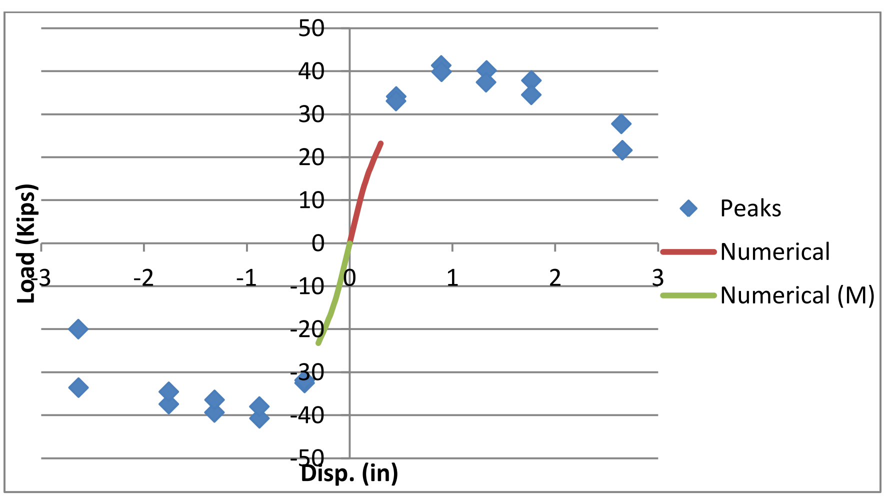

d) Comparison between FE and experimental results

Figure 3.13 Wall 1 (1/4 Spacing Mesh) Results

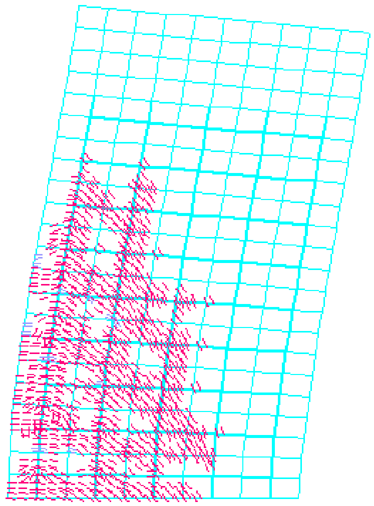

a) Deflected Shape and Crack Pattern

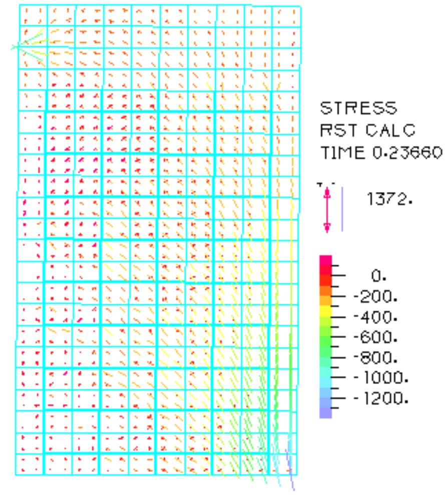

b) Masonry Principal Stresses

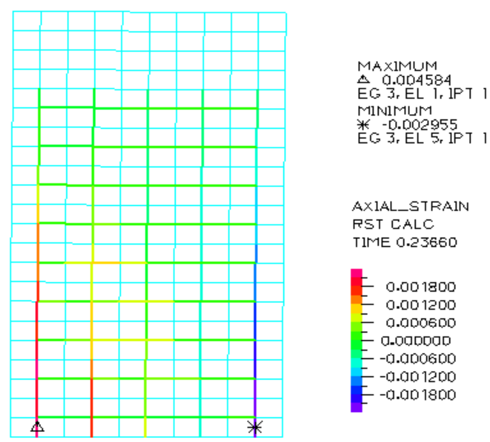

c) Axial Strain in Steel

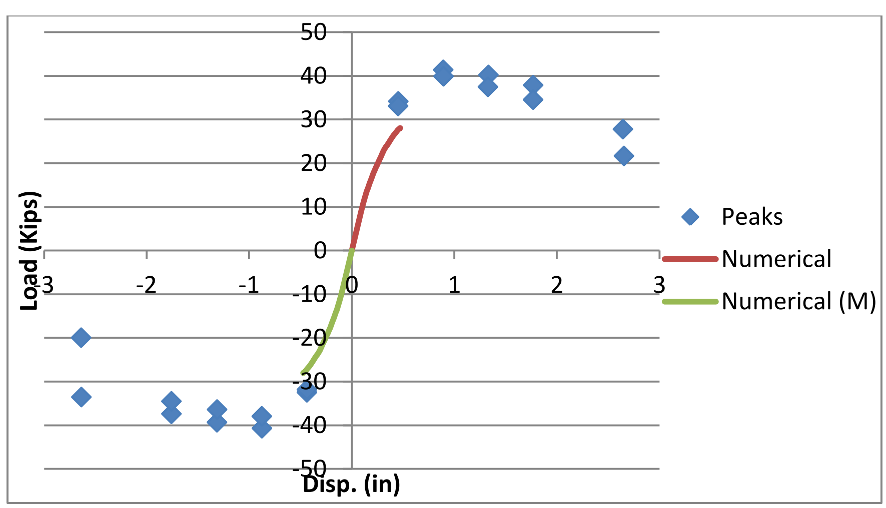

d) Comparison between FE and experimental results

Figure 3.14 Wall 1 (1/2 Spacing Mesh) Results

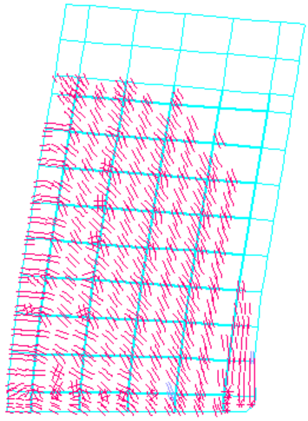

a) Deflected Shape and Crack Pattern

b) Masonry Principal Stresses

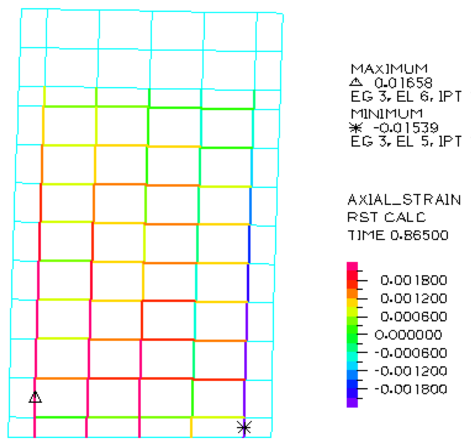

c) Axial Strain in Steel

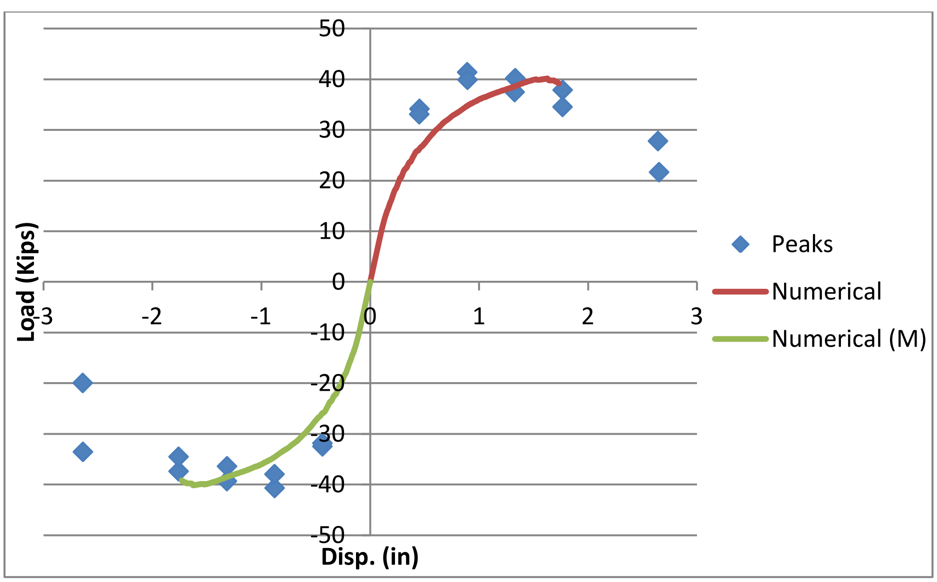

d) Comparison between FE and experimental results

Figure 3.15 Wall 1 (Spacing Mesh) Results

3.6.2 Results for Specimen 8

Figures 3.16, 3.17, and 3.18 show the results for Specimen 8 and three levels of mesh refinement. This specimen is mainly governed by shear response, as it has a loading height of 52 in and a width of 71.625 in. It is the shortest wall of all the specimens. None of the short walls that were modeled had high values of axial load. This specimen was chosen to check the ability of the model to adequately simulate the response of a wall whose behavior is dominated by shear.

The crack pattern shows the formation of a main diagonal crack, due to shear. These cracks represent the formation of the strut and tie mechanism, which is the primary source of global shear resistance. Due to the presence of bending, an additional crack pattern exists at the base. The formation of this crack pattern is related to the amount of axial load applied to the wall. With higher values of axial load, this crack pattern will be reduced. The diagonal crack pattern is responsible for the shear failure of the wall, and the base crack pattern is responsible for base sliding. As the mesh becomes coarser, the crack pattern becomes smeared compared to being more localized for the finest mesh.

Another way to evaluate the behavior of the model is to examine the principal stress pattern. It is obvious that the compression stresses are very high at the diagonal strut, as expected for the shear behavior. The compressive maximum stresses are diagonal, and the tensile maximum stresses are perpendicular to them and follow the cracking pattern. Because the coarser mesh models have the ability to carry more load, they have more ability to represent concrete diagonal strut crushing. Although that was not the case for the largest mesh in this specimen, it could be related to the effect of the low speed dynamics, not the meshing size.

The figures representing steel strain indicate the locations and extent of yielding, where yielding occurs at a strain value of approximately 0.002, shown as red in tension and blue in compression. Vertical and horizontal steel provides yielding, or strain values close to yield, along with the diagonal tie and the base crack patterns, as was expected for shear behavior.

Finally, the load-deflection curves from the FE analysis match quite well with the experimental data points taken from hysteretic peaks, as far as they go. The Low Speed Dynamics feature of ADINA is again required to give the model the ability to continue after the numerical instability condition that occurs with the first crack. However, even with the artificial damping, all three models experienced numerical failure prior to reaching a peak load.

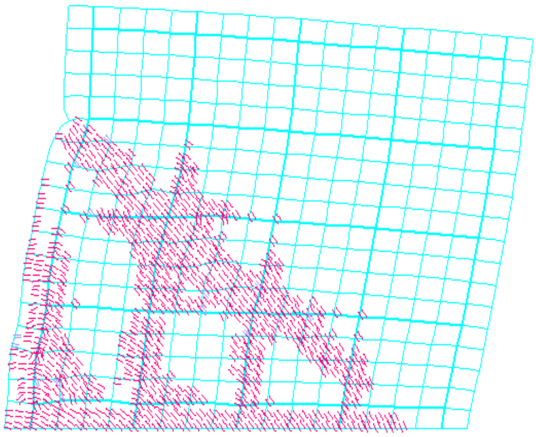

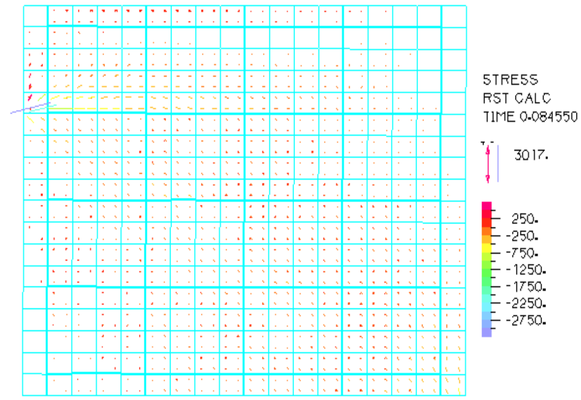

a) Deflected Shape and Crack Pattern b) Masonry Principal Stresses

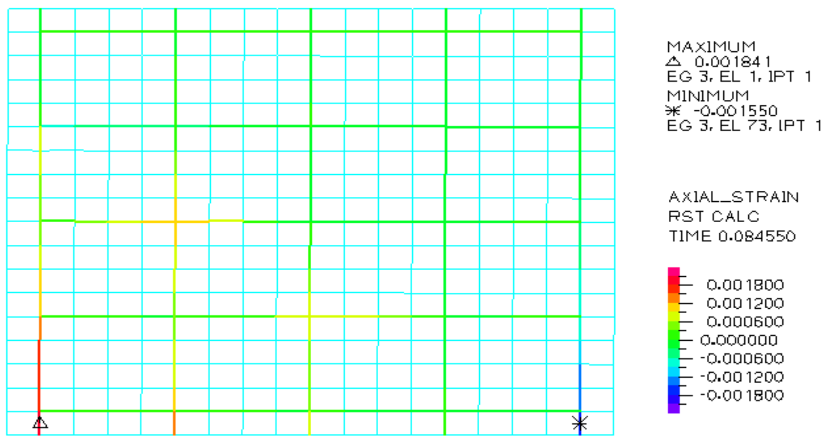

c) Axial Strains in Steel

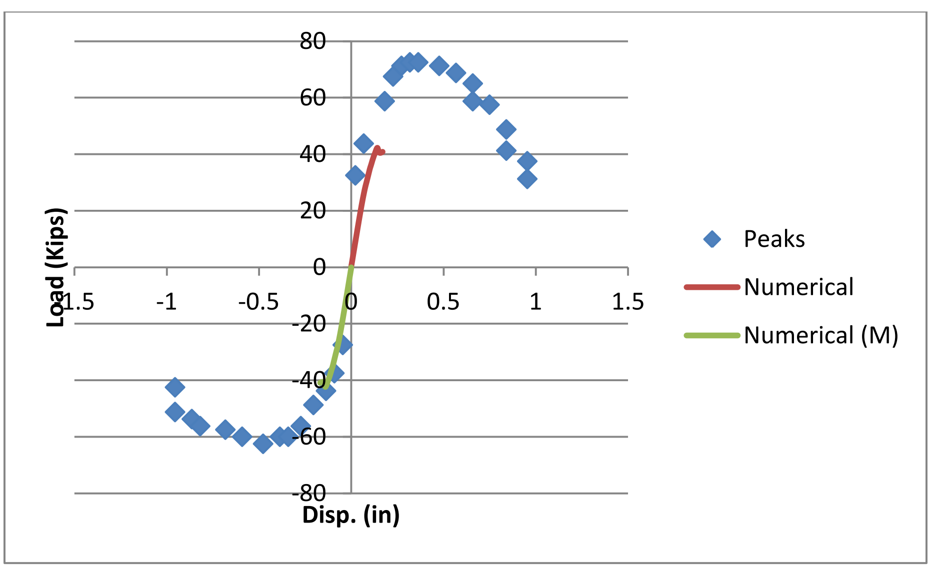

d) Comparison between FE and experimental results

Figure 3.16 Wall 8 (1/4 Spacing Mesh) Results

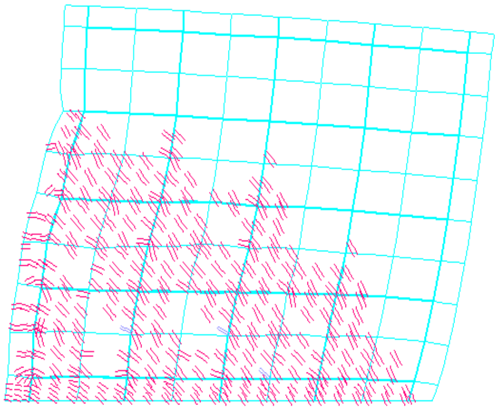

a) Deflected Shape and Crack Pattern

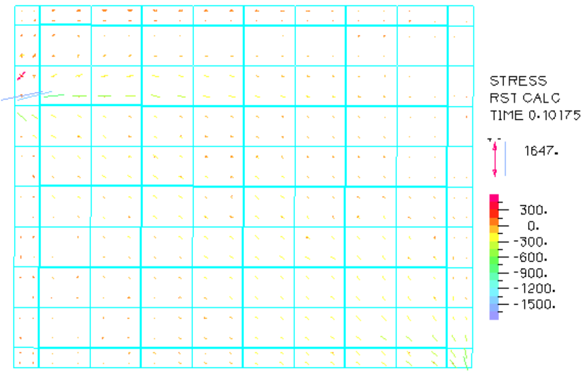

b) Masonry Principal Stresses

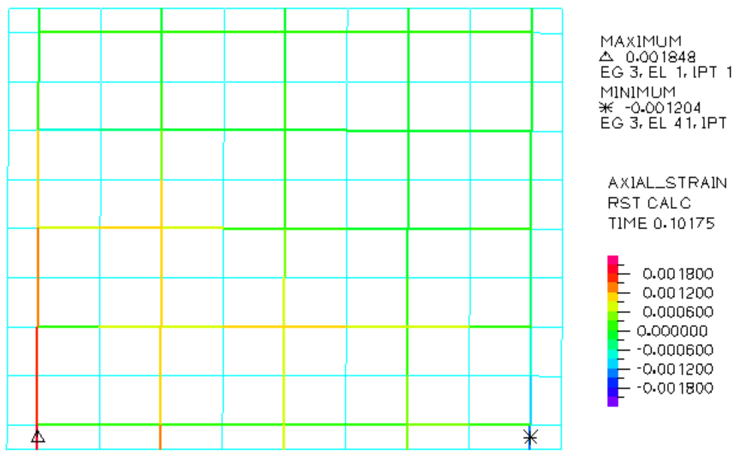

c) Axial Strains in Steel

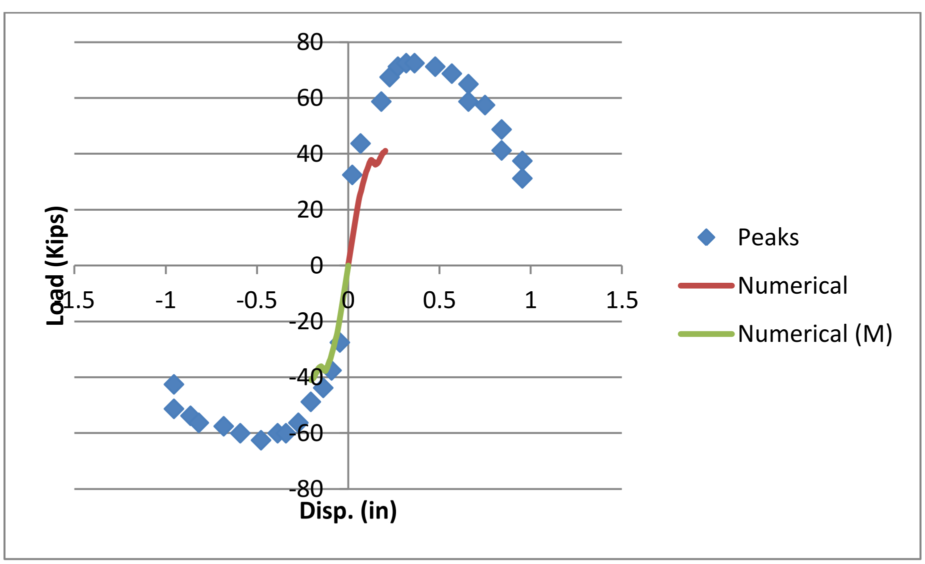

d) Comparison between FE and experimental results

Figure 3.17 Wall 8 (1/2 Spacing Mesh) Results

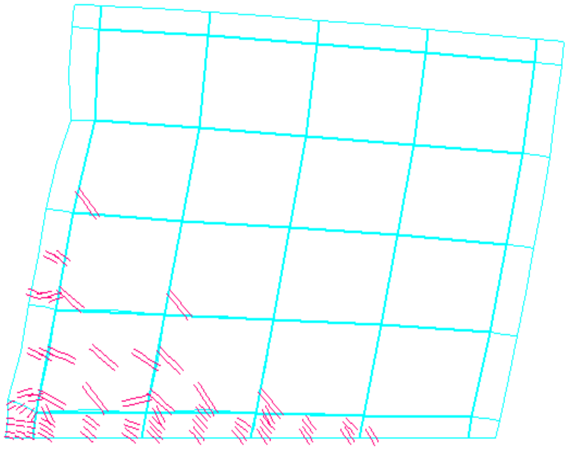

a) Deflected Shape and Crack Pattern

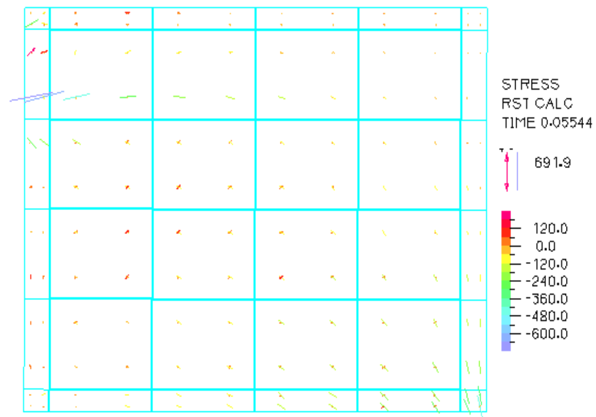

b) Masonry Principal Stresses

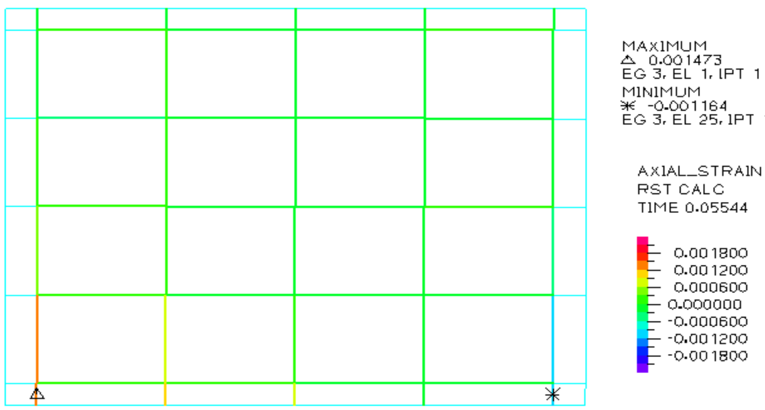

c) Axial Strains in Steel

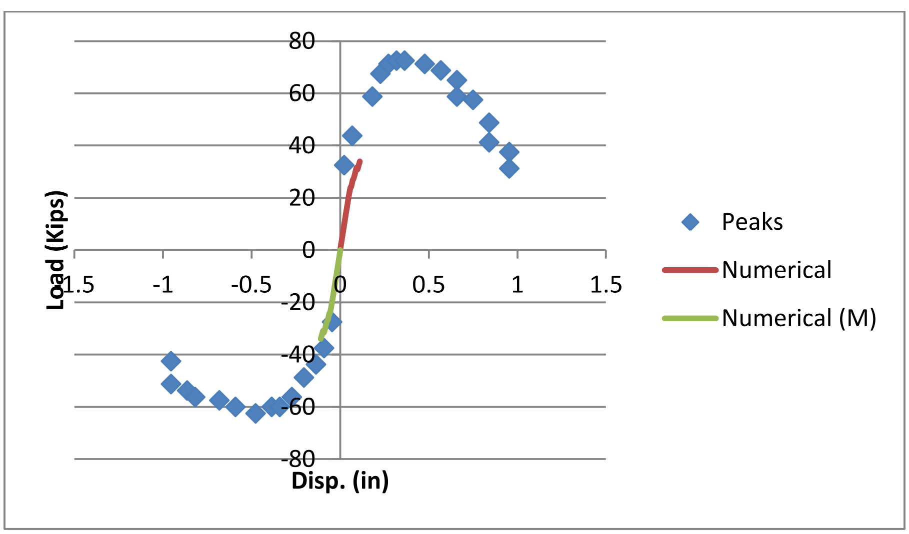

d) Comparison between FE and experimental results

Figure 3.18 Wall 8 (Spacing Mesh) Results

3.7 Discussion

The results of the two specimens that were presented show a strong agreement between the stiffness of the FE model, based on the described material assumptions and applied scaling technique for coarse meshing, and that of the experimental test specimens. Also, the FE models showed the potential to develop different failure mechanisms, such as flexural failure for relatively long walls and the strut and tie failure mechanism for relatively short walls.

For all of the specimens that were modeled, mesh size independence was achieved due to the fracture energy criteria used to define material behavior. In some of the models, elements with an aspect ratio of 2 were used without appearing to affect the overall behavior.

In general, coarse meshes showed a greater ability to carry loads/displacement further than fine meshes, mainly because the level of load required to reach the failure criteria at the integration points of individual elements is higher. This is caused by the significant smearing of the crack pattern. In a few cases, larger meshes stopped earlier, but slightly increasing the low speed dynamics factor allowed the model to progress further.

In order to control the fictitious damping effect on the model and to predict the wall displacement at peak load, the calculated failure load from Table 3.3 can be used. If the model was unable to develop a peak value of load (ND), increasing the fictitious damping coefficient will allow the solution to progress further. However, increased damping may result in unrealistic behavior. In Table 3.5, the displacement values from the finite element models at calculated peak load are given and compared to those from the experimental tests. The displacement associated with these loads varied from the experimental data by 1.8-37%.

Table 3.5 Peak Load Displacements

Specimens	Experimental PLD (in)	Predicted PLD (in) (Var. %)		
		¼ spacing mesh	½ spacing mesh	Spacing mesh
1	1.1	ND	ND	1.12 (1.8)
2	0.55	ND	ND	0.59 (7.3)
3	0.7	ND	ND	0.49 (30)
4	0.59	ND	ND	ND
5	0.57	ND	ND	ND
6	0.95	ND	ND	1.0 (5.3)
7	0.89	ND	1.21 (36)	1.22 (37)
8	0.27	ND	ND	ND

In most cases, the model could trace the load-displacement behavior and predict the ultimate load. In some cases, the ultimate load was overestimated due to the effect of the fictitious dynamics. In that case, the artificial damping force has become significant, and decreasing the fictitious damping coefficient is recommended. On the other hand, the model was not able to trace the descending part of the load-displacement behavior in most cases, which is due to the use of fictitious damping.

Finally, shear dominated walls show a higher tendency to be affected with numerical instability for lower values of fictitious damping than flexure dominated walls. This is likely because their behavior is more highly influenced by brittle cracking of the masonry, leading to global model instability, than by yielding of the steel reinforcement.

CHAPTER FOUR

SMEARED STEEL MODEL

4.1 Introduction

In this chapter, the modeling of masonry walls is discussed, considering a macro approach with coarse meshing for the masonry material in conjunction with orthotropic plane stress elements to represent steel reinforcement in a smeared way. This model does not require the high level of detail used in the models of Chapter 3.

The previous approach for modeling the masonry will be used, as described in Chapter 3. The difference in this model is the use of a smeared steel element.

4.2 Smeared Steel Element

The technique proposed in this chapter can be simply described as applying orthotropic scaling to the steel constitutive relation by applying a factor, α_s, in each direction to represent smeared steel stiffness in an element. Because steel strain is assumed to be compatible with that of masonry, the scaling factor is applied to stress, as shown in Figure 4.1.

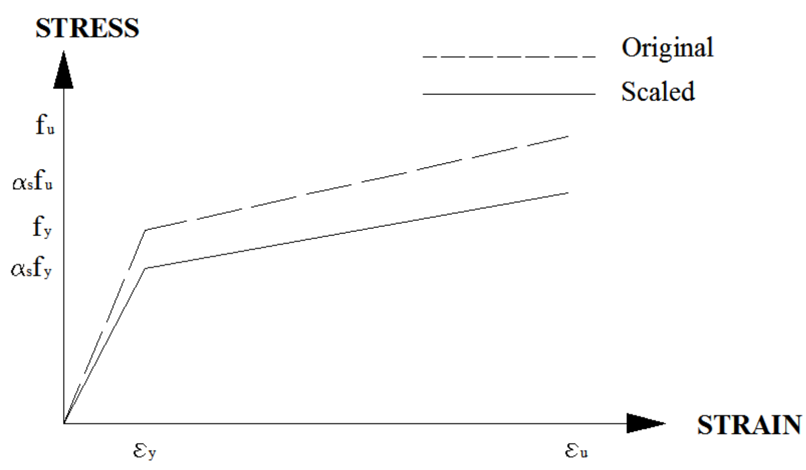

Figure 4.1 Stress-Strain of Smeared Steel

4.2.1 Smearing Formulations

In order to find the orthotropic properties of an equivalent smeared steel element, a simple plane stress element of masonry with dimensions L_x and L_y and the thickness of the wall, with two orthogonal steel reinforcement bars with areas A_{sx} and A_{sy}, is considered.

As the orthogonal steel is assumed to apply no contribution to shear resistance, the steel may be represented with end springs, as shown in Figure 4.2.

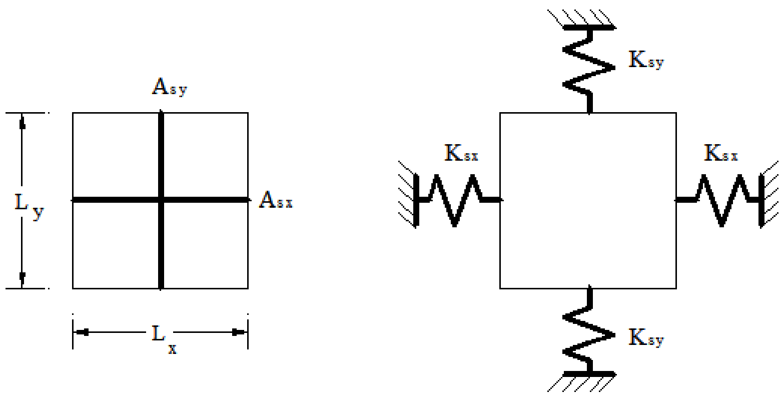

Figure 4.2 Equivalent Steel Springs

The stress-strain relation for axial components of masonry plane stress elements is represented as the following:

$$\begin{pmatrix} \sigma_x \\ \sigma_y \end{pmatrix} = \frac{E_m}{1-\nu^2} \begin{bmatrix} 1 & \nu \\ \nu & 1 \end{bmatrix} \begin{pmatrix} \varepsilon_X \\ \varepsilon_Y \end{pmatrix} \quad [31]$$

The stiffness values of the end springs are taken from those of standard axial elements.

$$K_{sx} = \frac{nE_m A_{sx}}{L_x} \quad [32]$$

$$K_{sy} = \frac{nE_m A_{sy}}{L_y} \quad [33]$$

where the forces in the x and y-direction springs, P_{sx} and P_{sy}, are

$$P_{sx} = nE_m A_{sx} \frac{\Delta_x}{L_x} \quad [34]$$

$$P_{sy} = nE_m A_{sy} \frac{\Delta_y}{L_y} \quad [35]$$

The equivalent stresses in the smeared steel element resulting from the steel reinforcement are then defined as

$$\sigma_{sx} = nE_m \rho'_x \, \varepsilon_X \quad [36]$$

$$\sigma_{sy} = nE_m \rho'_y \, \varepsilon_Y \quad [37]$$

where

$$\rho'_x = \frac{A_{sx}}{b' h_x'} \quad [38]$$

$$\rho'_y = \frac{A_{sy}}{b' h_y'} \quad [39]$$

and h'_x and h'_y are the in-plane dimensions and b' is the thickness of the reinforced masonry elements, as shown in Figure 4.3.

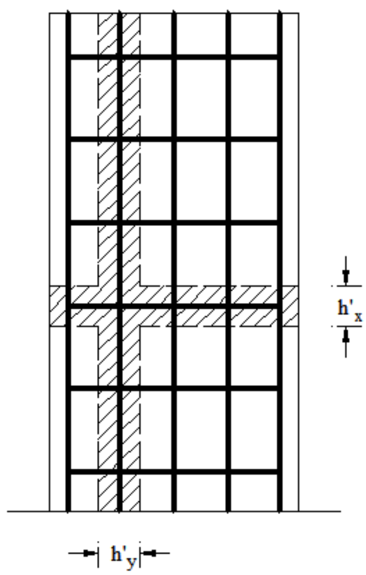

Figure 4.3 Reinforcement Steel Smearing on Structure Level

Then, the orthotropic constitutive relation of the smeared steel that contributes to the reinforced masonry element is

$$\begin{pmatrix} \sigma_{sx} \\ \sigma_{sy} \end{pmatrix} = E_s \begin{bmatrix} \rho_x' & 0 \\ 0 & \rho_y' \end{bmatrix} \begin{pmatrix} \varepsilon_X \\ \varepsilon_Y \end{pmatrix} \quad [40]$$

4.2.2 Stiffness Modification

The previous derivation was based on force equivalence, used to define wall stiffness. To be consistent, EI for the overall behavior of the wall should be the same for both smeared and discrete steel.

For the vertical reinforcement, the equivalent modulus of elasticity of the smeared orthotropic steel element in the vertical direction can be defined as:

$$E_{sy} = \rho_y' E_s = \frac{A_{sb}}{b' h_y'} E_s \qquad [41]$$

For the discrete vertical reinforcement bars, the contribution to wall bending stiffness is:

$$E_s I_s = E_s (A_{sb} S^2 K) \qquad [42]$$

For the smeared vertical reinforcement, the equivalent contribution to wall bending stiffness is:

$$E_{sy} I_s' = E_{sy} (N \frac{b' h_y'^3}{12} + b' h_y' S^2 K) \qquad [43]$$

The stiffness modification factor β can then be calculated as:

$$\beta = \frac{E_s I_s}{E_{sy} I_s'} = \frac{S^2 K}{N h_y'^2 / 12 + S^2 K} \qquad [44]$$

In some cases, steel is required to be smeared over the full area of the wall. In that case, the previous equation can be modified using the full amount of steel reinforcement in each direction over the complete wall dimensions, as follows:

$$E_{sy} = \rho_y' E_s = \frac{N A_{sb}}{b'(2e + (N-1)S)} E_s \qquad [45]$$

$$E_{sy} I_s' = E_{sy} (\frac{b'(2e + (N-1)S)^3}{12}) \qquad [46]$$

$$\beta = \frac{E_s I_s}{E_{sy} I_s'} = \frac{12 S^2 K}{N(2e + (N-1)S)^2} \qquad [47]$$

Finally, the orthotropic scaling factors are defined as:

$$\alpha_{sx} = \rho_x' \qquad [48]$$

$$\alpha_{sy} = \beta \rho_y' \qquad [49]$$

Note that horizontal reinforcement does not have a significant effect on shear wall bending stiffness. Therefore, the effect of the change of horizontal steel on the equivalent reinforced masonry wall element stiffness is ignored.

4.3 Finite Element Model Description

In this section, the details of the smeared finite element model are described. The main difference between the smeared model and the discretized model of Chapter 3 is the method of including the steel reinforcement in the finite elements. The assumptions for the masonry material are unchanged.

In this model, the stiffness of discrete steel reinforcing rods was added as an equivalent orthotropic plane stress finite element, overlaid with a masonry element. The nodes of both elements were set to be the same to enforce compatibility between them.

This methodology can be used with most commercially available FE programs as long as overlaying multiple elements is allowed. Alternatively, nodes of masonry elements and reinforcing elements can be tied together through constraints or rigid links.

4.4 Modeled Specimens

The wall specimens of Chapter 3 were again modeled using the reinforced masonry elements and the same meshing sizes. For each specimen, scaling factors, α_s, were calculated, based on the assumption that the thickness of the smeared element is the same as the thickness of the wall, as given in Table 4.1.

Table 4.1 Specimen Smeared Steel Scaling Factors

Specimens	1	2	3	4	5	6	7	8
$\alpha_{s\,x}$	0.003224	0.003224	0.001612	0.001612	0.001612	0.001612	0.001612	0.001612
$\alpha_{s\,y}$	0.006947368	0.003094737	0.003567592	0.003567592	0.004994629	0.004994629	0.004894737	0.003357158

4.5 Results and Discussion

Selected results for representative specimens are presented in the figures below. For each case, the following items are shown:

- Deflected shape and crack pattern;
- Masonry principal stresses;

- Steel plastic strain;
- Comparison between FE and experimental results; and
- Comparison between FE discretized and smeared models.

Note that the “comparison between FE and experimental results” figures include two identical curves, labeled as Numerical and Numerical (M), which are mirror images of each other. These two curves are used to compare the numerical results with the experimental hysteresis results, which includes load/displacement in two opposite directions. Finally, the full results of all specimens are listed in Appendix A.

4.5.1 Results for Specimen 1

Figures 4.4, 4.5, and 4.6 show the results for Specimen 1 and three levels of mesh refinement. The results of this smeared model are compared with the results of the alternative discretized model.

The crack pattern shows smeared crack propagation at the base and along the vertical steel direction as the steel developed large deformation due to yielding. Most of cracks are horizontal, due to bending, but there are some cracks that are inclined due to the effect of shearing, leading to a truss mechanism. For the finest mesh, localized flexure cracks appear, having large amounts of plastic strain. The numerical solution was seen to break down shortly after the localized masonry cracks appeared. The models with relatively coarse meshes did not exhibit crack localization, enabling the solution to proceed further. Then, the final breakdown of the solution occurred when the compression masonry reached failure.

The load-deflection curves from the smeared finite element models match quite well with both the experimental data points and the corresponding curves from the discretized models. It is necessary to mention that, as with the discretized models, the Low Speed Dynamics feature of ADINA was required to give the model the ability to continue after the instability condition that occurred with the first crack.

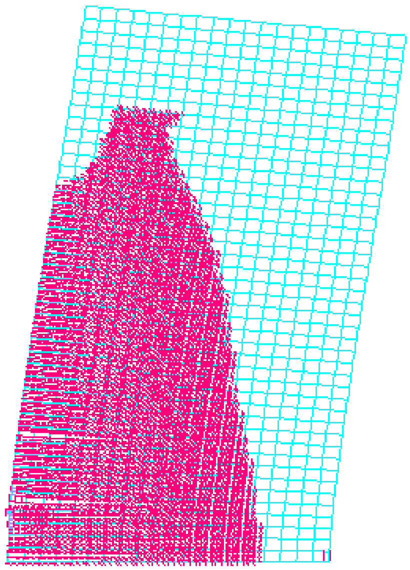

a) Deflected Shape and Crack Pattern

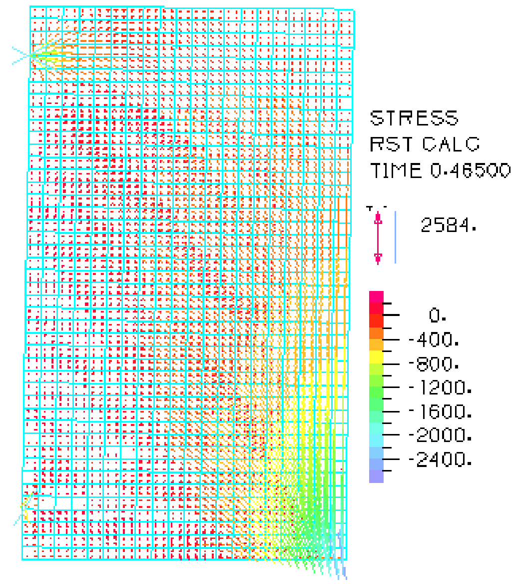

b) Masonry Principal Stresses

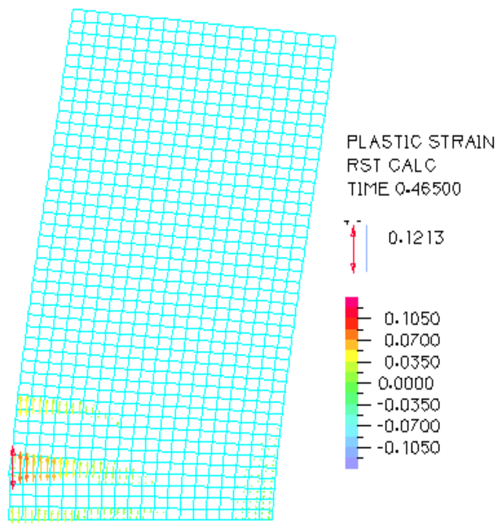

c) Steel Plastic Strain

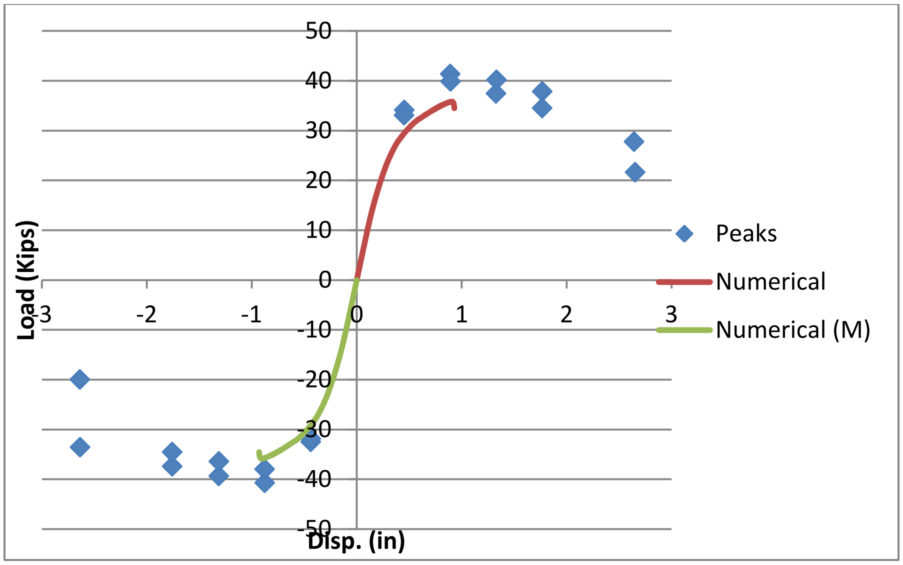

e) Comparison between FE and experimental results

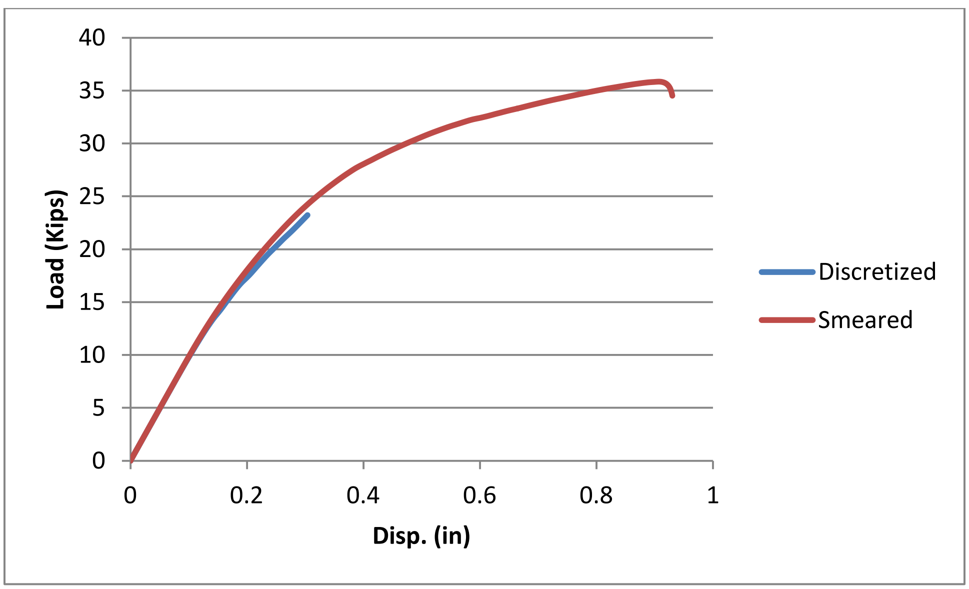

f) Comparison between FE Discretized and Smeared Models

Figure 4.4 Wall 1 (1/4 Spacing Mesh) Results

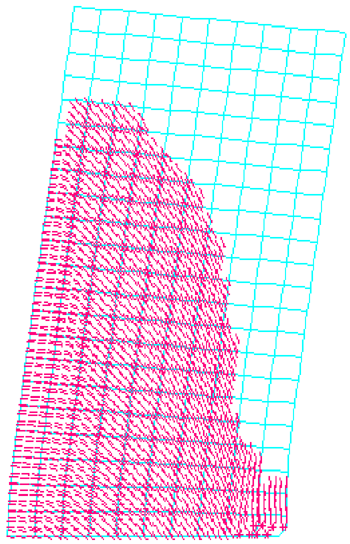

a) Deflected Shape and Crack Pattern

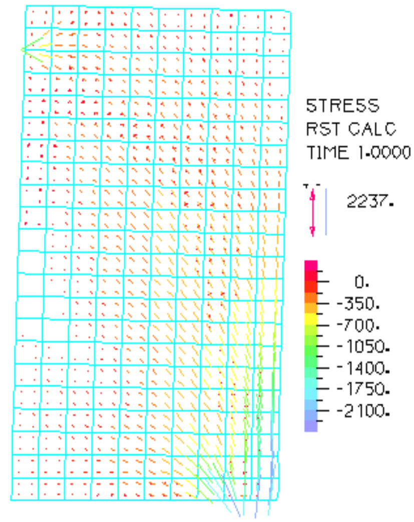

b) Masonry Principal Stresses

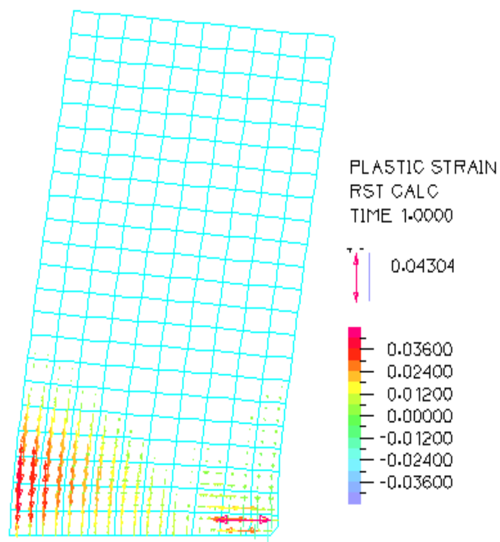

c) Steel Plastic Strain

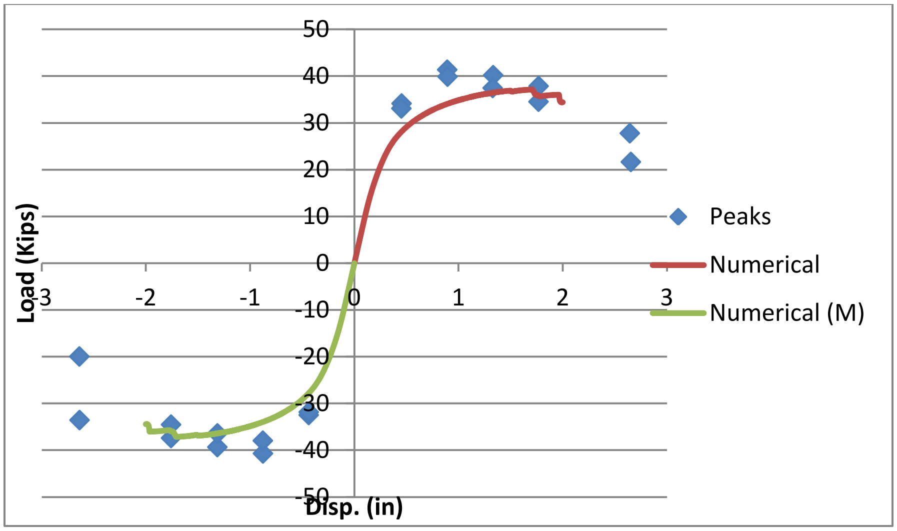

e) Comparison between FE and experimental results

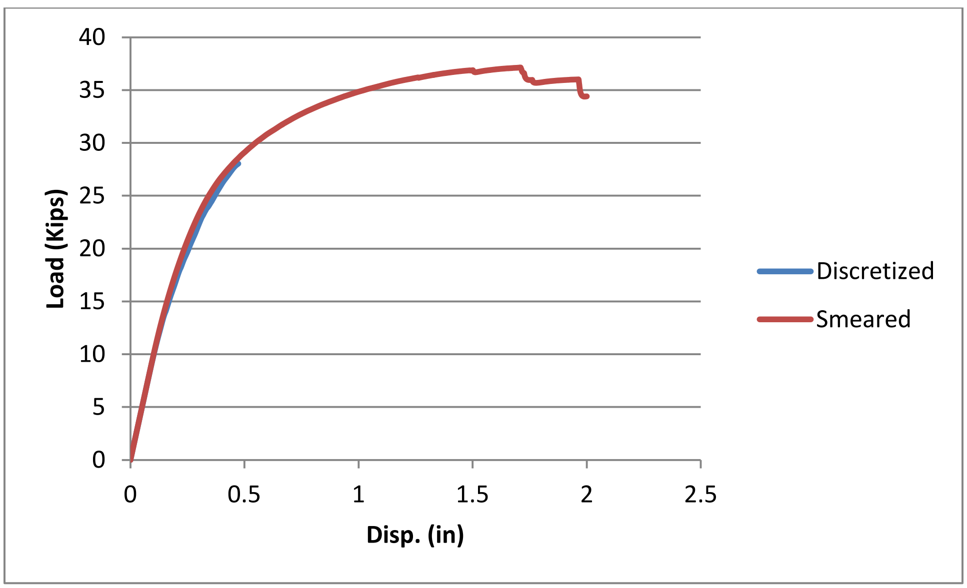

f) Comparison between FE Discretized and Smeared Models

Figure 4.5 Wall 1 (1/2 Spacing Mesh) Results

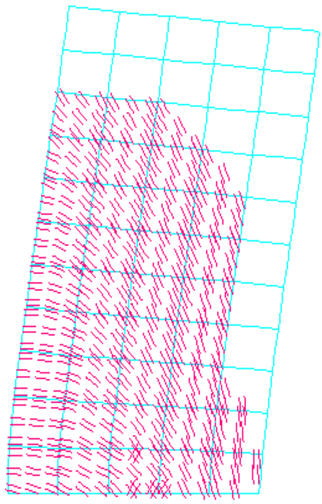

a) Deflected Shape and Crack Pattern

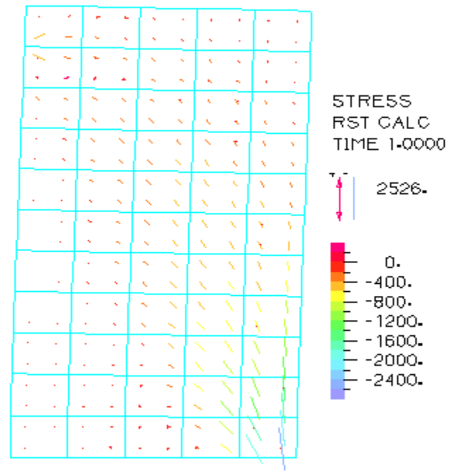

b) Masonry Principal Stresses

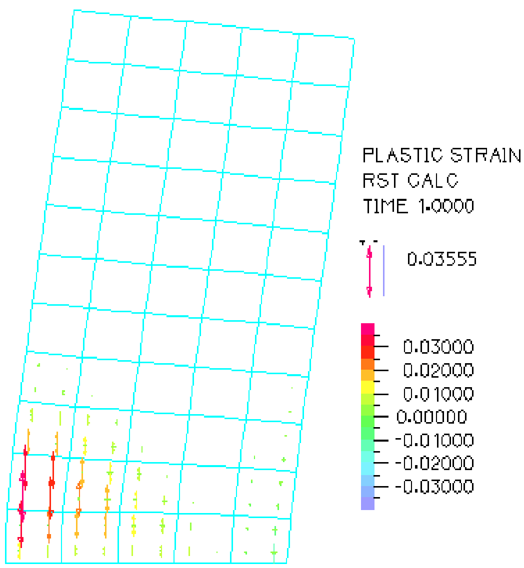

c) Steel Plastic Strain

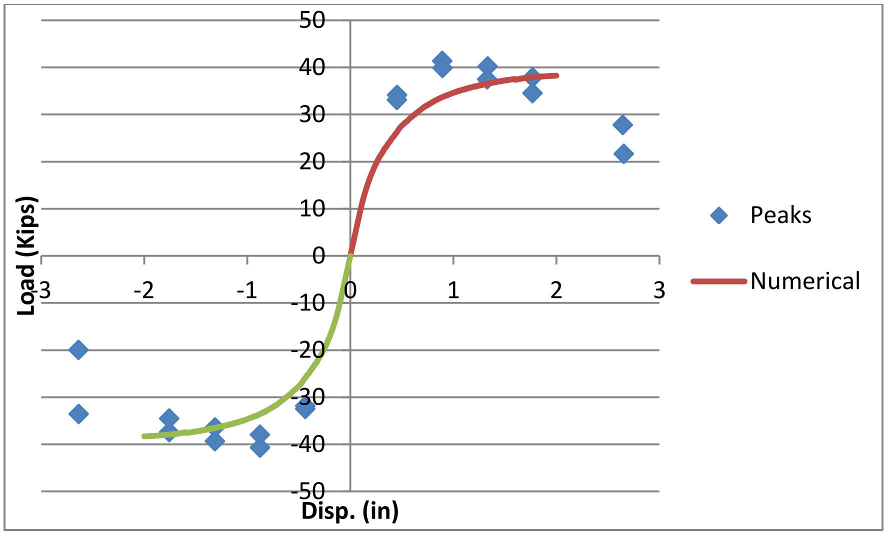

e) Comparison between FE and experimental results

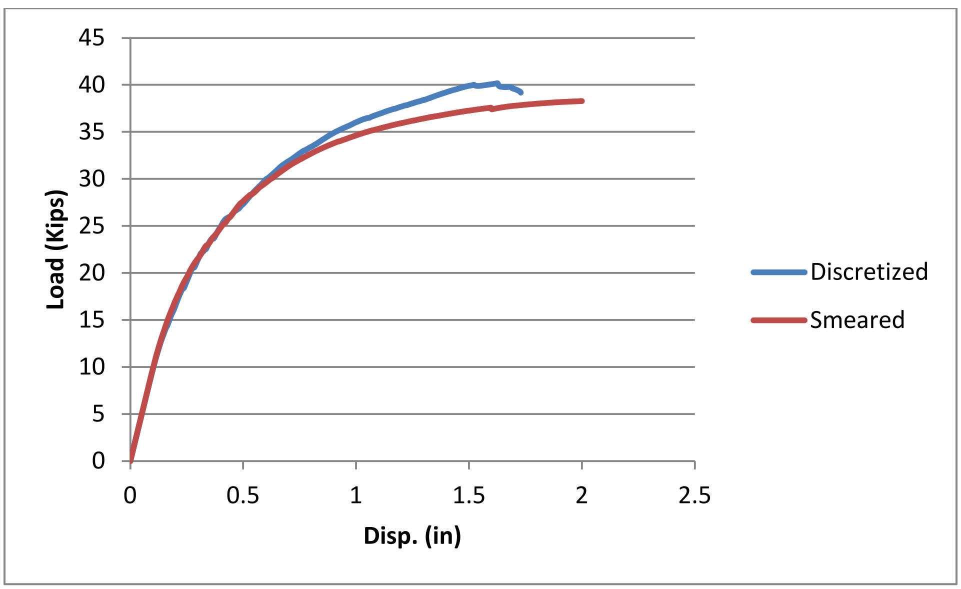

f) Comparison between FE Discretized and Smeared Models

Figure 4.6 Wall 1 (Spacing Mesh) Results

4.5.2 Results for Specimen 8

Figures 4.7, 4.8, and 4.9 and show the results for Specimen 8 and three levels of mesh refinement. The results of this smeared model are compared with the results of the alternative discretized model.

The crack pattern shows smeared diagonal cracks, which represents the formation of the strut and tie mechanism as with the discretized model. Also, due to the presence of bending, another smeared crack pattern exists at the base. The formation of this crack pattern is related to the amount of axial load applied to the wall. For higher values of axial load, this crack pattern will be reduced.

Again, a localized crack appeared in the model with the finest mesh, which led to a breakdown in the solution. With the coarser meshes, the plastic deformation was more highly distributed and the solution proceeded much further. In those cases, although the load-deflection curve is of a different shape compared to the experimental data points, it is interesting to note that the eventual instability in the solution occurred at approximately the same displacement as physical failure. In addition, the peak load value for the coarsest meshes, for which a peak was attained, is close to those obtained for the experimental specimen. However, it should be noted that the experimental data points represent peaks from cyclic loading, which may have accelerated damage in the masonry. Specimen 8 is the wall most heavily influenced by shear and it is, therefore, most influenced by damage in the masonry as compared with the taller walls which exhibit bending behavior and are more highly influenced by plasticity in the steel.

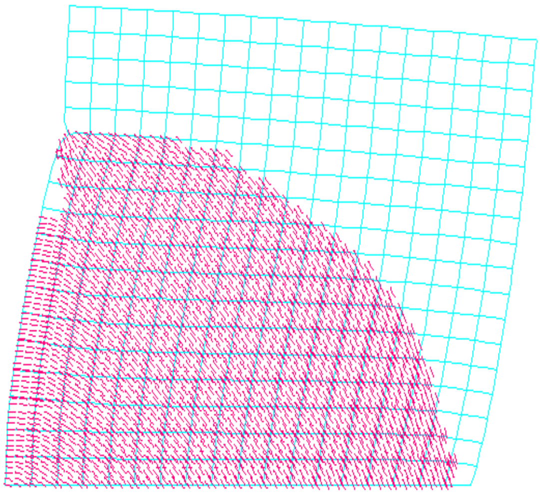

a) Deflected Shape and Crack Pattern

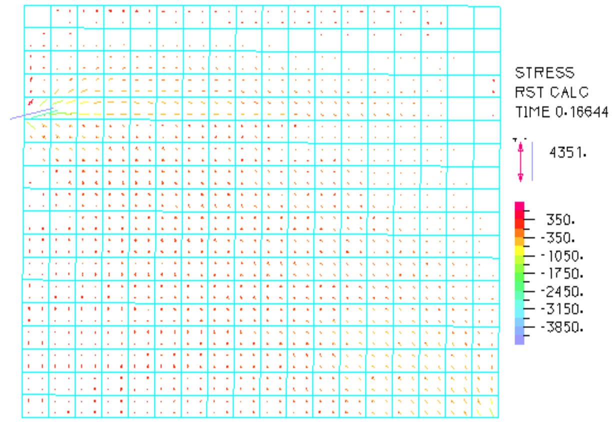

b) Masonry Principal Stresses

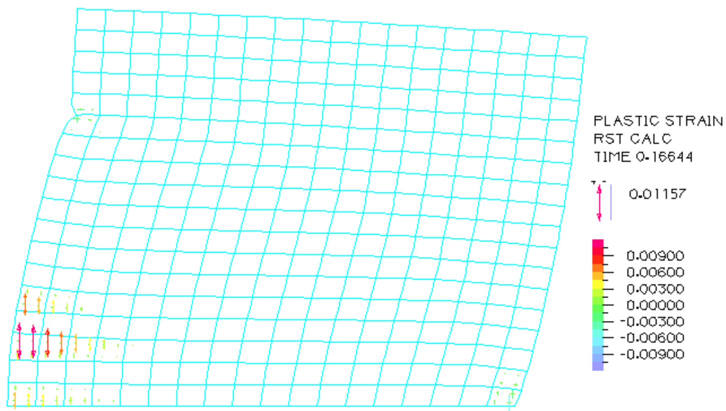

c) Steel Plastic Strain

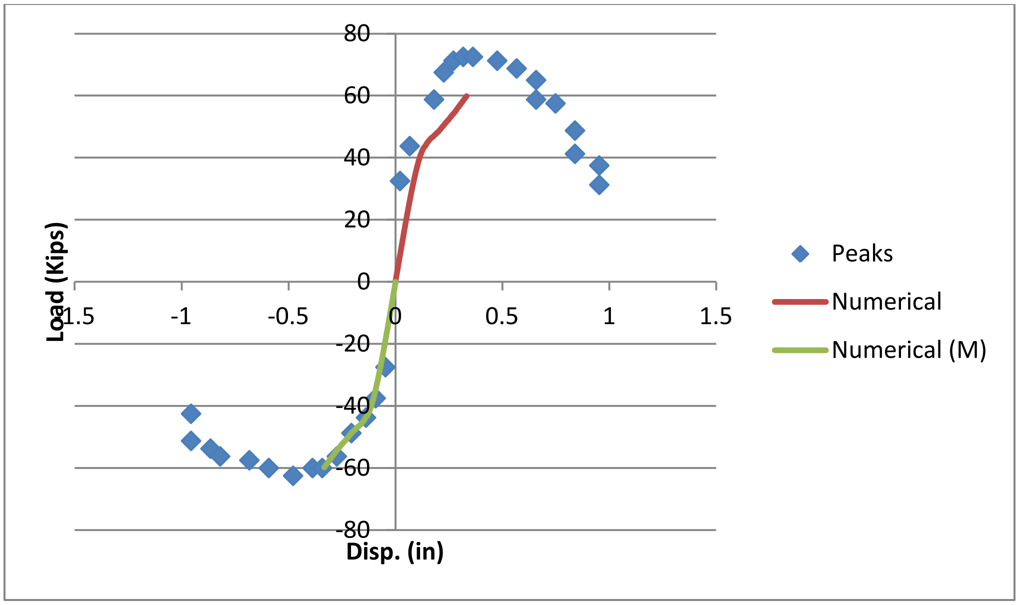

e) Comparison between FE and experimental results

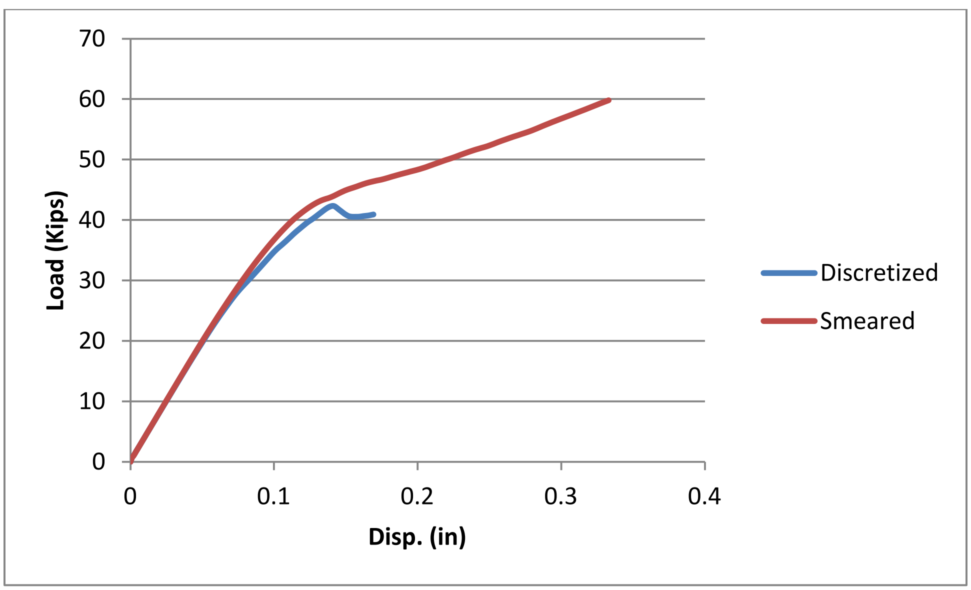

f) Comparison between FE Discretized and Smeared Models

Figure 4.7 Wall 8 (1/4 Spacing Mesh) Results

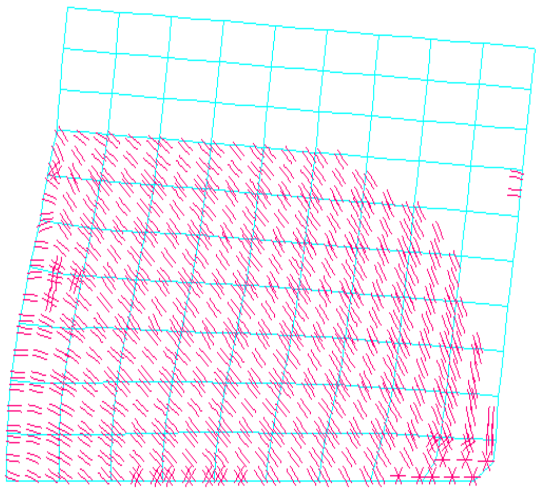

a) Deflected Shape and Crack Pattern

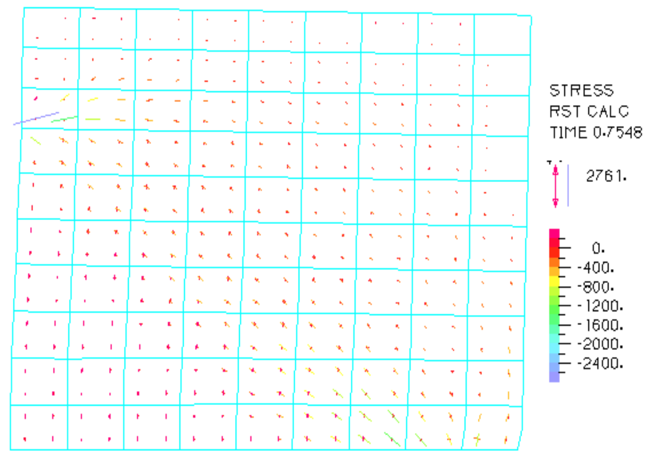

b) Masonry Principal Stresses

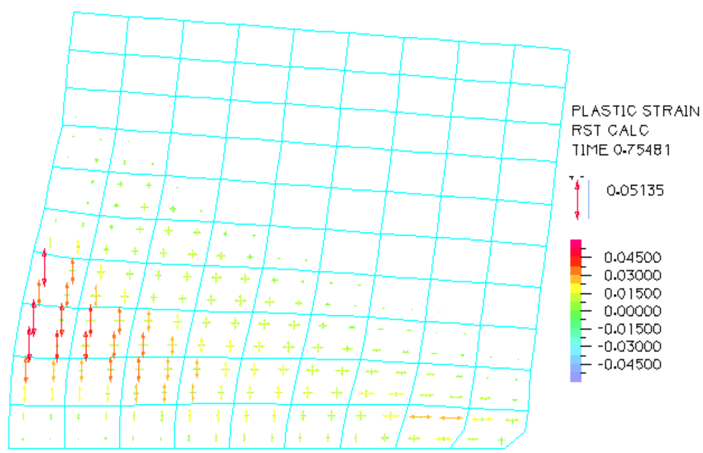

c) Steel Plastic Strain

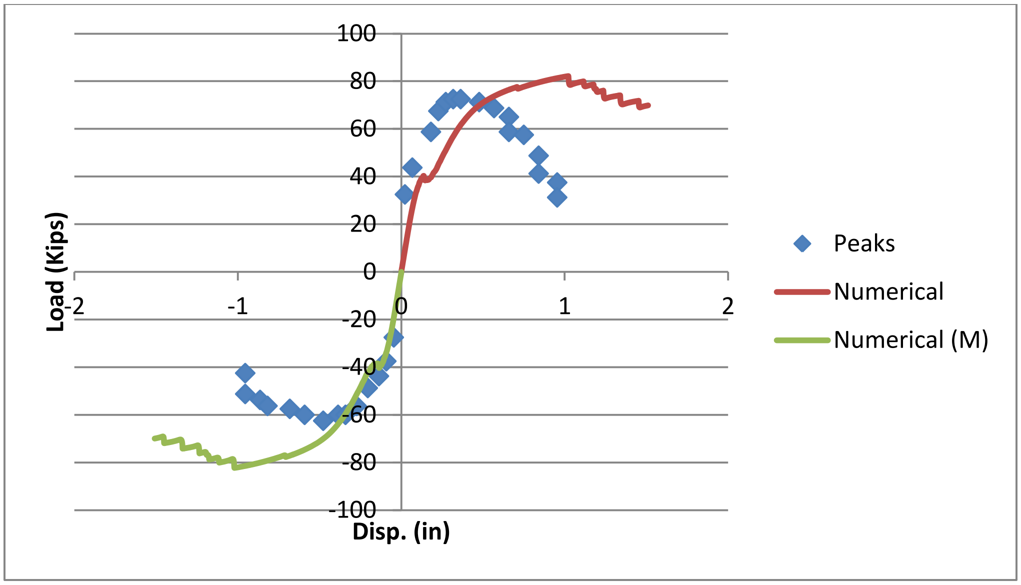

e) Comparison between FE and experimental results

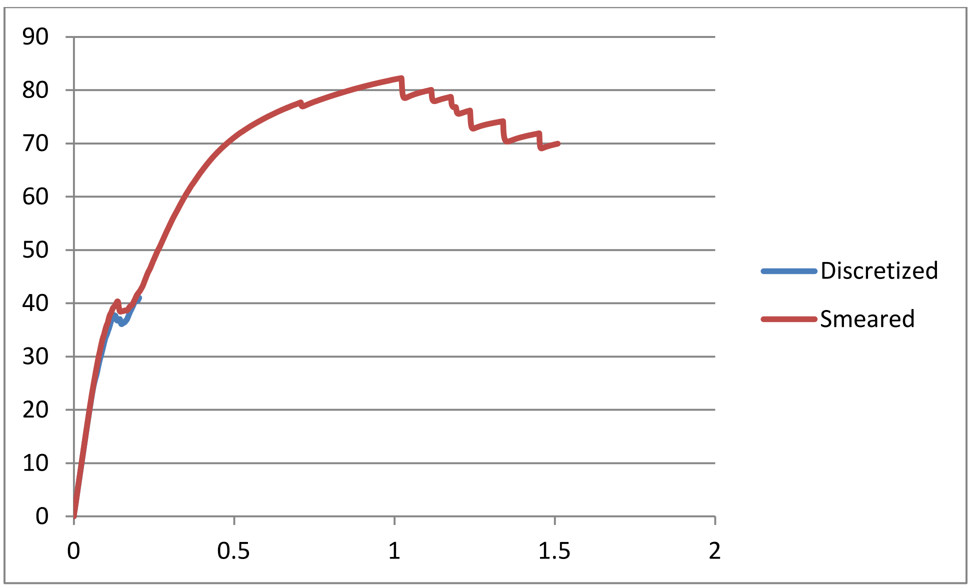

f) Comparison between FE Discretized and Smeared Models

Figure 4.8 Wall 8 (1/2 Spacing Mesh) Results

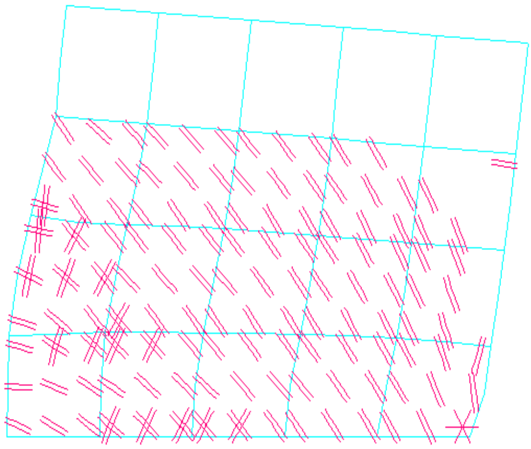

a) Deflected Shape and Crack Pattern

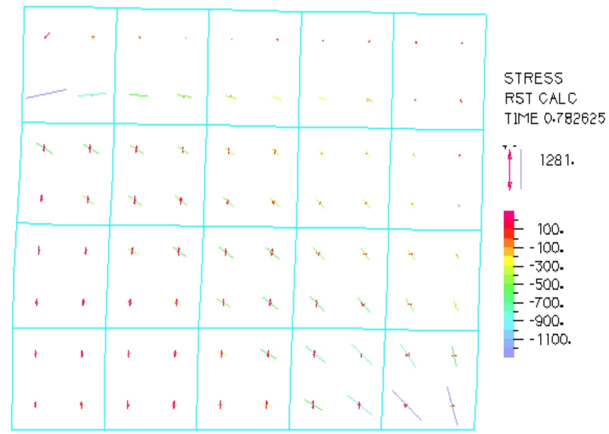

b) Masonry Principal Stresses

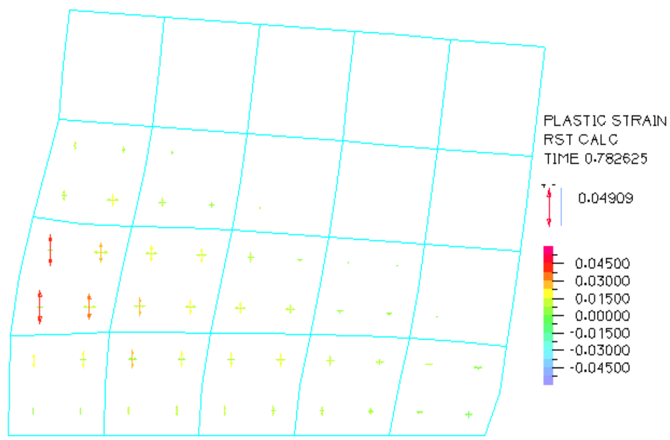

c) Steel Plastic Strain

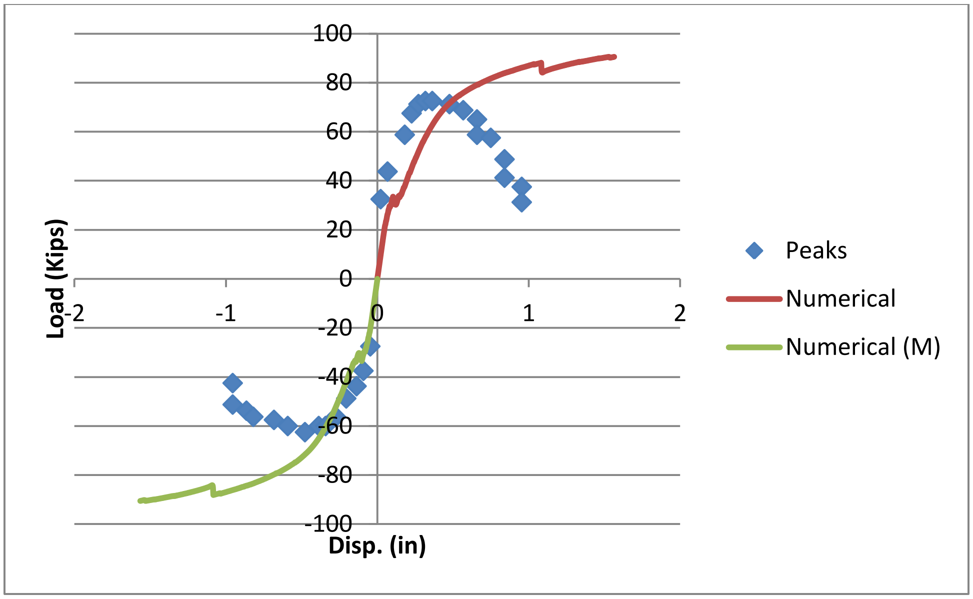

e) Comparison between FE and experimental results

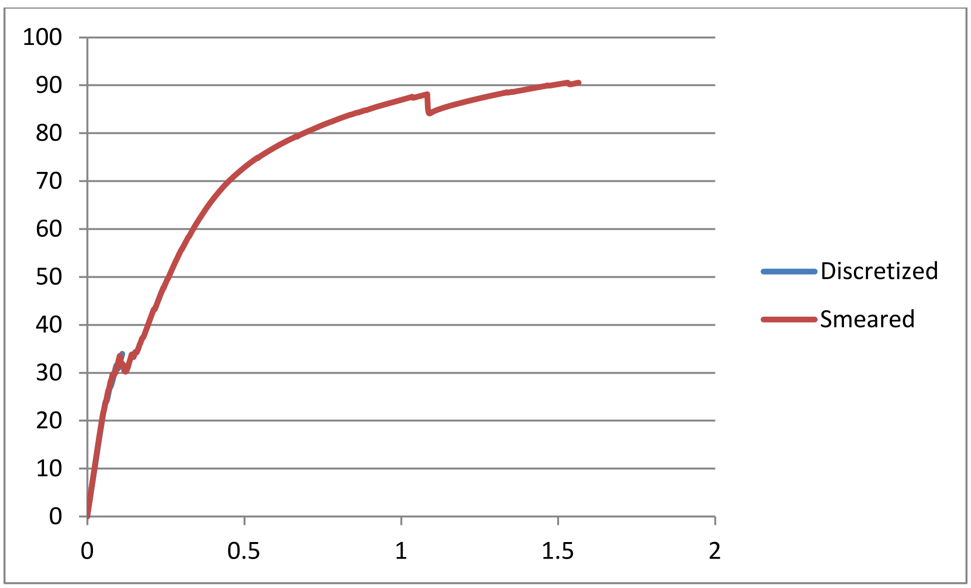

f) Comparison between FE Discretized and Smeared Models

Figure 4.9 Wall 8 (Spacing Mesh) Results

4.6 Discussion

The plots in Figures [4.4-4.9](e) show a strong correlation between results for the discretized steel finite element model of reinforced masonry shear wall specimens and those for the equivalent smeared steel finite element models. The plots also show that, as with the discretized model, the smeared model is not affected by mesh size other than that coarse meshes tend to progress further than fine meshes, especially for walls dominated by shear failure. Neither modeling approach was able to accurately trace the descending part of the load-displacement curve.

Again, In order to control the fictitious damping effect on the model and to predict the wall displacement at peak load, the calculated failure load from Table 3.3 can be used. If the model was unable to develop a peak value of load (ND), increasing the fictitious damping coefficient will allow the solution to progress further. However, increased damping may result in unrealistic behavior. In Table 3.5, the displacement values from the finite element models at calculated peak load are given and compared to those from the experimental tests. The displacement associated with these loads varies from the experimental data by 20-67%. The variance in results is higher than that of the discretized model because smearing of the steel caused yielding of the wall to occur sooner, resulting in higher displacement at peak load.

Table 4.2 Peak Load Displacements

Specimens	Experimental PLD (in)	Predicted PLD (in) (Var. %)		
		¼ spacing mesh	½ spacing mesh	Spacing mesh
1	1.1	ND	1.64 (49.1)	1.44 (30.9)
2	0.55	ND	0.84 (52.7)	0.7 (27.3)
3	0.7	0.26 (62.8)	0.41 (41.4)	0.4 (42.9)
4	0.59	0.79 (33.9)	0.98 (66.1)	ND
5	0.57	ND	0.88 (54.4)	0.73 (28.1)
6	0.95	ND	1.25 (31.6)	1.15 (21.1)
7	0.89	ND	ND	ND
8	0.27	ND	0.45 (66.7)	0.43 (59.3)

The equivalent smeared models were better able to overcome the numerical difficulties exhibited by the discretized models for the shear dominated wall specimens. This is likely because, for the former, all finite elements were influenced by the reinforcement and the effect of masonry cracking was distributed. For the latter, masonry elements without discrete bars experienced a large reduction in stress capacity and stiffness when they cracked, which led to an early numerical breakdown of the solution.

Although detailed steel/masonry interaction is beyond the simulation capability of the smeared model, the general crack pattern and steel yielding zones were accurately depicted with much less time required for model preparation and computer execution than for the discrete model.

CHAPTER FIVE
SUMMARY AND CONCLUSIONS

5.1 Summary

Scaling techniques for the constitutive relations of reinforced masonry shear walls to account for initial cracking were developed to simplify the construction of finite element models for their analysis. These techniques provide solutions for macro modeling of these walls that are valid up to the point of yielding of the reinforcement or gross cracking of the masonry.

For considering the macro scale modeling of reinforced masonry walls beyond the elastic range, the masonry was assumed to have constitutive relations of a similar form to those of concrete at the macro level. Full nonlinear masonry constitutive relations were obtained by scaling, in terms of strains, concrete relations with the ratio of their initial moduli of elasticity.

Steel reinforcement was smeared in an orthotropic element, with properties obtained from stress scaling of the original steel layout, to represent the different reinforcement ratios in both horizontal and vertical directions. This element, including plastic deformation, was overlaid on an identical masonry element.

When compared with experimental results and more detailed finite element results, models composed of the proposed elements showed good agreement with regard to initial cracked stiffness and peak load capacity, when it was attained. The deformation of shear wall specimens at failure was estimated by evaluating displacement at the peak load indicated by existing LRFD design provisions. The values predicted by the discretized models were within experimental accuracy, while those from the smeared models over predicted displacement at peak load due to premature yielding of the steel. Their behavior was insensitive to mesh size and consistent results were obtained for meshes that were relatively coarse. They successfully predicted the performance of walls with various aspect ratios, steel reinforcement patterns, and axial load.

Finally, it is important to mention that both models require using fictitious dynamics with them in order to overcome the instability that results from cracking. This damping does not have an effect on the load-displacement path, but it does give the model the ability to progress further with load/displacement. However, even the fictitious damping did not enable the model to predict the descending part of the load-displacement behavior.

5.2 Conclusions

The proposed simplified modeling techniques appear to be adequate to reduce model construction and solution time. The discretized steel model shows significant ability to predict masonry shear wall behavior, even with very coarse meshing. The smeared steel model provided similar results and was more robust than the discretized steel model in spite of the fact that it only required a fraction of the detailing effort and solution time. Also, the proposed masonry constitutive relationship, based on strain scaling of a standard concrete model, was shown to be a good representation for the macro behavior of masonry.

This simplified representation of masonry shear walls can be used as a part of a full building model. Most practicing engineers should have the ability to use these models to examine the wall behavior, as a part of the entire structure, and check their design. Also, they need only the masonry prism compressive stress and steel design stress properties to set up the material constitutive relations.

Both models are capable of predicting masonry shear wall behavior for relatively long or short walls, even with relatively coarse meshes. Compared with experimental tests, they were shown to be able to represent both flexural and shear response, with and without the effect of axial load. These features make them more appropriate for nonlinear analysis than ordinary or deep beam theories.

The biggest limitation to widespread use of this element for masonry shear wall analysis may be the capabilities required of the finite element software. A full nonlinear failure analysis requires a multidimensional concrete constitutive model, an elastio-plastic orthotropic material model, and some means to progress beyond initial localized cracking. For other, more basic software, the initial masonry modulus of elasticity could be used with the steel elastic modulus to simulate stiffness and approximately estimate the behavior prior to steel yielding or gross masonry cracking.

5.3 Further Research

The scope of this research was on static nonlinear analysis. More research is required to develop these techniques for cyclic loading or nonlinear dynamic analysis. The developed techniques in this research are based on estimating the effective stiffness for a targeted loading point, which is not the same for the suggested further research. It may require a variable material constitutive relation scaling to be applied at each cycle.

REFERENCES

ADINA Structures Software and Documentation, Version 8.7.2. ADINA R&D, Inc. 2010.

Abboud, B. E., Hamid, A. A., and Harris, H. G. (1996). "Flexural Behavior of Reinforced Concrete Masonry Walls Under Out-of-Plane Monotonic Loads." *ACI Structural Journal*, Vol. 93, no. 3, pp. 327-335.

Afshari, F., and Kaldjian, M. J. (1989). "Finite Element Analysis of concrete Masonry Prisms." ACI Material Journal, Vol. 86, no. 5, pp. 525-530.

American Concrete Institute Committee 318, *Building Code Requirements for Structural Concrete (ACI318-08) and Commentary (ACI318R-08)*. American Concrete Institute, Farmington Hills, MI. 2008.

Asteris, P. G., and Tzamtzis, A. D. (2003). "On The Use of a Regular Yield Surface for the Analysis of Unreinforced Masonry Walls." Electronic Journal of Structural Engineering, Vol. 3, no., pp. 23-42.

Balakrishnan, S., and Murray, D. W. (1988). "Concrete Constitutive Model for NLFE Analysis of Structures." *Journal of Structural Engineering*, Vol. 114, no. 7, pp. 1449-1466.

Barbosa, C. S., and Hanai, J. B. (2009). "Strength and Deformability of Hollow Concrete Blocks: Correlation of Block and Cylindrical Sample Test Results." *IBRACON Structures and Materials Journal*, Vol. 2, no. 1, pp. 85-99.

Chaimoon, K., and Attard, M. M. (2007). "Modeling of Unreinforced Masonry Walls Under Shear and Compression." *Engineering Structures*, Vol. 29, no. 9, pp. 2056-2068.

Cheema, T. S., and Klingner, R. E. (1986). "Compressive Strength of Concrete Masonry Prisms." *ACI Journal*, Vol. 83, no. 1, pp. 88-97.

Da Porto, F., Guidi, G., Garbin, E., and Modena, C. (2010). "In-Plane Behavior of Clay Masonry Walls: Experimental Testing and Finite-Element Modeling." *Journal of Structural Engineering*, Vol. 136, no. 11, pp. 1379-1392.

Dhanasekar, M., and Shrive, N. G. (2002). "Strength and Deformation of Confined and Unconfined Grouted Concrete Masonry." *ACI Structural Journal*, Vol. 99, no. 6, pp. 819-826.

Drysdale, R. G., and Hamid, A. A. (1983). "Capacity of Concrete Block Masonry Prisms Under Eccentric Compressive Loading." *ACI Journal*, Vol. 80, no. 2, pp. 102-108.

Drysdale, R. G., Heidebrecht, A. C., and Hamid, A. A. (1979). "Tensile Strength of Concrete Masonry." *Journal of Structural Engineering*, Vol. 105, no. 7, pp. 1261-1276.

Drysdale, R. G., and Khattab, M. M. (1995). "In-Plane Behavior of Grouted Concrete Masonry under Biaxial Tension-Compression." *ACI Structural Journal*, Vol. 92, no. 6, pp. 653-664.

Eikanas, I. K. (2003). "Behavior of Concrete Masonry Shear Walls with Varying Aspect Ratio and Flexure Rerinforcement." Washington State University, Pullman.

El-Dakhakhni, W. W., Drysdale, R. G., and Khattab, M. M. (2006). "Multilaminate Macromodel for Concrete Masonry: Formulation and Verification." Journal of Structural Engineering, Vol. 132`, no. 12, pp. 1984-1996.

El-Metwally, S. E. E., Ashour, A. F., and Chen, W. F. (1991). "Behavior and Strength of Concrete Masonry Walls." *ACI Structural Journal*, Vol. 88, no. 1, pp. 42-48.

Feenstra, P. H., and De Borst, R. (1995). "Constitutive Model for Reinforced Concrete." *Journal of Engineering Mechanics*, Vol. 121, no. 5, pp. 587-595.

Gambarotta, L., and Lagomarsino, S. (1997). "Damage Models for the Seismic Response of Brick Masonry Shear Walls. Part I: The Mortar Joint Model and Its Applications." *Earthquake Engineering and Structural Dynamics*, Vol. 26, no. 4, pp. 423-439.

Haach, V. G., Vasconcelos, G., and Loureco, P. B. (2011). "Parametrical Study of Masonry Wall Subjected to In-Plane Loading Through Numerical Modeling." *Engineering Structures*, Vol. 33, no. 4, pp. 1377-1389.

Hatzinikolas, M., Longworth, J., and Warwaruk, J. (1980). "Failure Modes for Eccentrically Loaded Concrete Block Masonry Walls." *ACI Journal*, Vol. 77, no. 4, pp. 258-263.

Holm, T. A. (1987). "structural Properties of Block Concrete." 1st Noth American Masonry Conference, 15 pp.

Horton, R. T., and Tadros, M. K. (1990). "Deflection of Reinforced Masonry Members." *ACI Structural Journal*, Vol. 87, no. 4, pp. 453-463.

Karapitta, L., Mouzakis, H., and GCarydis, P. (2011). "Explicit Finite-Element Analysis for the In-Plane Cyclic Behavior of Unreinforced Masonry Structures." *Earthquake Engineering and Structural Dynamics*, Vol. 40, no. 2, pp. 175-193.

Kazaz, I., Yakut, A., and Gulkan, P. (2006). "Numerical Simulation of Dynamic Shear Wall Tests: A Benchmark Study." *Computers and Structures*, Vol. 84, no. 8, pp. 549-562.

Klingner, R. E. (2010). *Masonry Structure Design*, McGraw Hill,560.pp

Legeron, F., Paultre, P., and Mazars, J. (2005). "Damage Mechanics Modeling of Nonlinear Seismic Behavior of Concrete Structures." Journal of Structural Engineering, Vol. 131, no. 6, pp. 946-955.

Loureco, P. B., and Rots, J. G. (1997). "Multisurface Interface Model for Analysis of Masonry Structures." *Journal of Engineering Mechanics*, Vol. 123, no. 7, pp. 660-668.

Loureco, P. B., Rots, J. G., and Blaauwendraad, J. (1998). "Countinuum Model for Masonry: Parameter Estimation and Validation." Journal of Structural Engineering, Vol. 124, no. 6, pp. 642-652.

Mojsilovic, N., and Marti, P. (1997). "Strength of Masonry Subjected to Combined Actions." ACI Structural Journal, Vol. 96, no. 4, pp. 633-640.

Nilson, A. H. (1987). *Design of Prestressed Concrete*, 2nd edition. Wiley, New York,592.pp

Nilson, A. H., Darwin, D., and Dolan, C. W. (2003). *Design of Concrete Structures*, 14th Edition. McGraw Hill,795.pp

Priestley, M. J. N. (1986). "Seismic Design of Concrete Masonry Shearwalls." *ACI Structural Journal*, Vol. 83, no. 1, pp. 58-68.

Priestley, M. J. N., and Elder, D. M. (1983). "Stress-Strain Curves for Unconfined and Confined Concrete Masonry." *ACI Journal*, Vol. 80, no. 3, pp. 192-201.

Ramamurthy, K., Sathish, V., and Ambalavanan, R. (2000). "Compressive Strength Prediction of Hollow Concrete Block Masonry Prisms." *ACI Structural Journal*, Vol. 97, no. 1, pp. 61-67.

Selby, R. G., and Vecchio, F. J. (1997). "A Constitutive Model For Analysis of Reinforced Concrete Solids." *Canadia*n Journal of Civil Engineering Vol. 24, no., pp. 460-470.

Sherman, J. (2011). "Effects of Key Parameters on The Performance of Concrete Masonry Shear Walls Under In-Plane Loading." Washington State University, Pullman.

Shing, P. B., Schuller, M., Hoskere, V. S., and Carter, E. (1990). "Flexural and Shear Response of Reinforced Masonry Walls." ACI *Structural Journal*, Vol. 87, no. 6, pp. 646-656.

Stavridis, A., and Shing, P. B. (2010). "Finite-Element Modeling of Nonlinear Behavior of Masonry-Infilled RC Frames." Journal of Structural Engineering, Vol. 136, no. 3, pp. 285-296.

Sutcliffe, D. J., Yu, H. S., and Page, A. W. (2001). "Lower Bound Limit Analysis of Unreinforced Masonry Shear Walls." Computers and Structures, Vol. 79, no. 14, pp. 1295-1312.

Vecchio, F. J. (1990). "Reinforced Concrete Membrane Element Formulations." *Journal of Structural Engineering*, Vol. 116, no. 3, pp. 730-750.

Vecchio, F. J., and Collins, M. P. (1986). "The Modified Compression-Field Theory for Reinforced Concrete Elements Subjected to Shear." *ACI Journal*, Vol. 83, no. 2, pp. 219-231.

Vecchio, F. J., and Selby, R. G. (1991). "Toward Compression-Field Analysis of Reinforced Concrete Solids." *Journal of Structural Engineering*, Vol. 117, no. 20, pp. 1740-1758.

Yamaguchi, E., and Ohta, T. (1993). "Accurate and Efficient Method for Analysis of Reinforced Concrete Structures." *Journal of Structural Engineering*, Vol. 119, no. 30, pp. 2017-2034.

A.1 Discretized Model Results

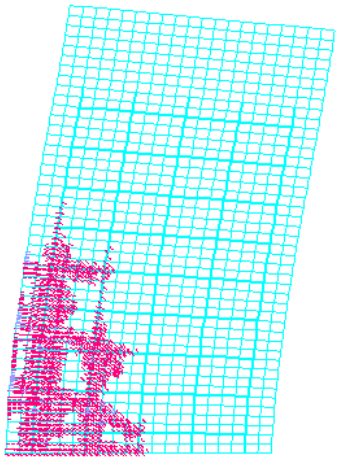

a) Deflected Shape and Crack Pattern

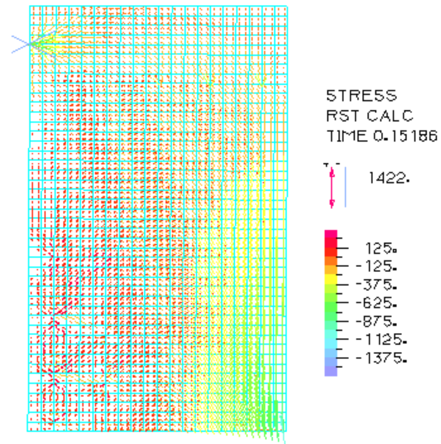

b) Masonry Principal Stresses

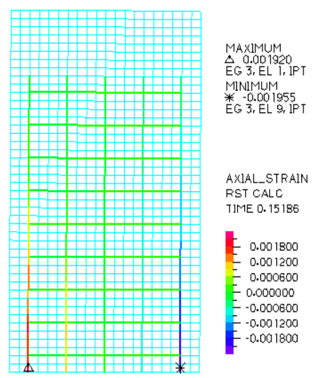

c) Axial Strain in Steel

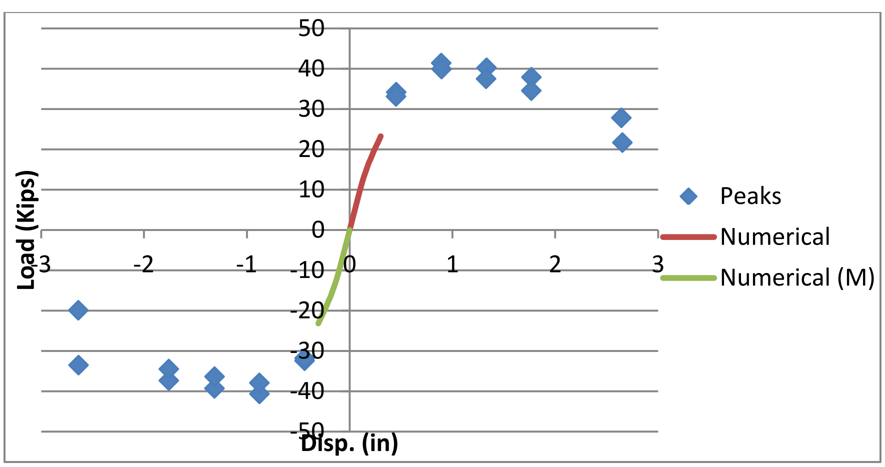

d) Comparison between FE and experimental results

Figure A1.1 Wall 1 (1/4 Spacing Mesh) Results

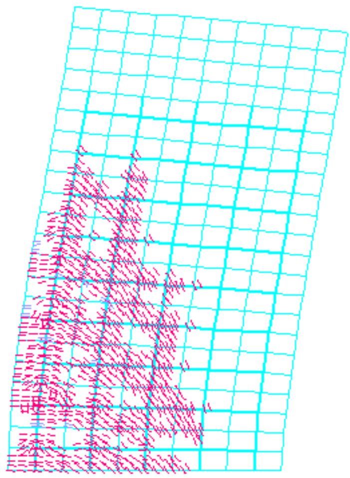

a) Deflected Shape and Crack Pattern

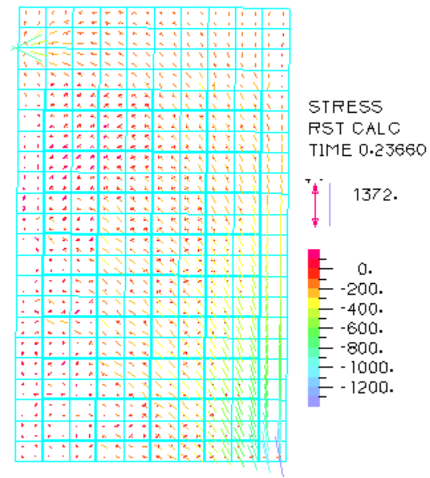

b) Masonry Principal Stresses

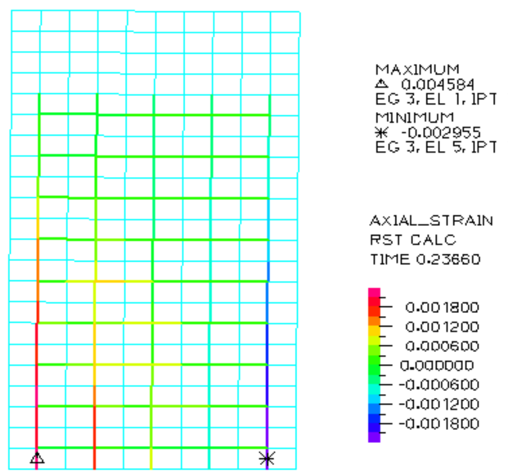

c) Axial Strain in Steel

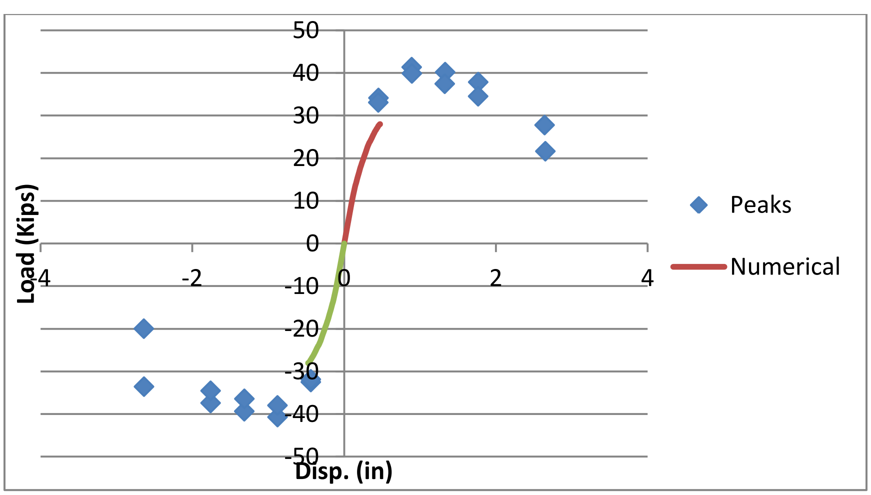

d) Comparison between FE and experimental results

Figure A1.2 Wall 1 (1/2 Spacing Mesh) Results

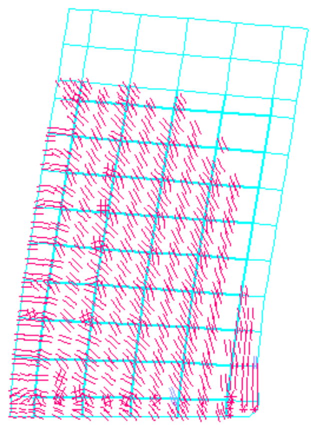

a) Deflected Shape and Crack Pattern

b) Masonry Principal Stresses

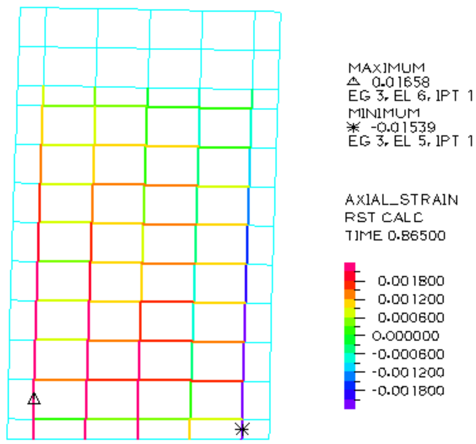

c) Axial Strain in Steel

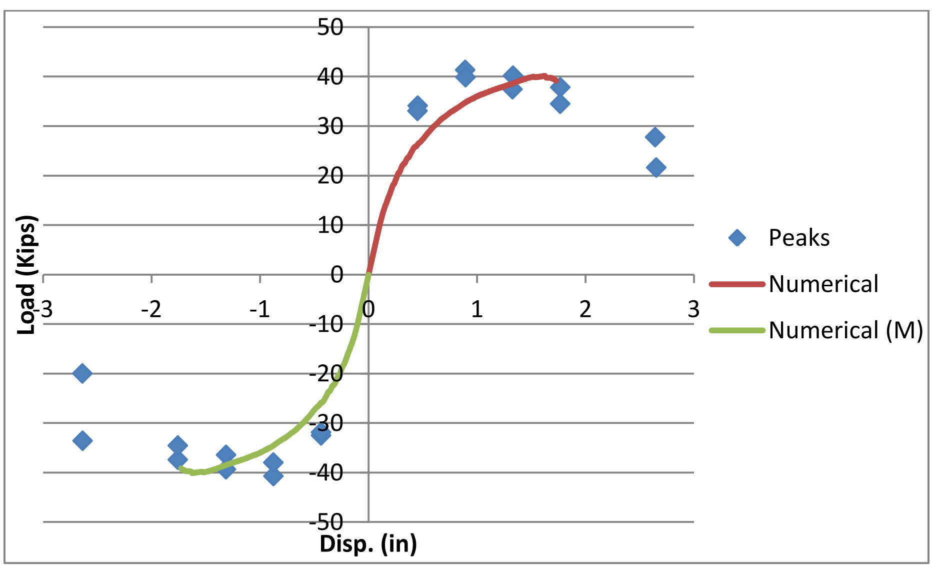

d) Comparison between FE and experimental results

Figure A1.3 Wall 1 (Spacing Mesh) Results

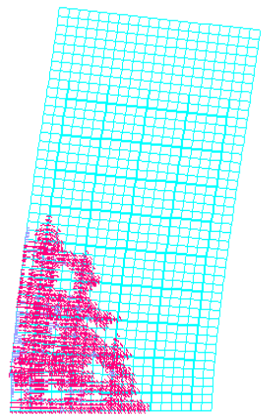

a) Deflected Shape and Cracks Pattern

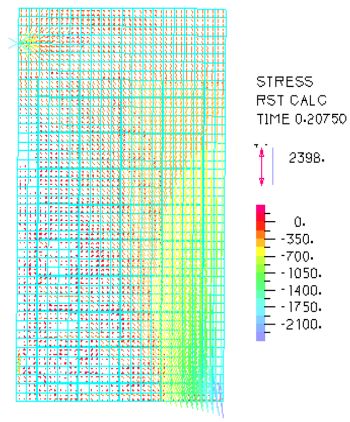

b) Masonry Principal Stresses

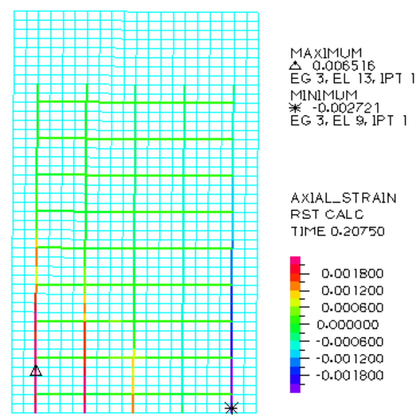

c) Axial Strain in Steel

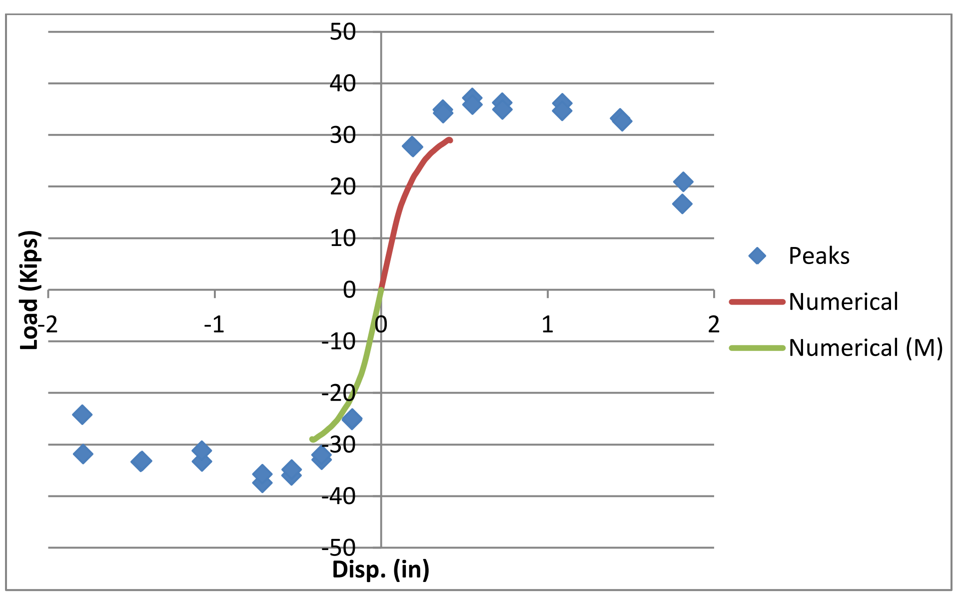

d) Comparison between FE and experimental results

Figure A1.4 Wall 2 (1/4 Spacing Mesh) Results

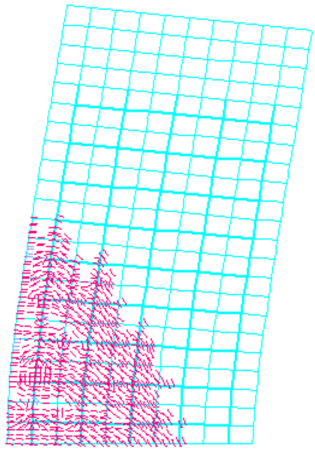

a) Deflected Shape and Cracks Pattern

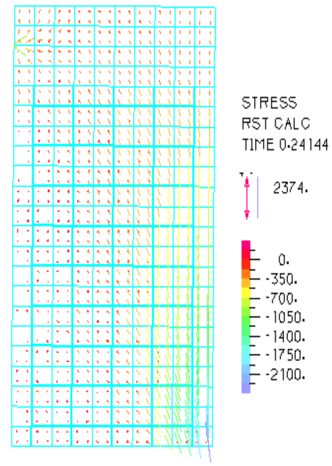

b) Masonry Principal Stresses

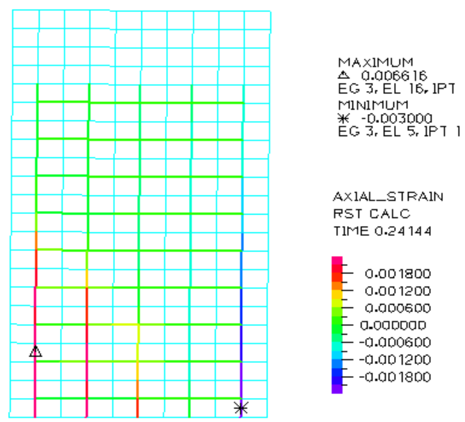

c) Axial Strain in Steel

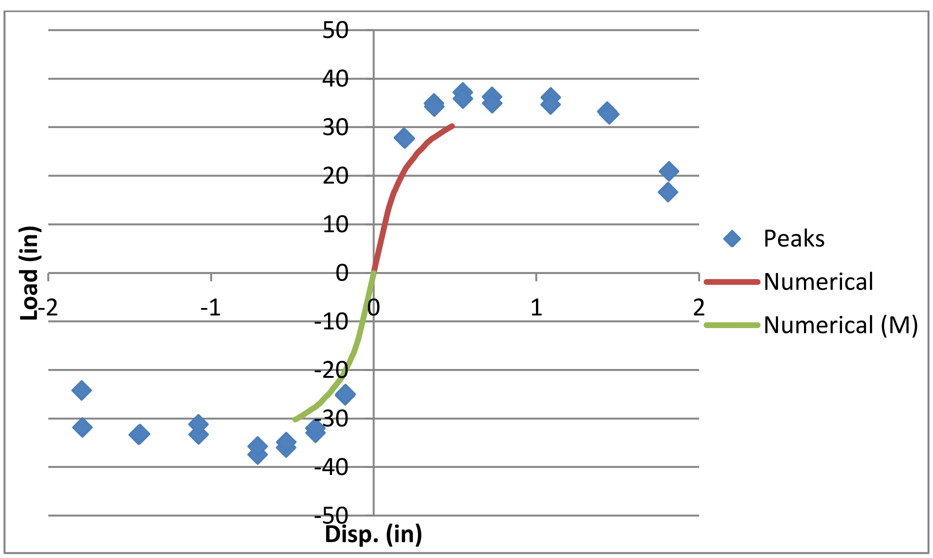

d) Comparison between FE and experimental results

Figure A1.5 Wall 2 (1/2 Spacing Mesh) Results

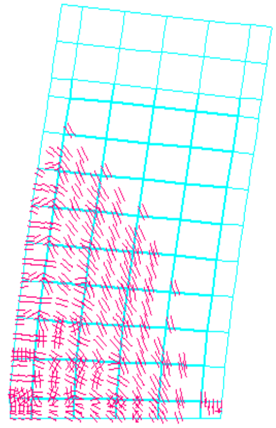

a) Deflected Shape and Crack Pattern

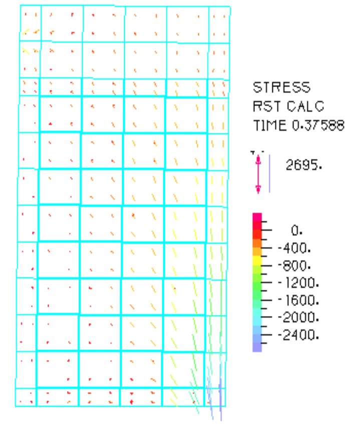

b) Masonry Principal Stresses

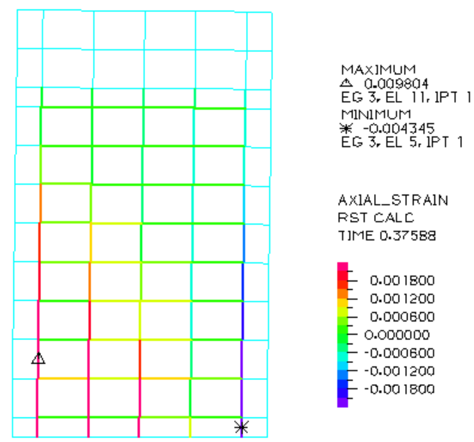

c) Axial Strain in Steel

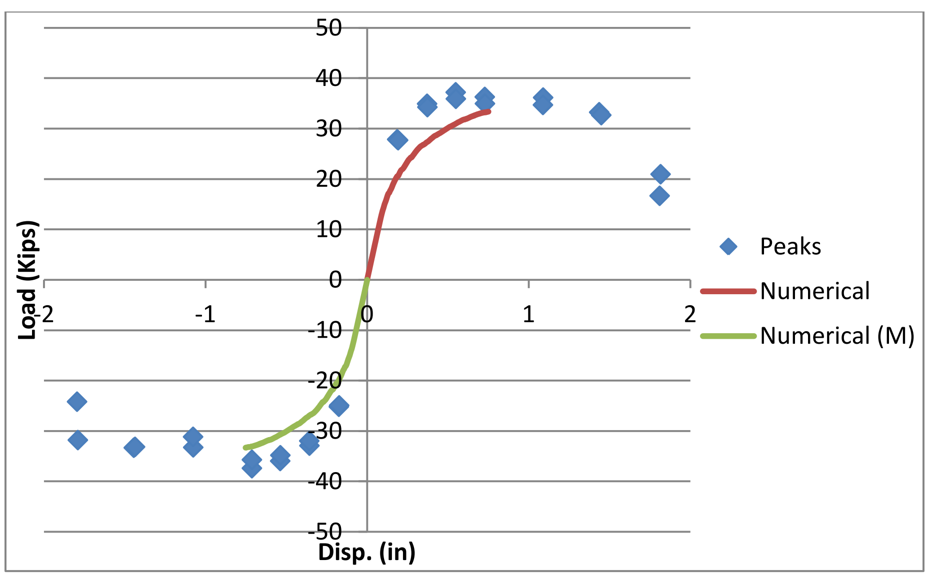

d) Comparison between FE and experimental results

Figure A1.6 Wall 2 (Spacing Mesh) Results

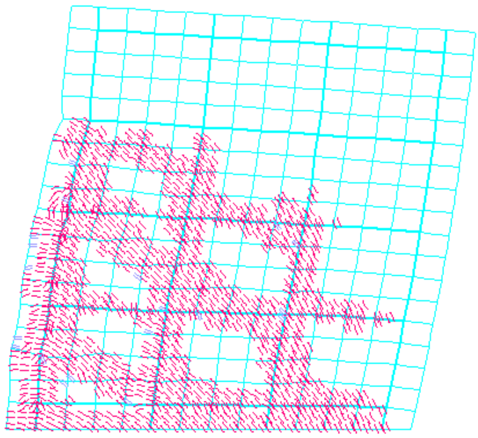

a) Deflected Shape and Crack Pattern

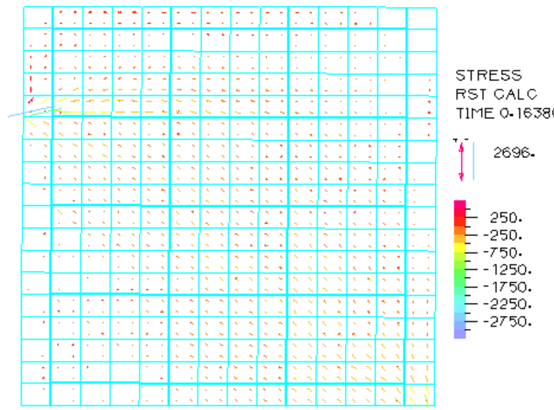

b) Masonry Principal Stresses

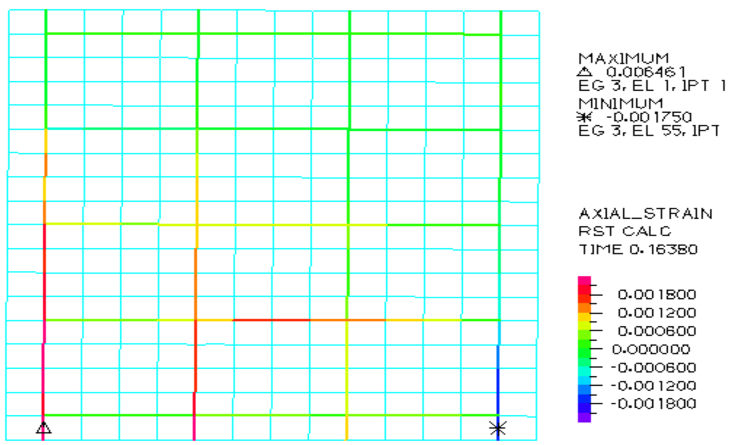

c) Axial Strain in Steel

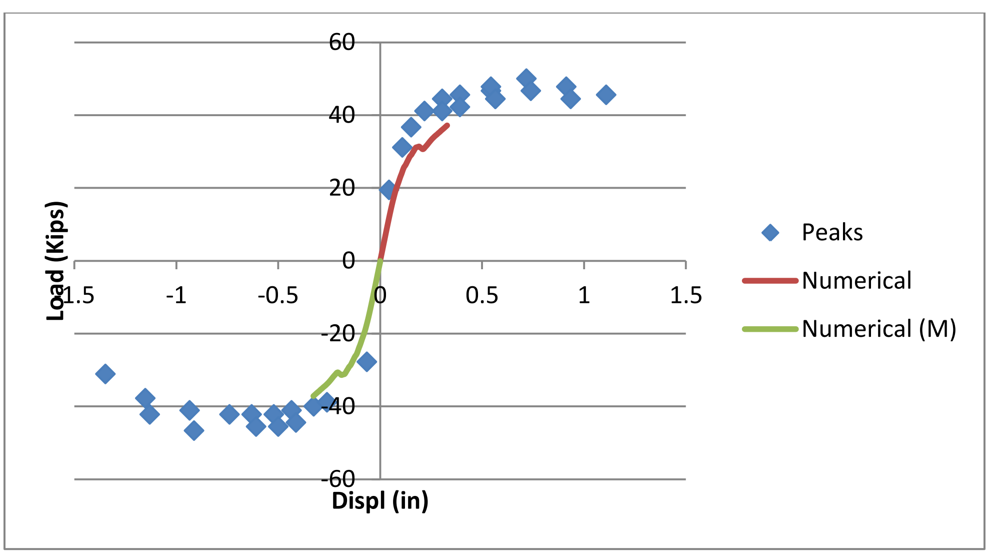

d) Comparison between FE and experimental results

Figure A1.7 Wall 3 (1/4 Spacing Mesh) Results

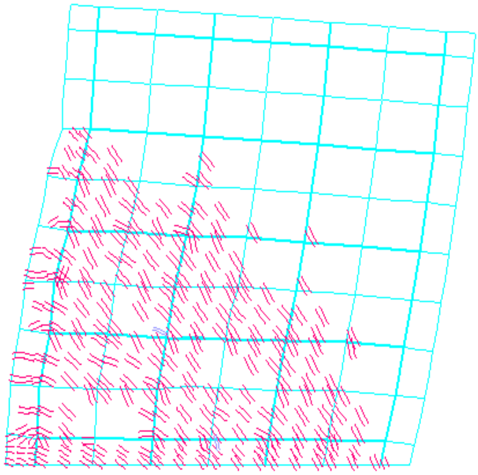

a) Deflected Shape and Cracks Pattern

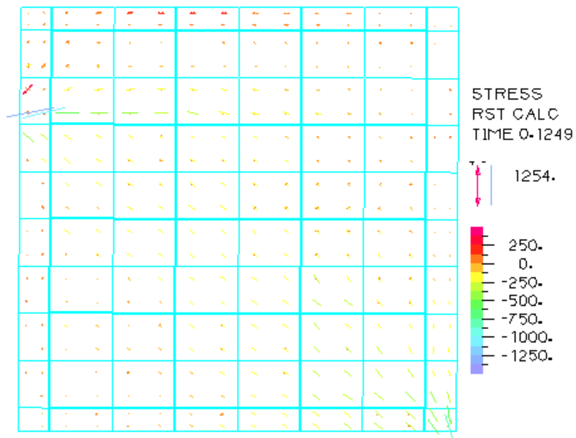

b) Masonry Principal Stresses

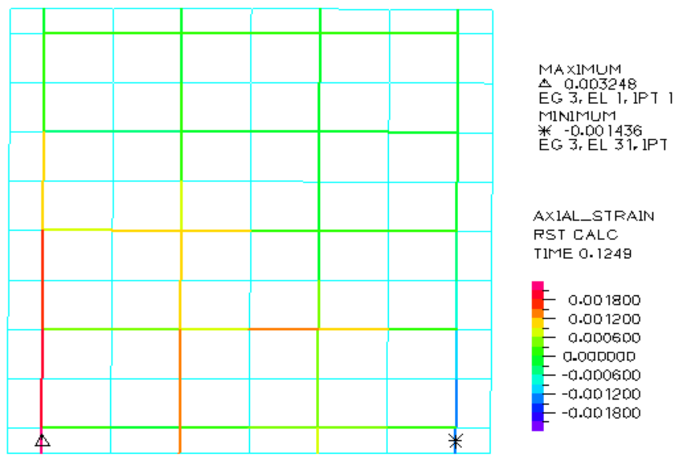

c) Axial Strain in Steel

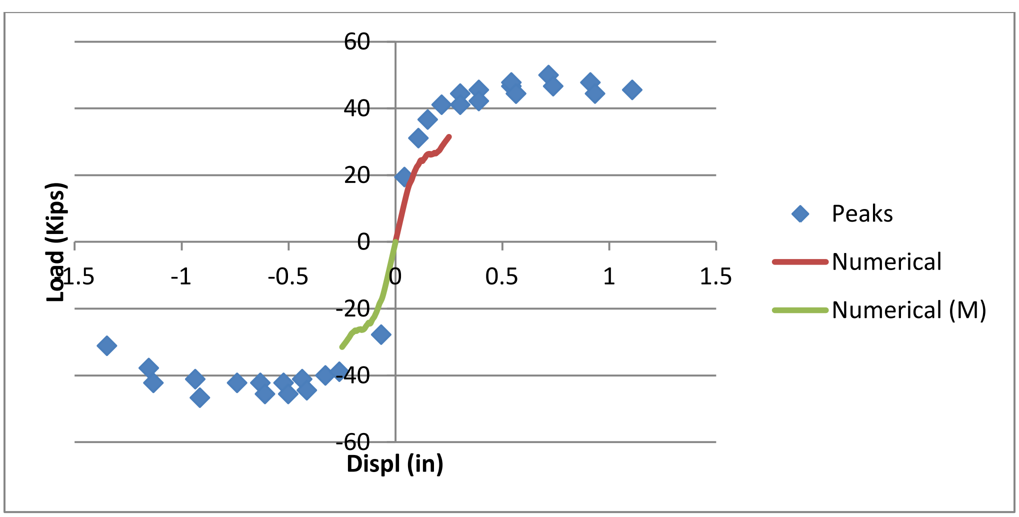

d) Comparison between FE and experimental results

Figure A1.8 Wall 3 (1/2 Spacing Mesh) Results

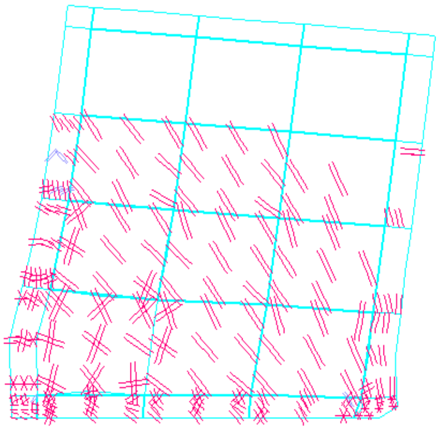

a) Deflected Shape and Crack Pattern

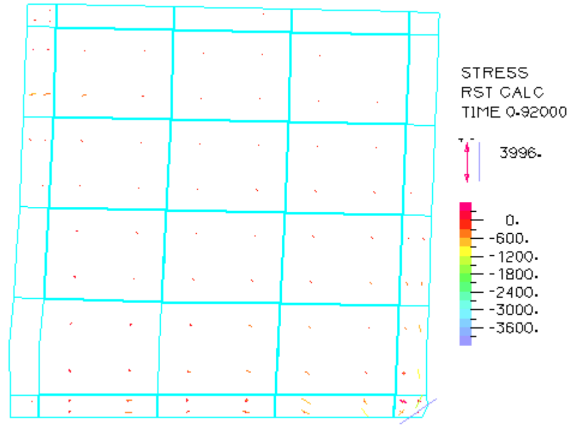

b) Masonry Principal Stresses

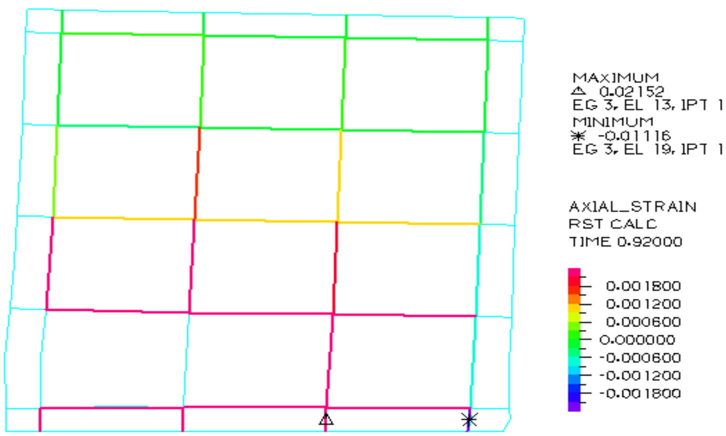

c) Axial Strain in Steel

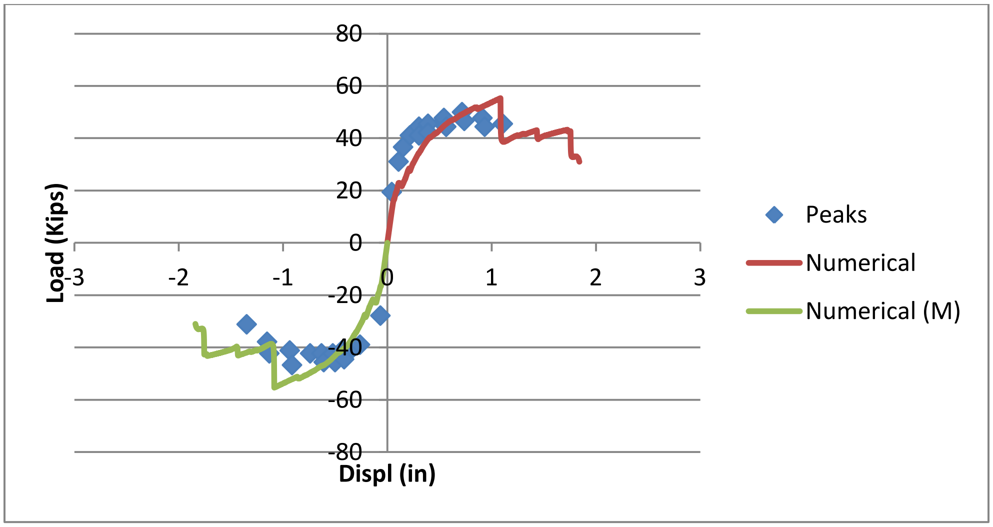

d) Comparison between FE and experimental results

Figure A1.9 Wall 3 (Spacing Mesh) Results

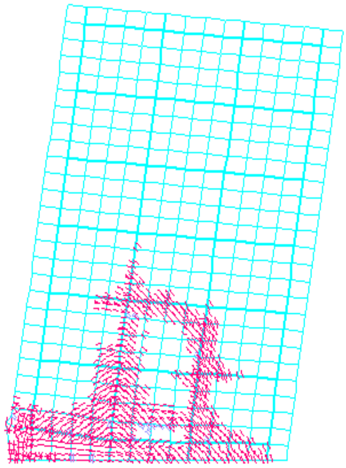

a) Deflected Shape and Crack Pattern

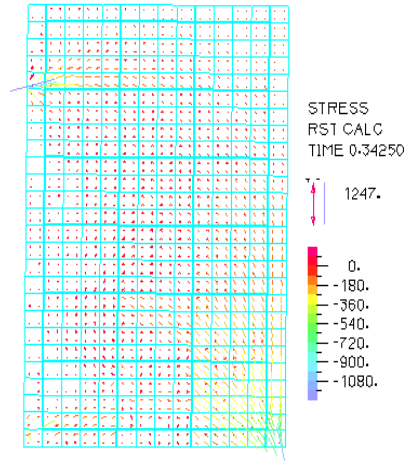

b) Masonry Principal Stresses

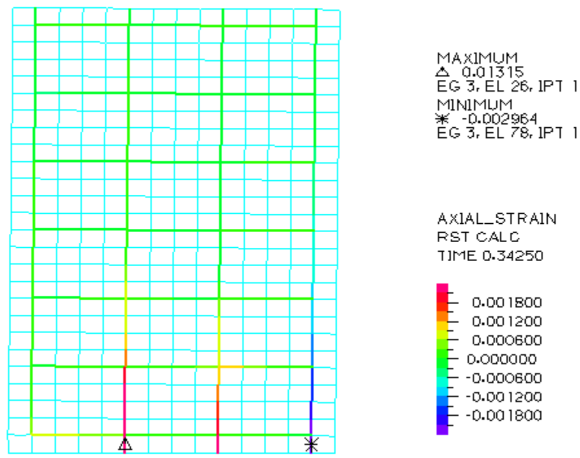

c) Axial Strain in Steel

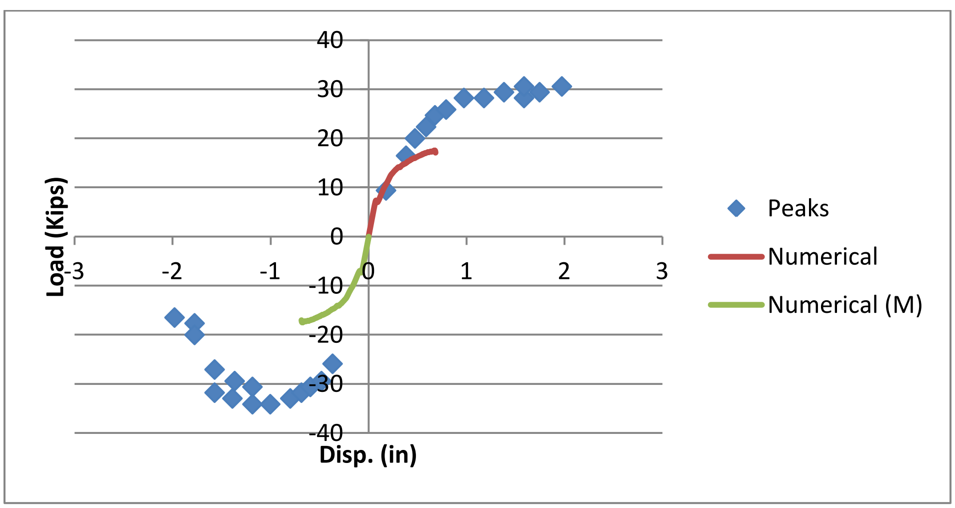

d) Comparison between FE and experimental results

Figure A1.10 Wall 4 (1/4 Spacing Mesh) Results

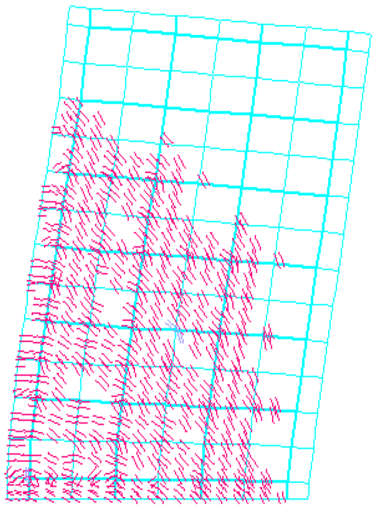

a) Deflected Shape and Crack Pattern

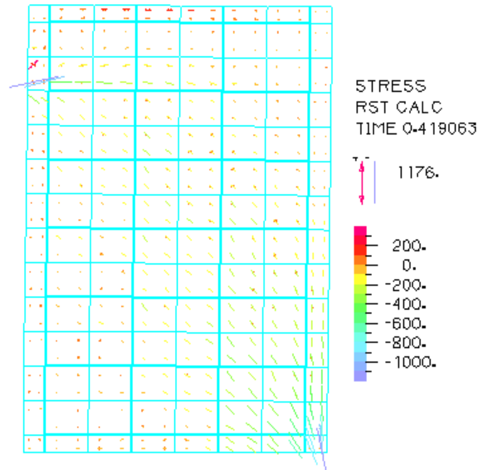

b) Masonry Principal Stresses

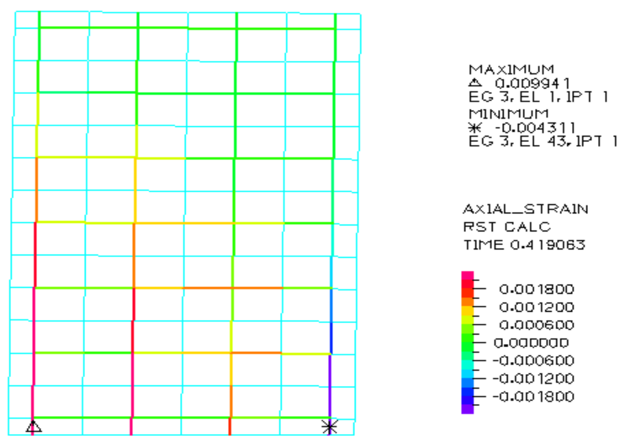

c) Axial Strain in Steel

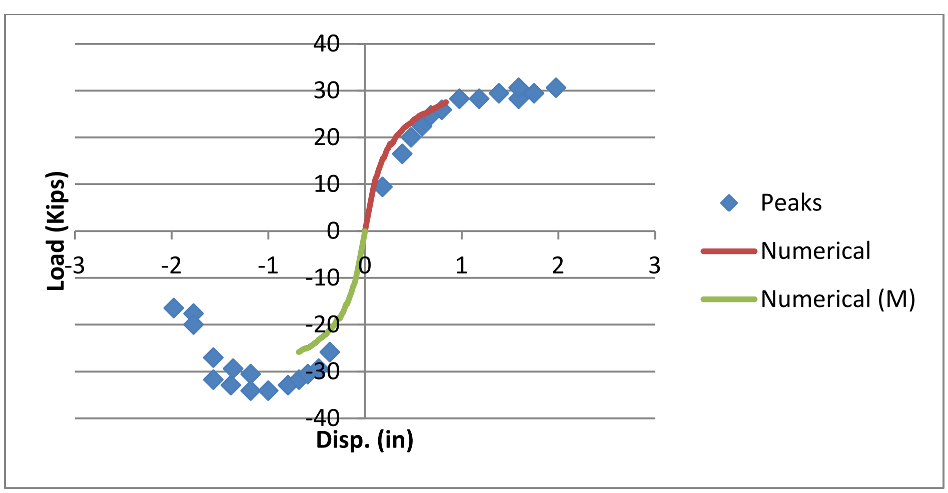

d) Comparison between FE and experimental results

Figure A1.11 Wall 4 (1/2 Spacing Mesh) Results

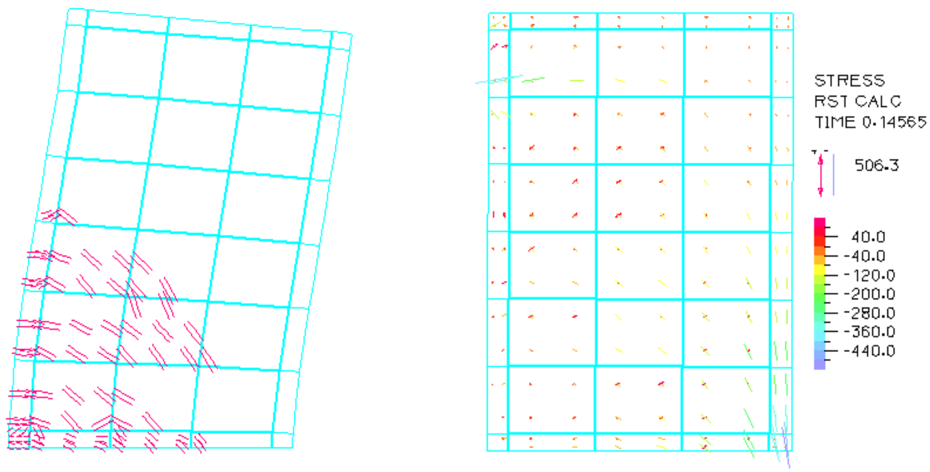

a) Deflected Shape and Crack Pattern b) Masonry Principal Stresses

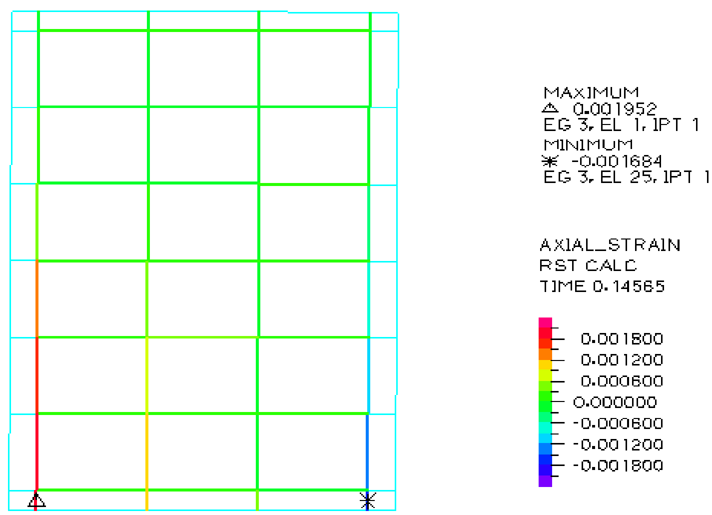

c) Axial Strain in Steel

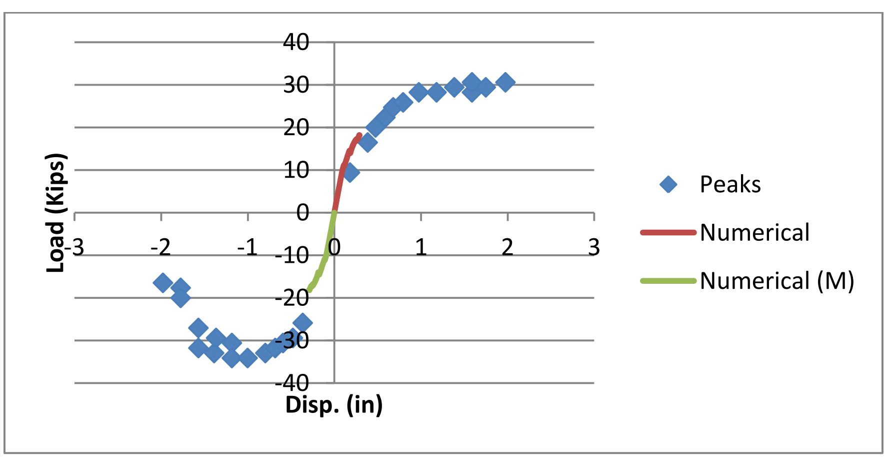

d) Comparison between FE and experimental results

Figure A1.12 Wall 4 (Spacing Mesh) Results

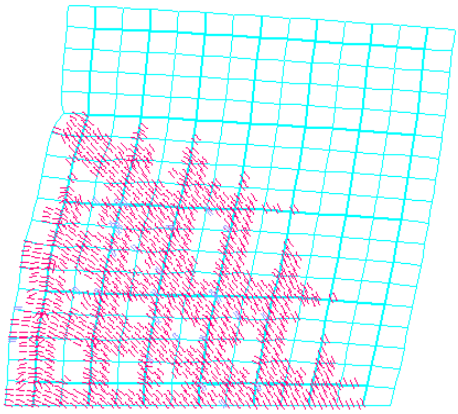

a) Deflected Shape and Crack Pattern

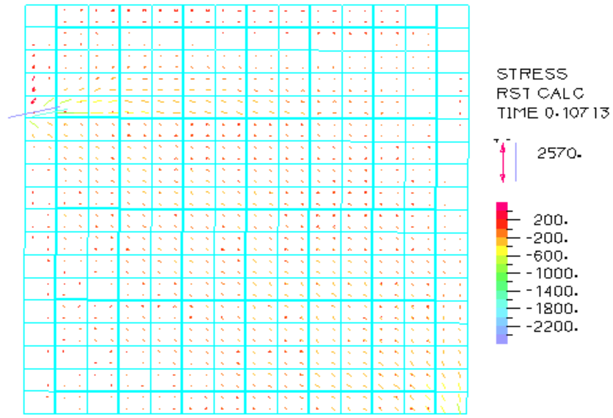

b) Masonry Principal Stresses

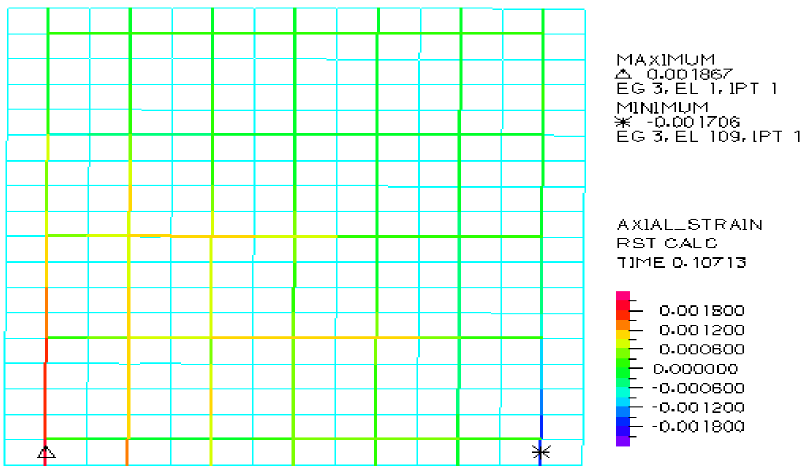

c) Axial Strain in Steel

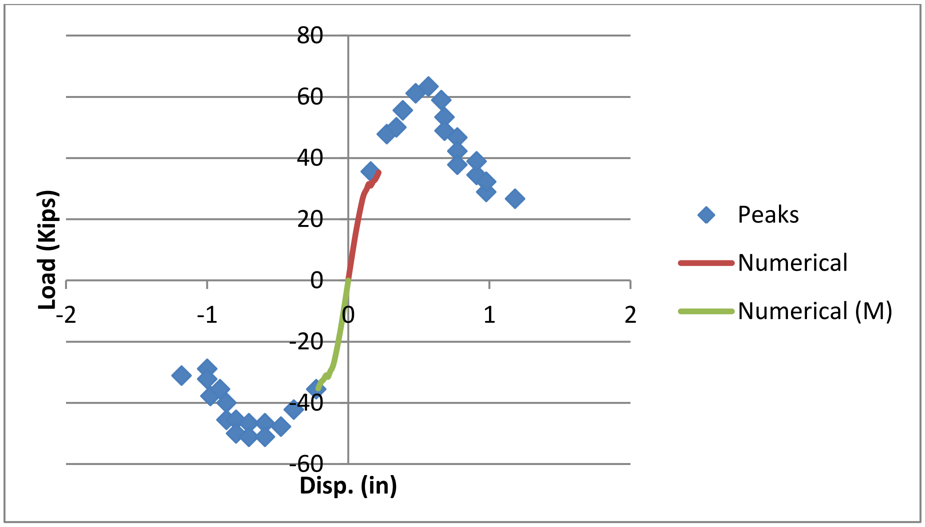

d) Comparison between FE and experimental results

Figure A1.13 Wall 5 (1/4 Spacing Mesh) Results

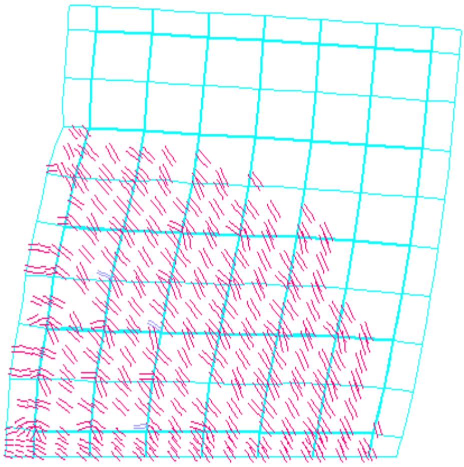

a) Deflected Shape and Crack Pattern

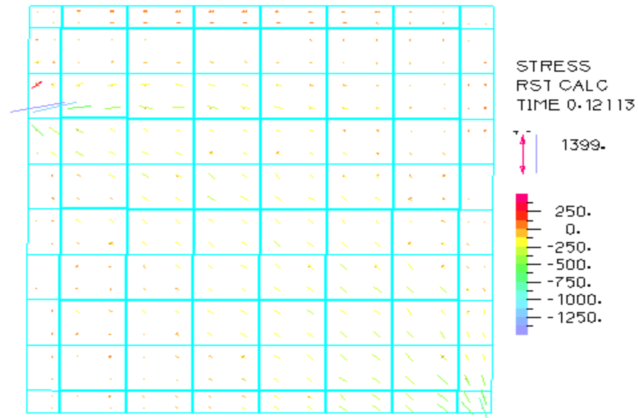

b) Masonry Principal Stresses

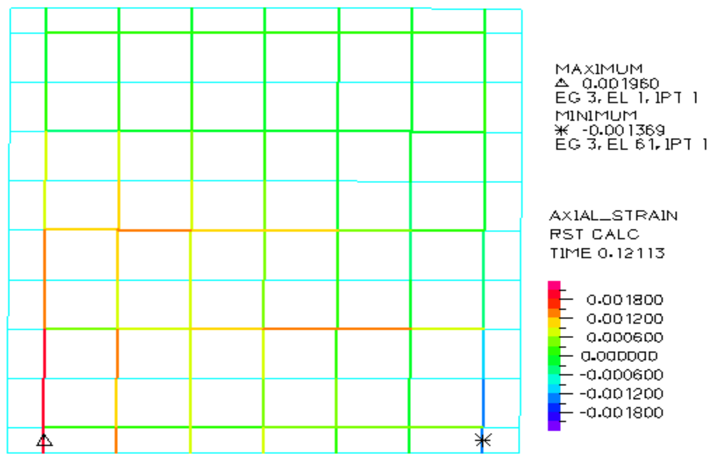

c) Axial Strain in Steel

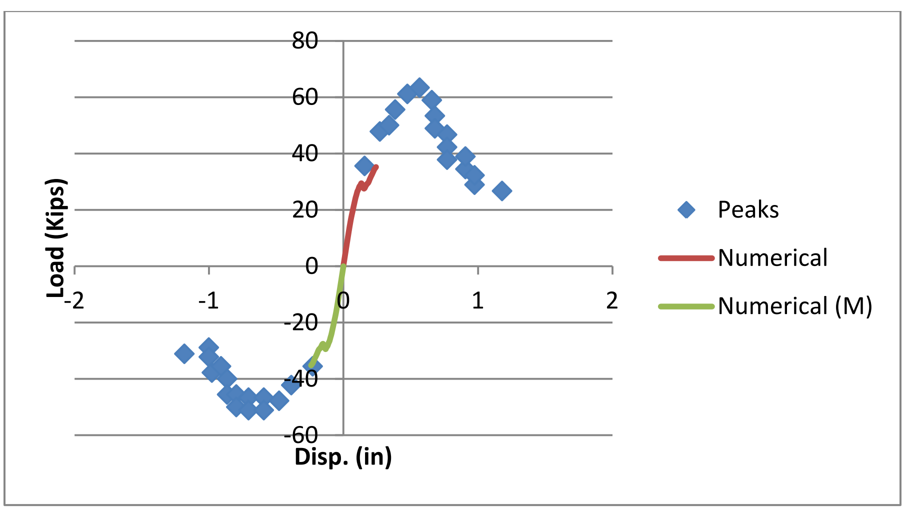

d) Comparison between FE and experimental results

Figure A1.14 Wall 5 (1/2 Spacing Mesh) Results

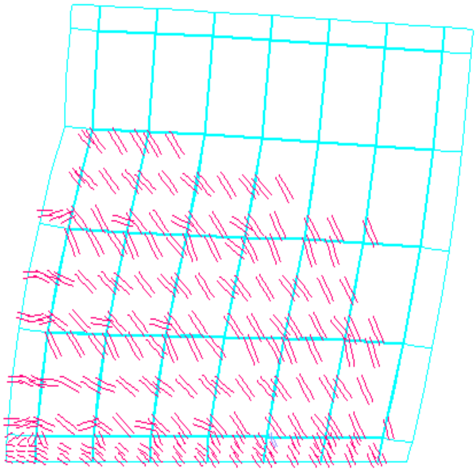

a) Deflected Shape and Crack Pattern

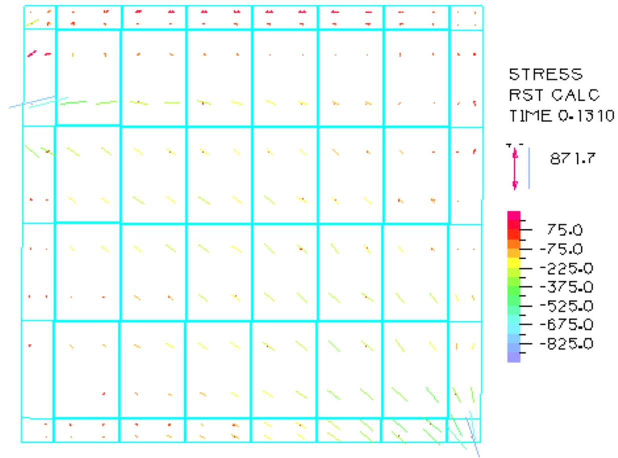

b) Masonry Principal Stresses

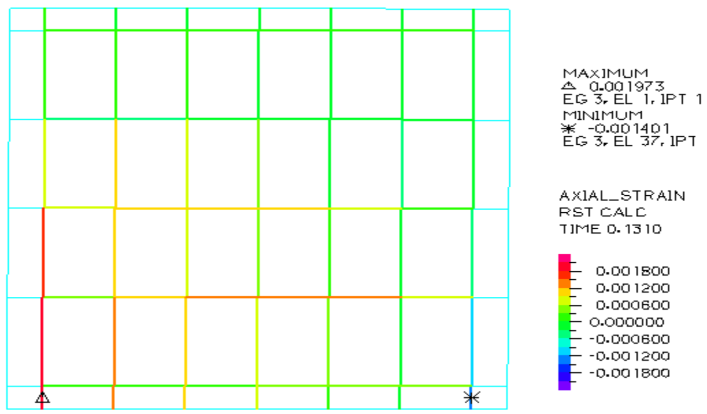

c) Axial Strain in Steel

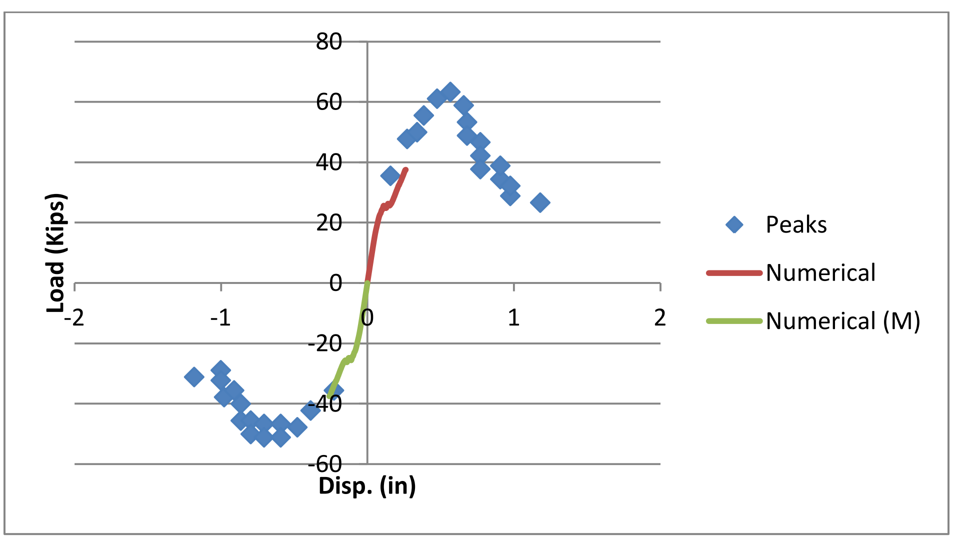

d) Comparison between FE and experimental results

Figure A1.15 Wall 5 (Spacing Mesh) Results

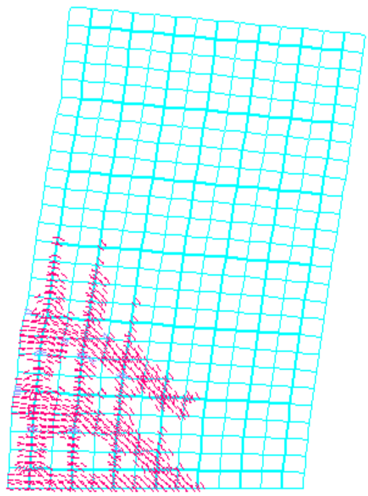

a) Deflected Shape and Crack Pattern

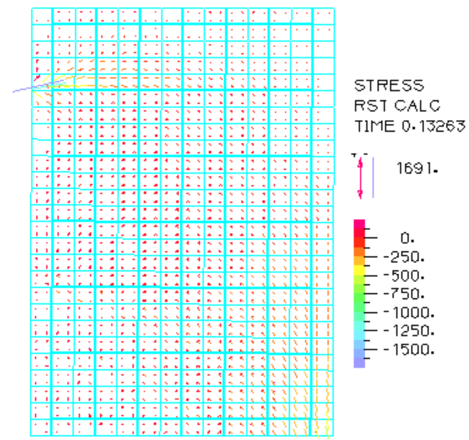

b) Masonry Principal Stresses

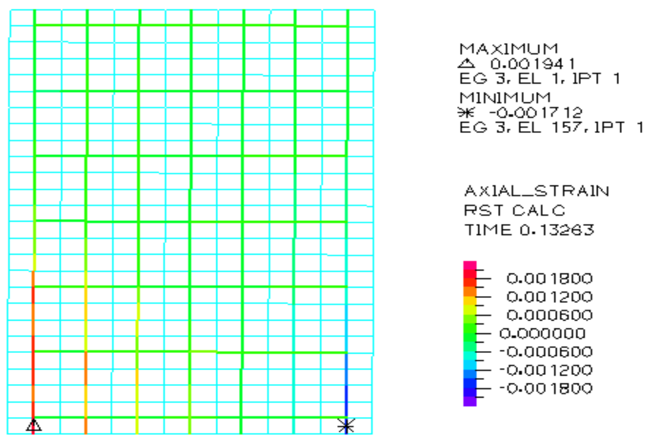

c) Axial Strain in Steel

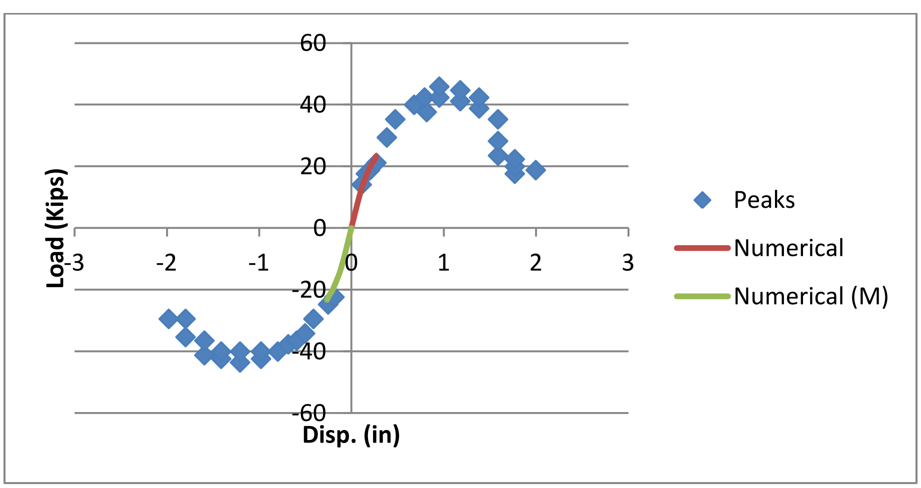

d) Comparison between FE and experimental results

Figure A1.16 Wall 6 (1/4 Spacing Mesh) Results

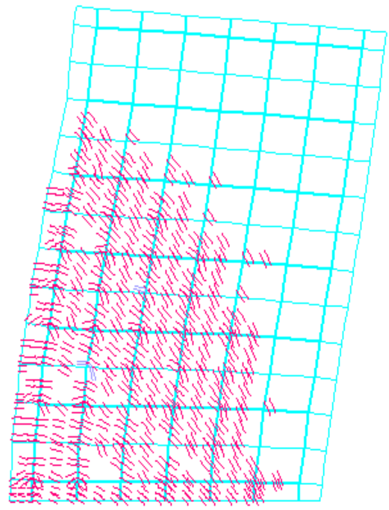

a) Deflected Shape and Crack Pattern

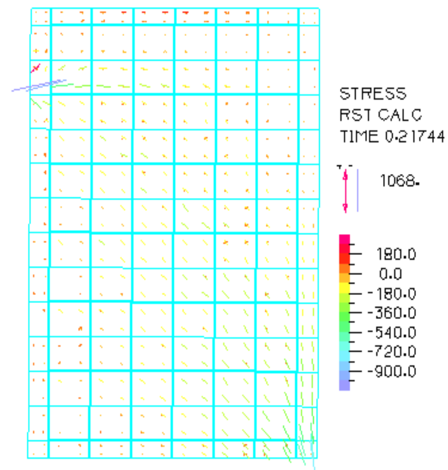

b) Masonry Principal Stresses

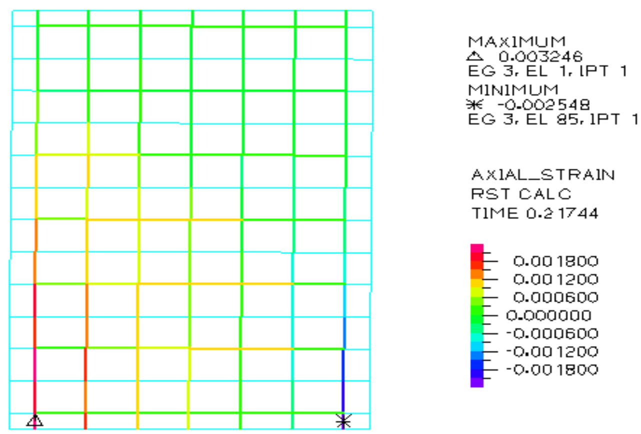

c) Axial Strain in Steel

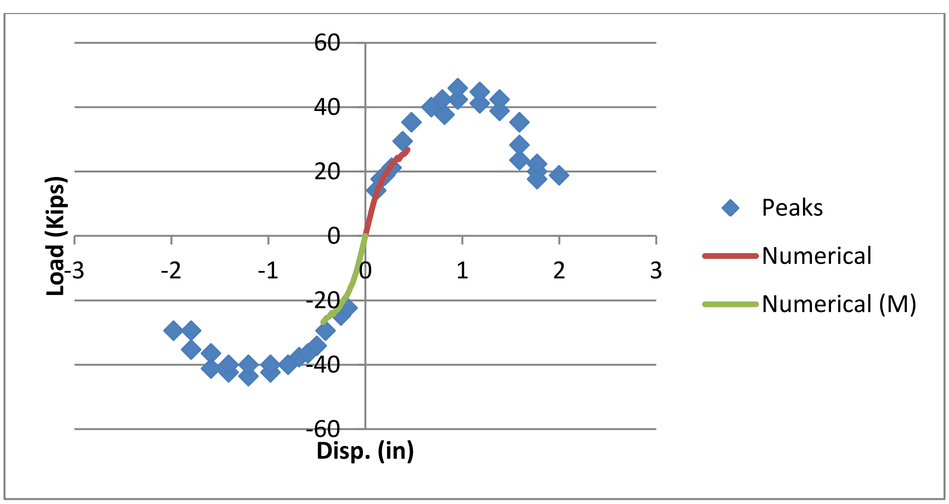

d) Comparison between FE and experimental results

Figure A1.17 Wall 6 (1/2 Spacing Mesh) Results

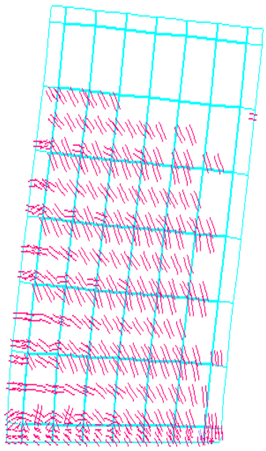

a) Deflected Shape and Crack Pattern

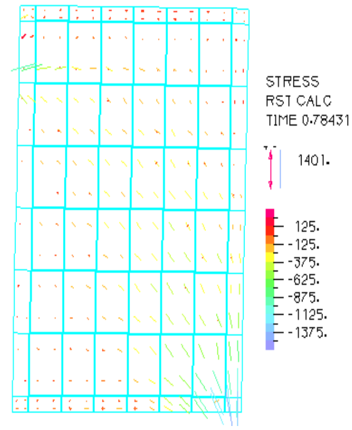

b) Masonry Principal Stresses

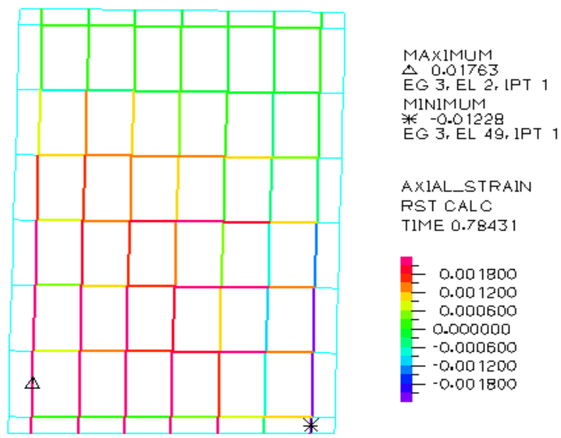

c) Axial Strain in Steel

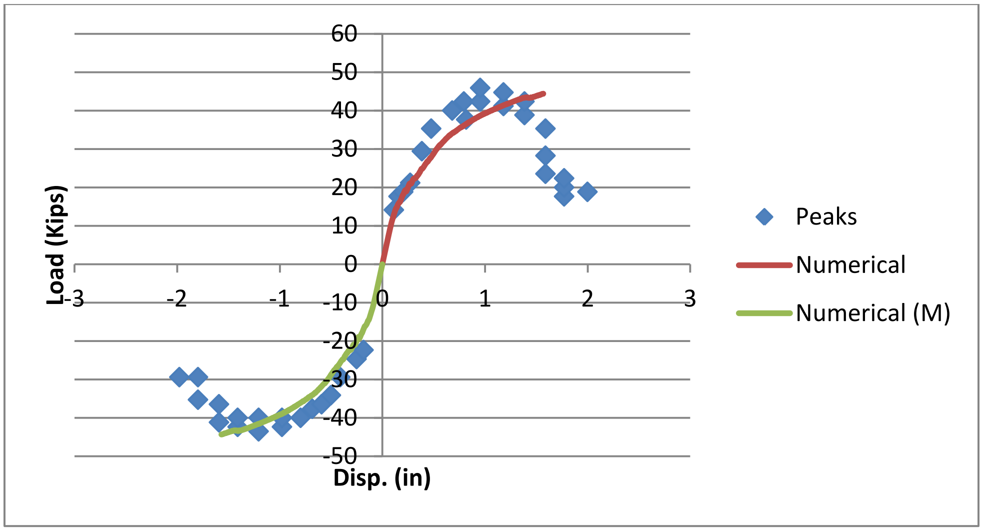

d) Comparison between FE and experimental results

Figure A1.18 Wall 6 (Spacing Mesh) Results

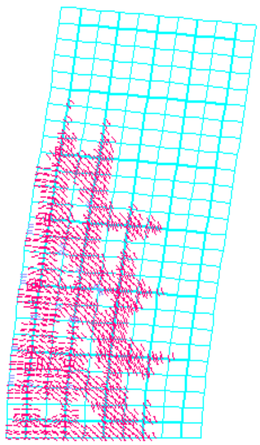

a) Deflected Shape and Crack Pattern

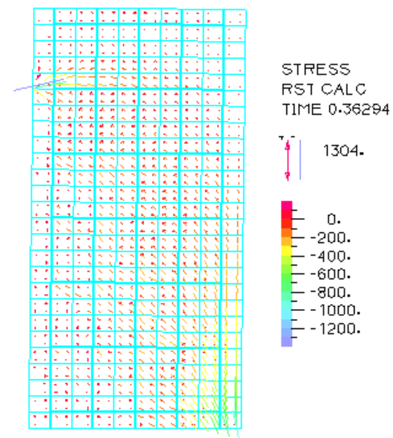

b) Masonry Principal Stresses

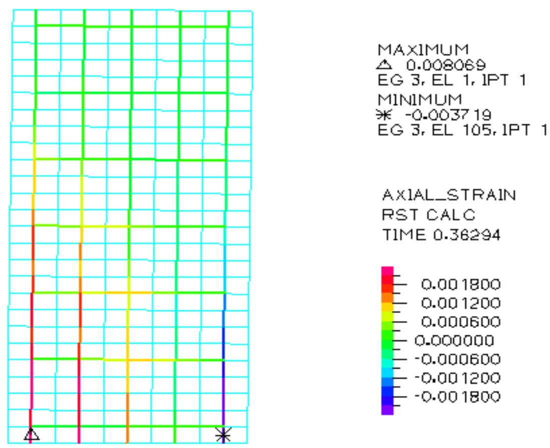

c) Axial Strains in Steel

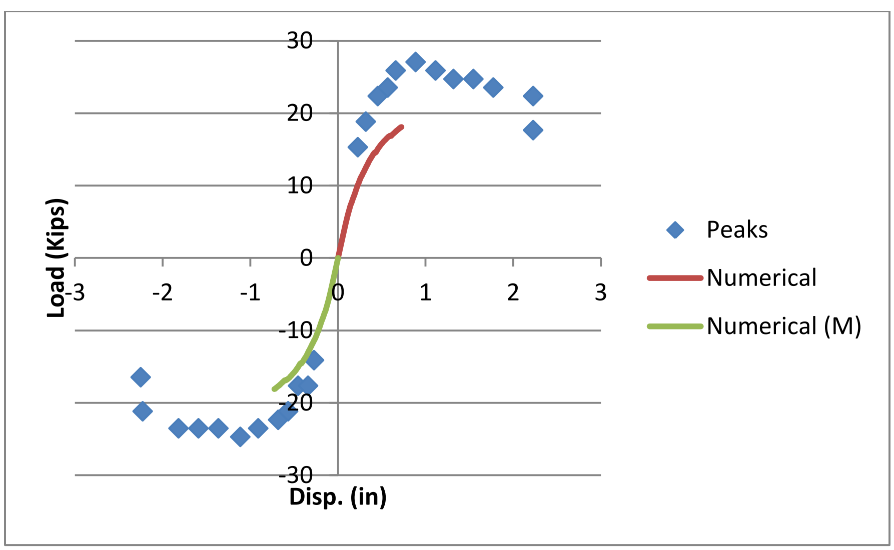

d) Comparison between FE and experimental results

Figure A1.19 Wall 7 (1/4 Spacing Mesh) Results

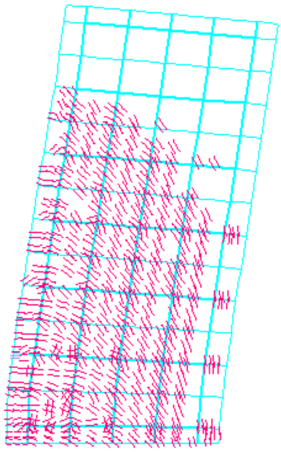

a) Deflected Shape and Crack Pattern

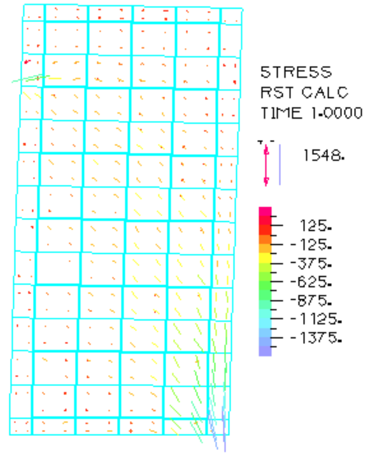

b) Masonry Principal Stresses

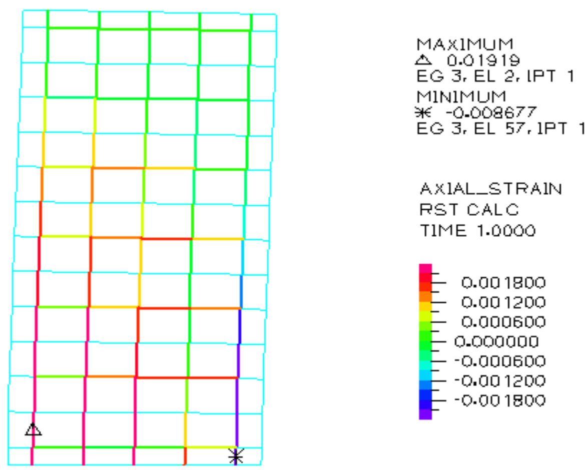

c) Axial Strains in Steel

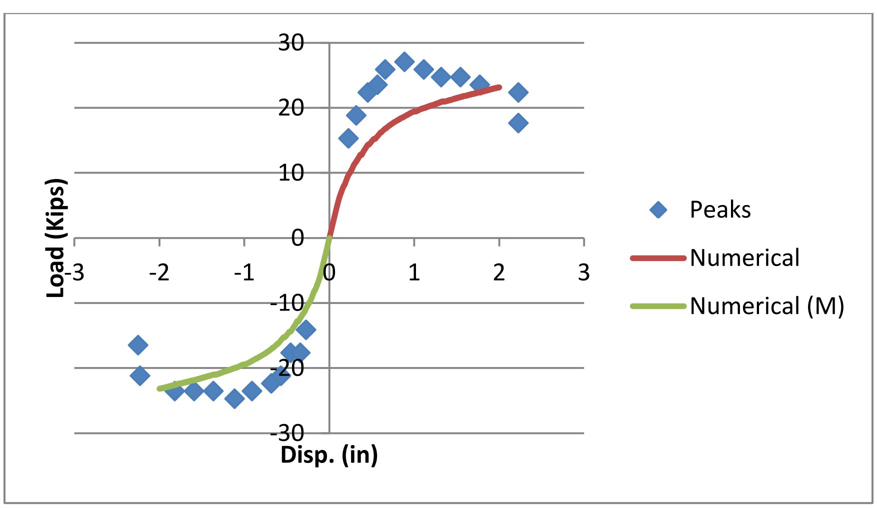

d) Comparison between FE and experimental results

Figure A1.20 Wall 7 (1/2 Spacing Mesh) Results

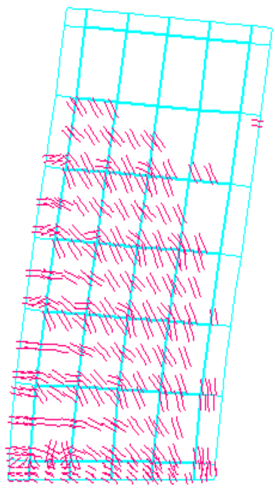

a) Deflected Shape and Crack Pattern

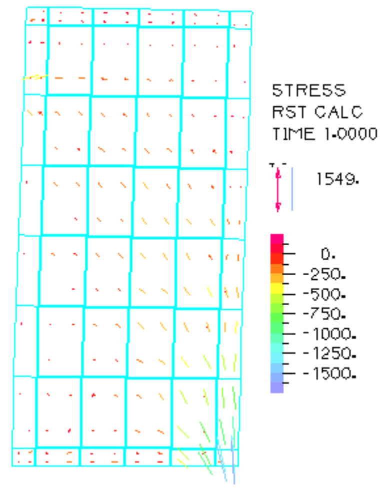

b) Masonry Principal Stresses

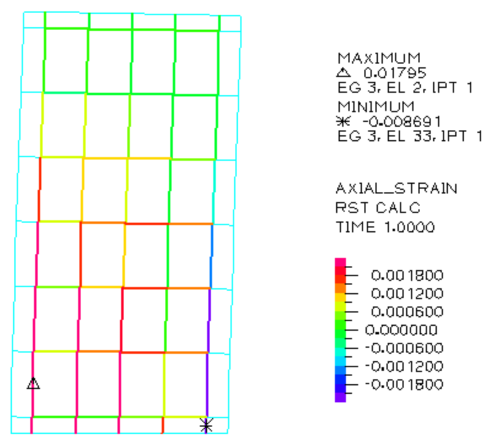

c) Axial Strains in Steel

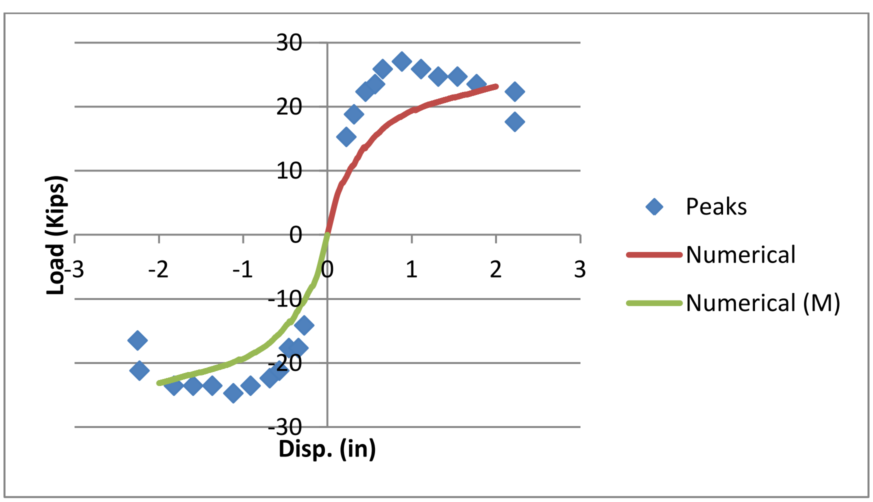

d) Comparison between FE and experimental results

Figure A1.21 Wall 7 (Spacing Mesh) Results

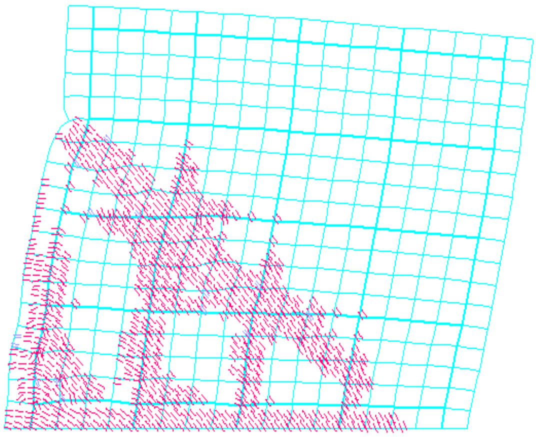

a) Deflected Shape and Crack Pattern

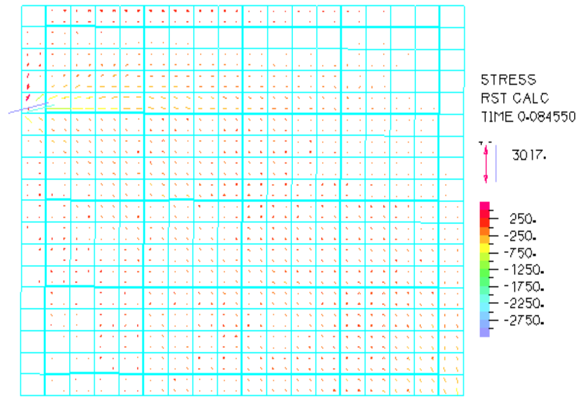

b) Masonry Principal Stresses

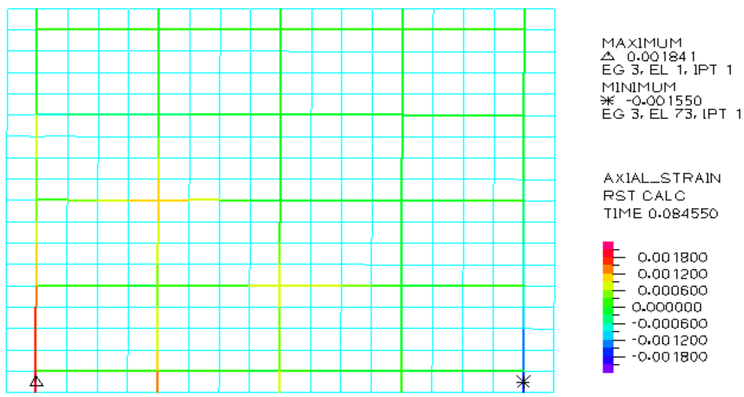

c) Axial Strains in Steel

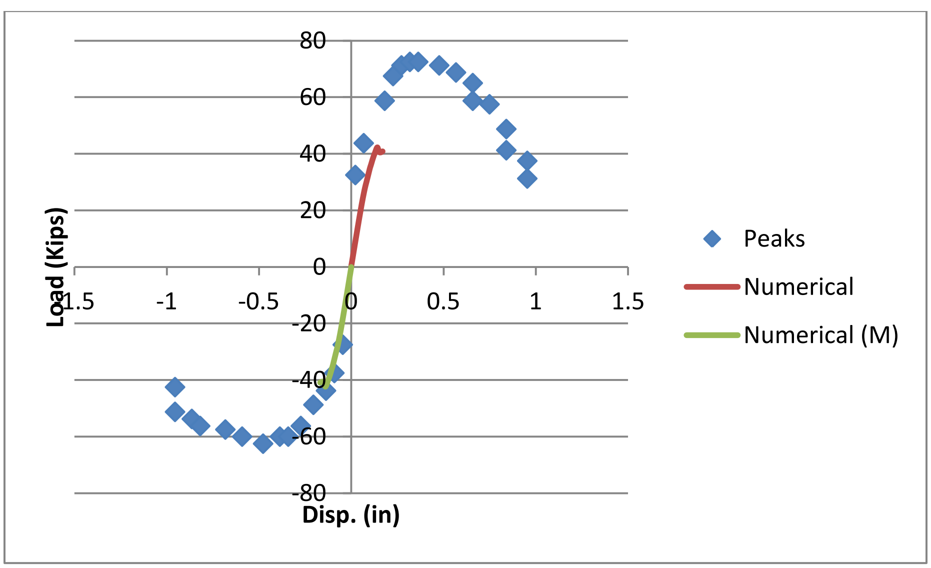

d) Comparison between FE and experimental results

Figure A1.22 Wall 8 (1/4 Spacing Mesh) Results

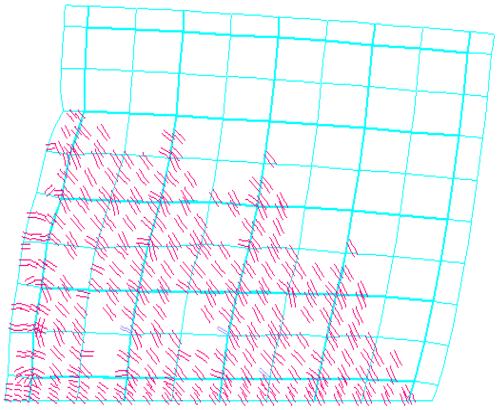

a) Deflected Shape and Crack Pattern

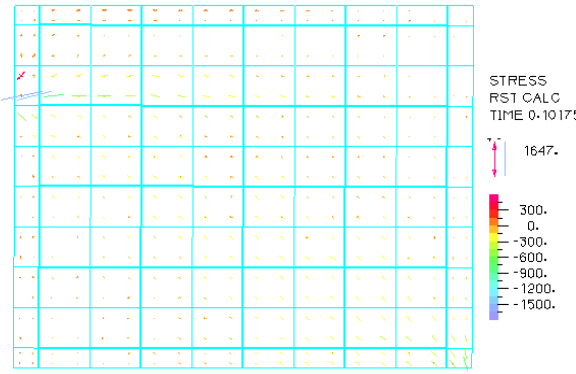

b) Masonry Principal Stresses

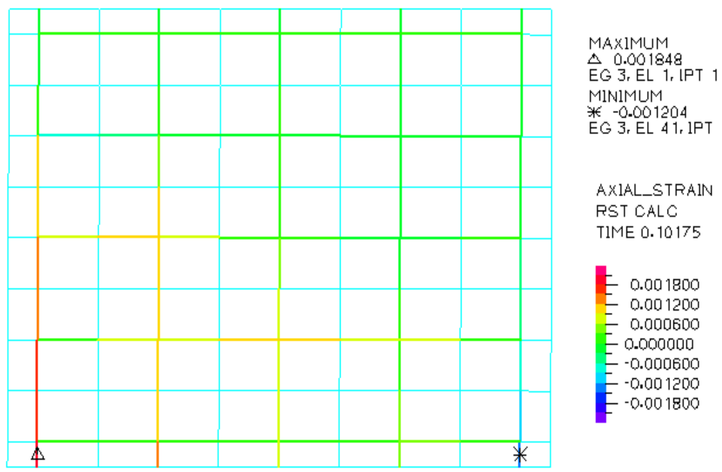

c) Axial Strains in Steel

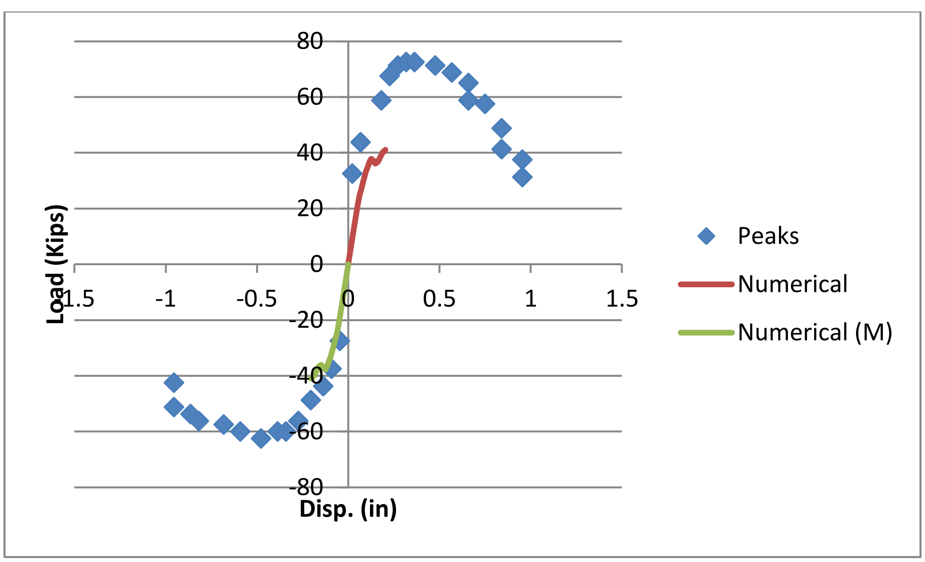

d) Comparison between FE and experimental results

Figure A1.23 Wall 8 (1/2 Spacing Mesh) Results

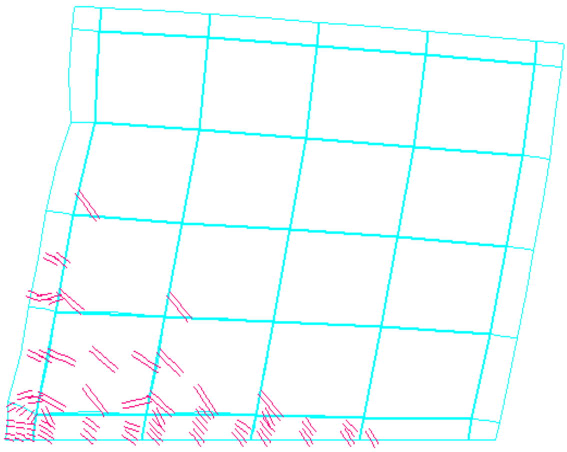

a) Deflected Shape and Crack Pattern

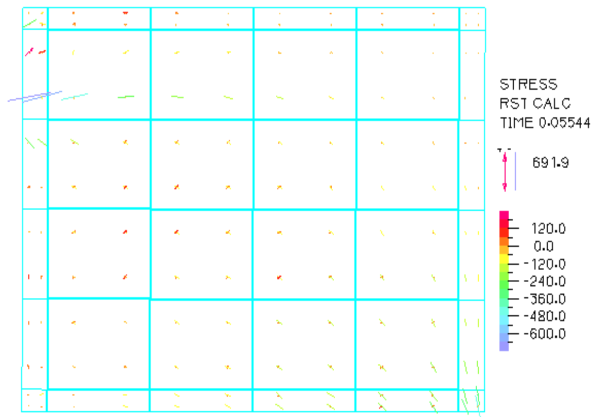

b) Masonry Principal Stresses

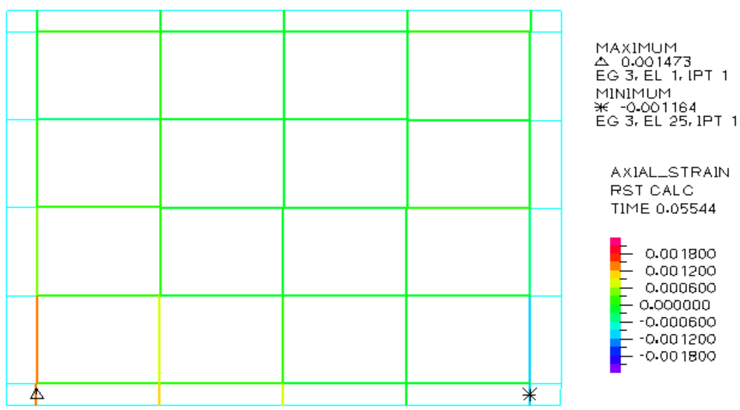

c) Axial Strains in Steel

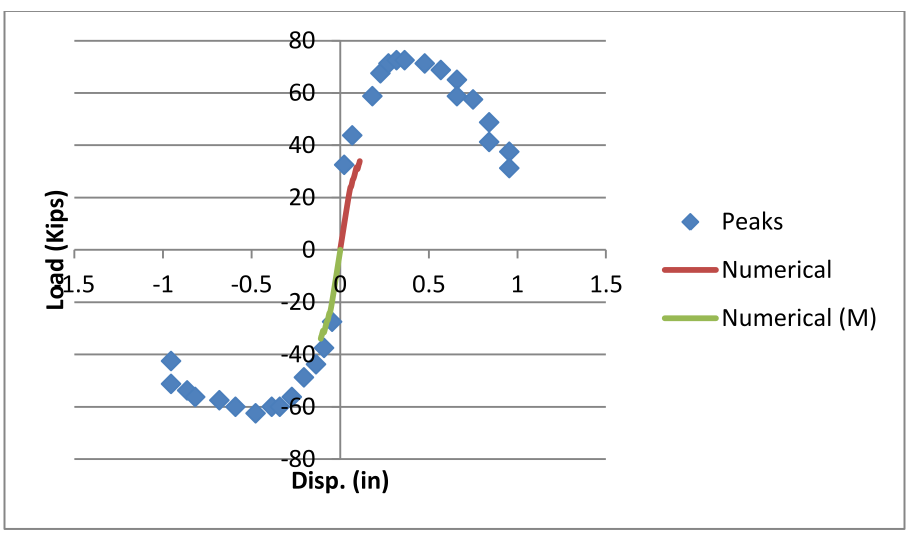

d) Comparison between FE and experimental results

Figure A1.24 Wall 8 (Spacing Mesh) Results

A.2 Smeared Model Results

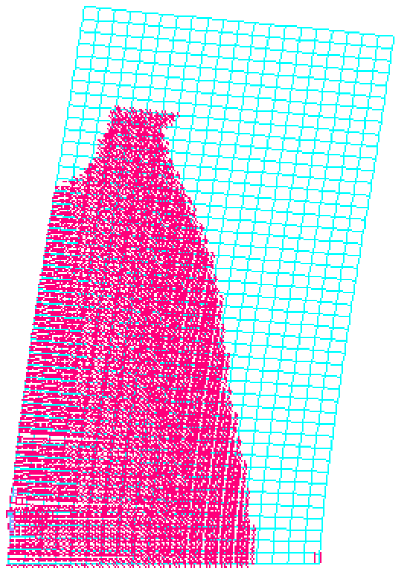

a) Deflected Shape and Crack Pattern

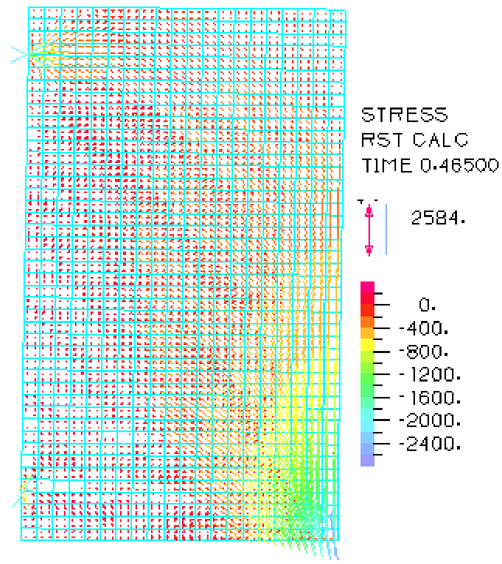

b) Masonry Principal Stresses

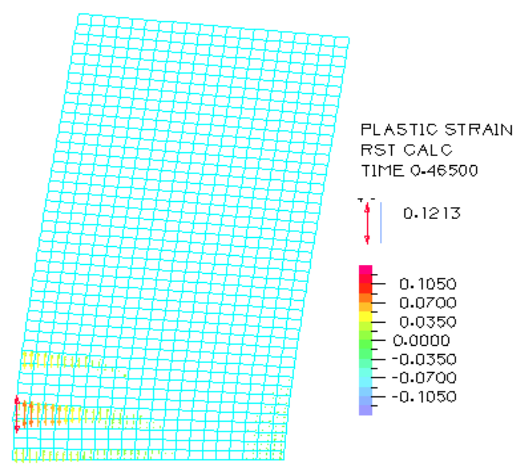

c) Steel Plastic Strain

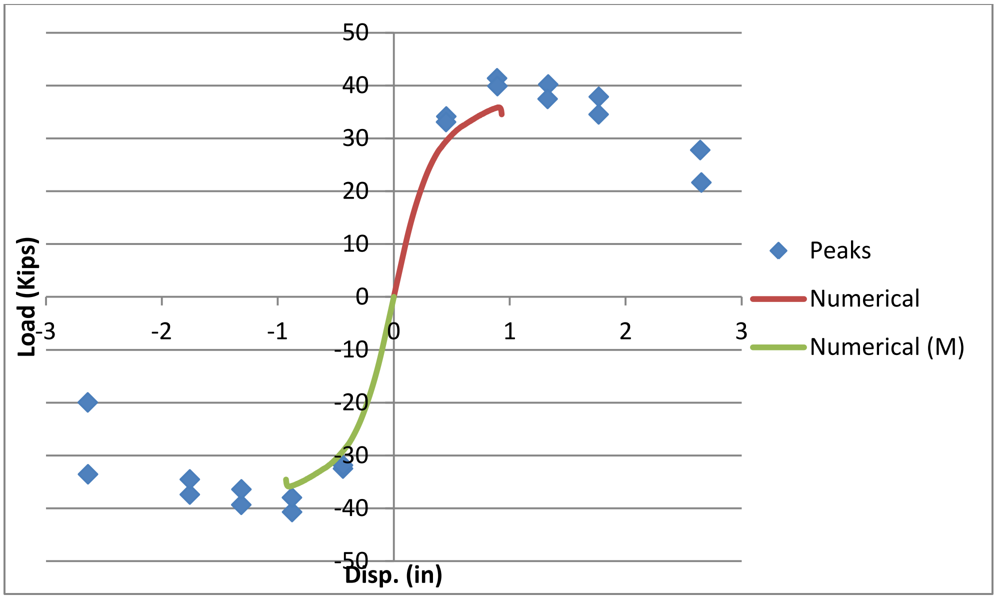

e) Comparison between FE and experimental results

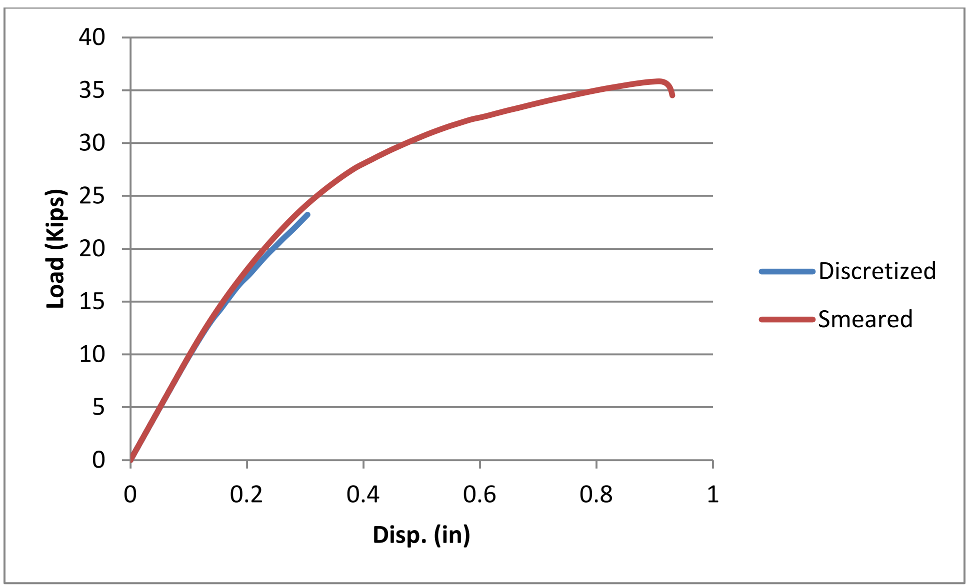

f) Comparison between FE Discretized and Smeared Models

Figure A2.1 Wall 1 (1/4 Spacing Mesh) Results

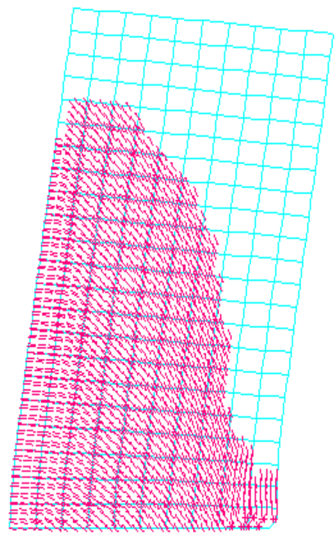

a) Deflected Shape and Crack Pattern

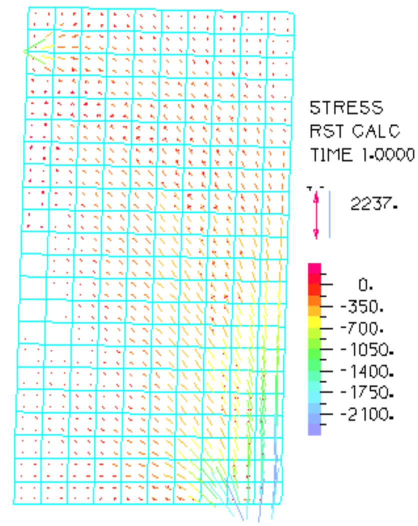

b) Masonry Principal Stresses

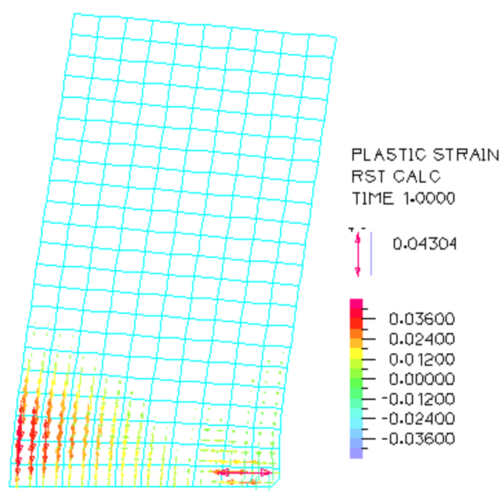

c) Steel Plastic Strain

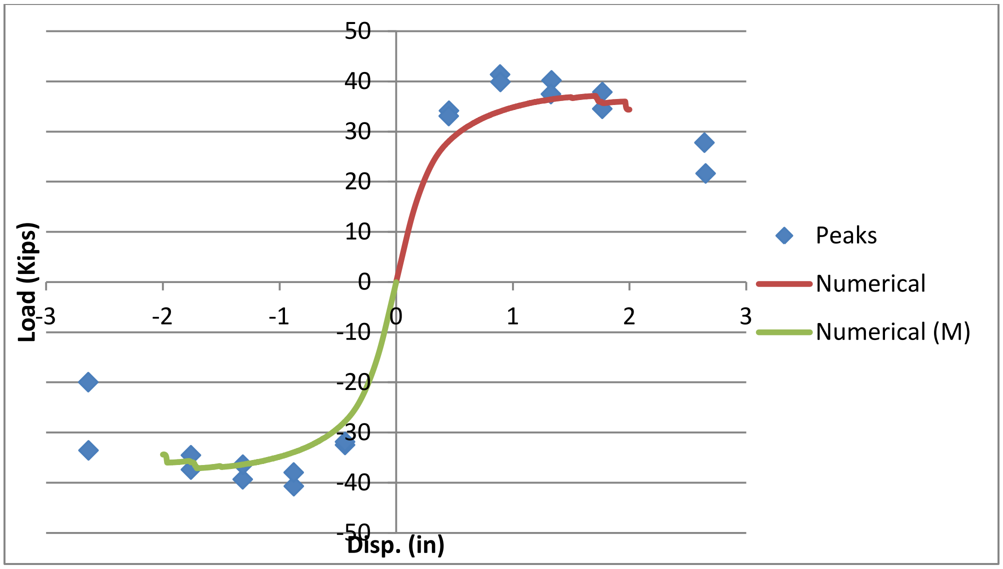

e) Comparison between FE and experimental results

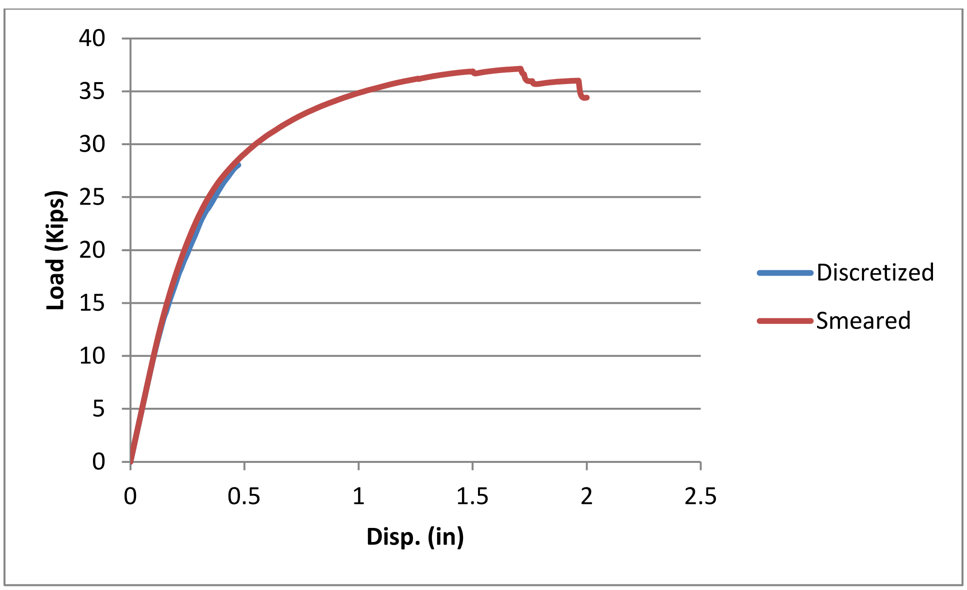

f) Comparison between FE Discretized and Smeared Models

Figure A2.2 Wall 1 (1/2 Spacing Mesh) Results

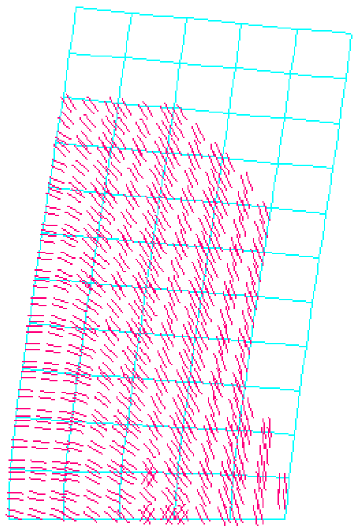

a) Deflected Shape and Crack Pattern

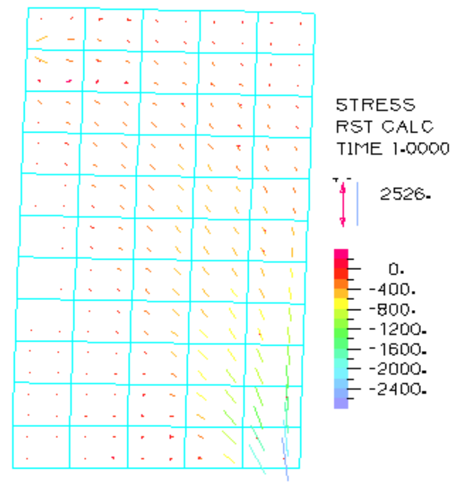

b) Masonry Principal Stresses

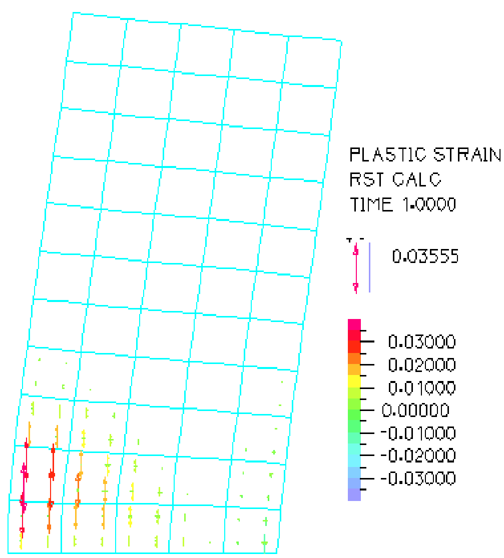

c) Steel Plastic Strain

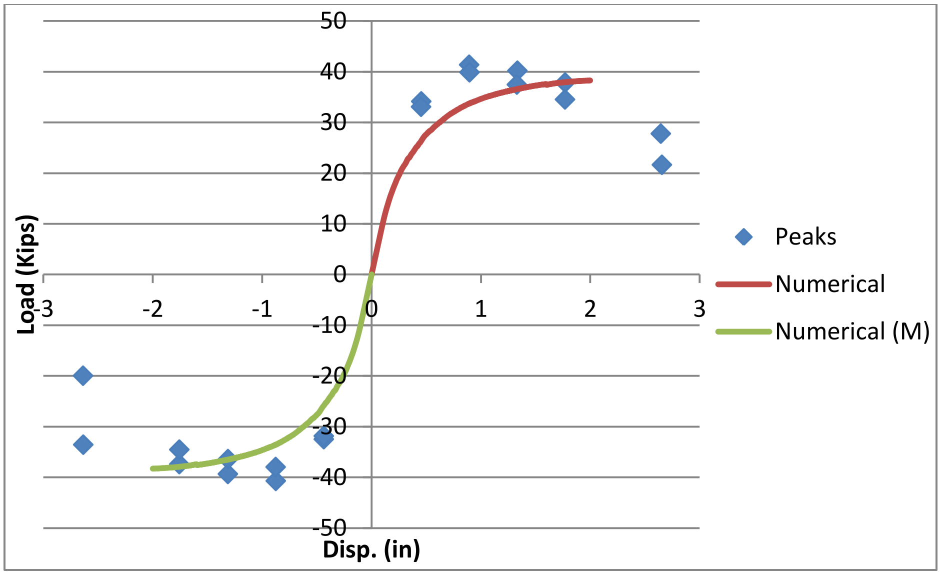

e) Comparison between FE and experimental results

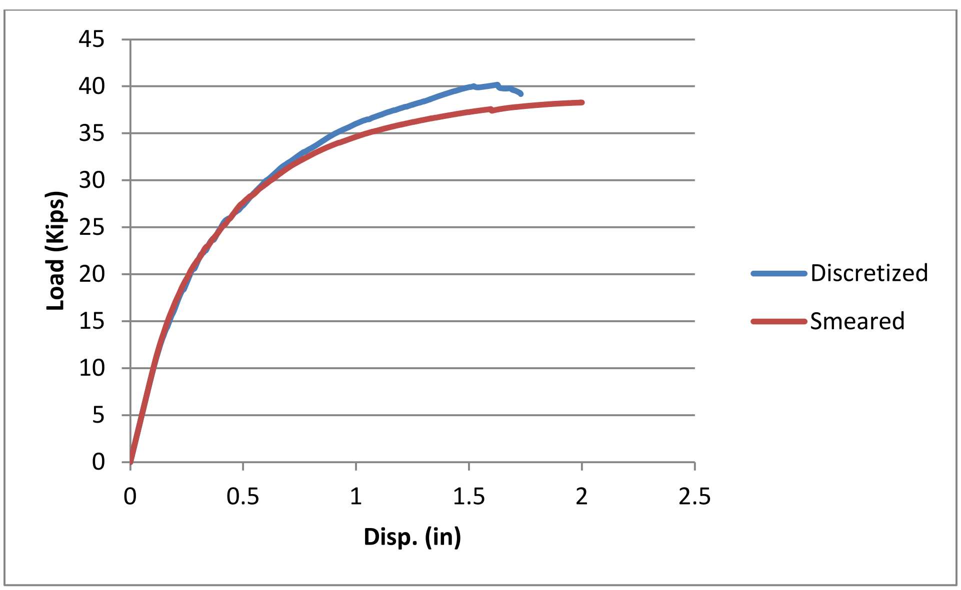

f) Comparison between FE Discretized and Smeared Models

Figure A2.3 Wall 1 (Spacing Mesh) Results

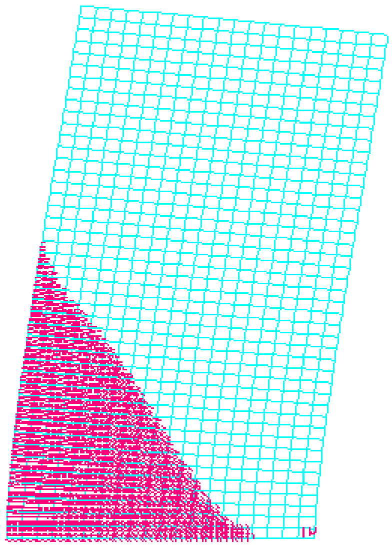

a) Deflected Shape and Crack Pattern

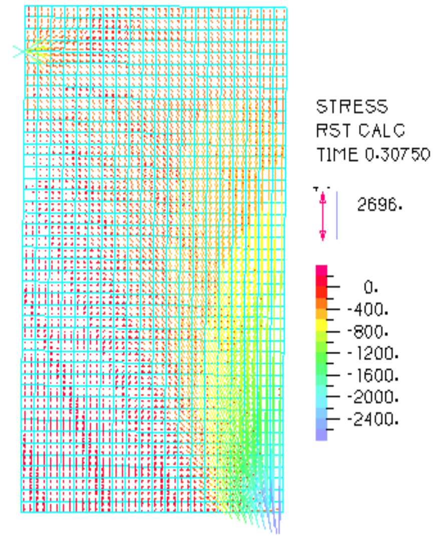

b) Masonry Principal Stresses

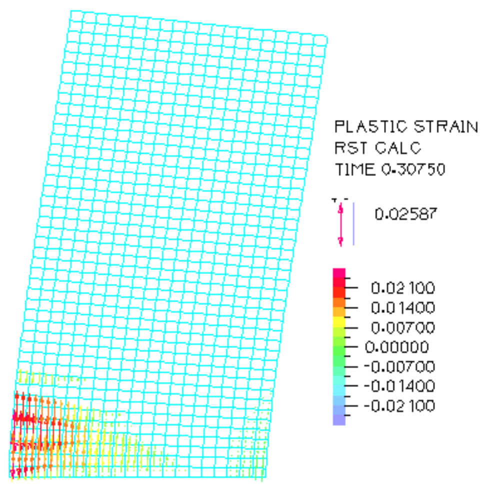

c) Steel Plastic Strain

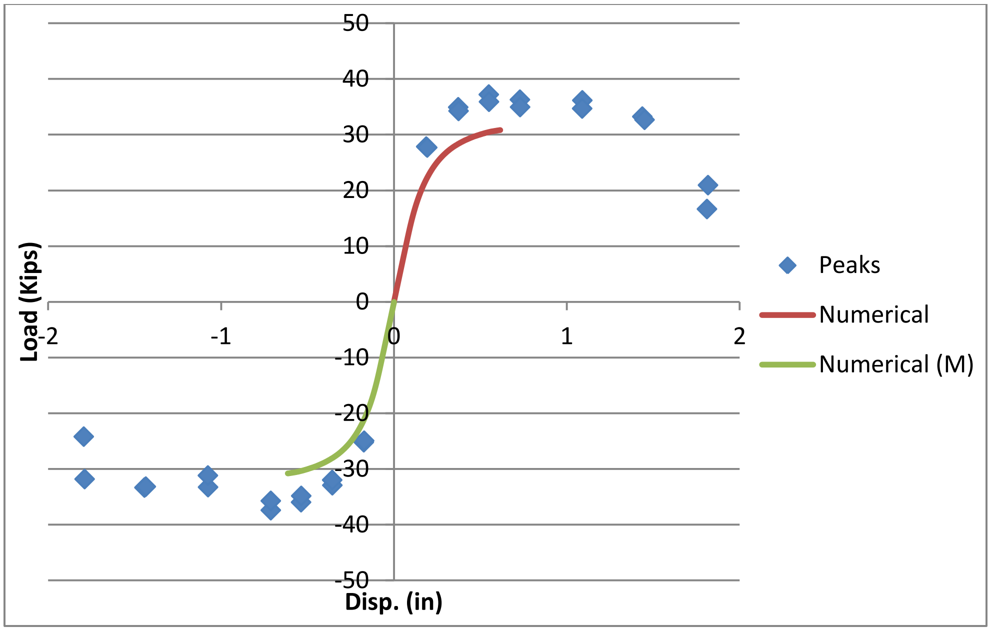

e) Comparison between FE and experimental results

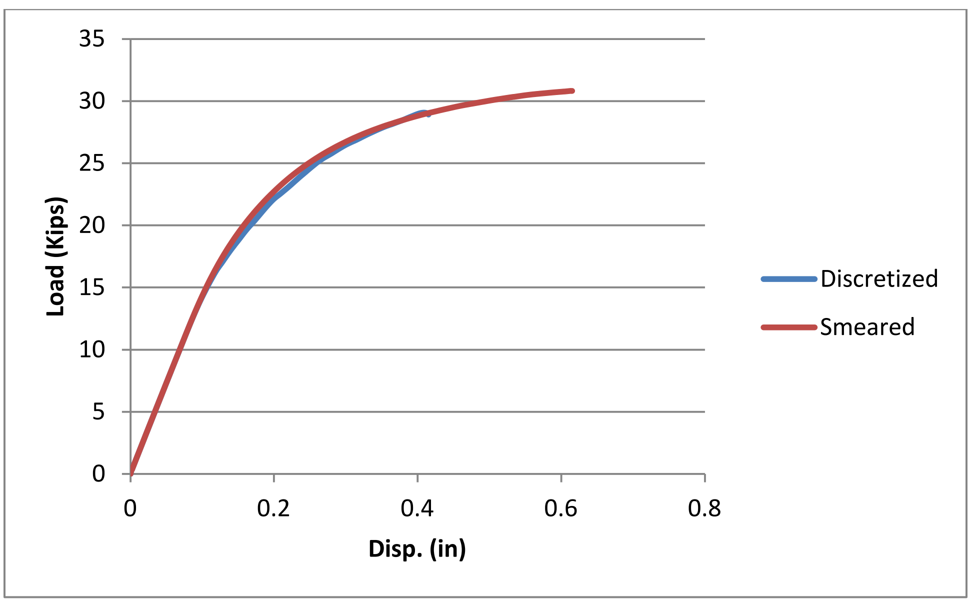

f) Comparison between FE Discretized and Smeared Models

Figure A2.4 Wall 2 (1/4 Spacing Mesh) Results

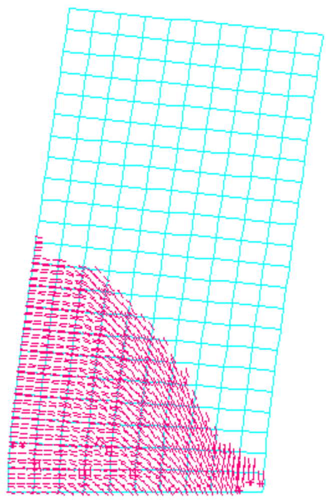

a) Deflected Shape and Crack Pattern

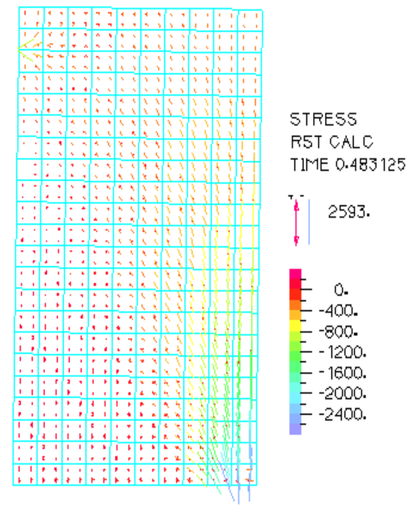

b) Masonry Principal Stresses

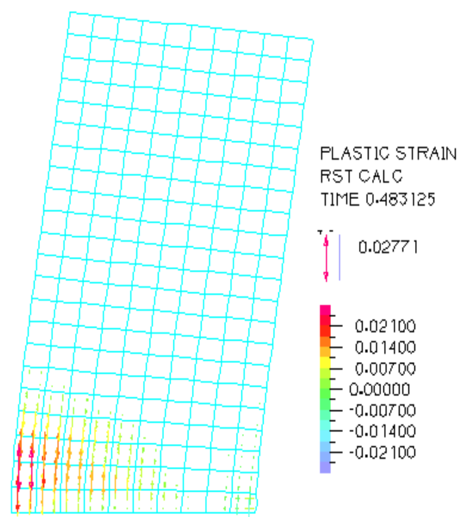

c) Steel Plastic Strain

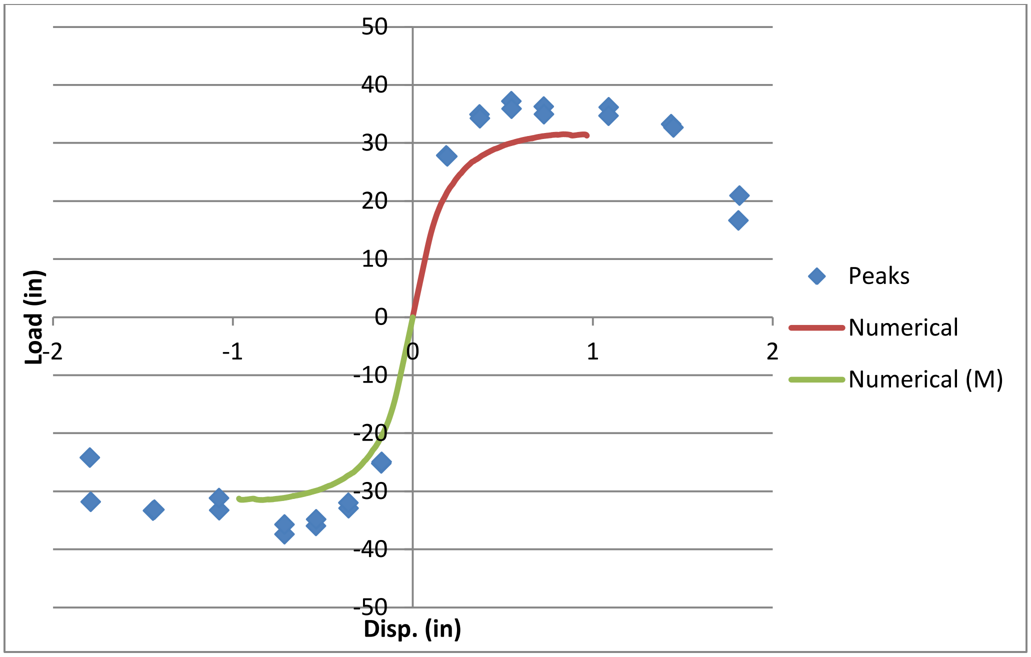

e) Comparison between FE and experimental results

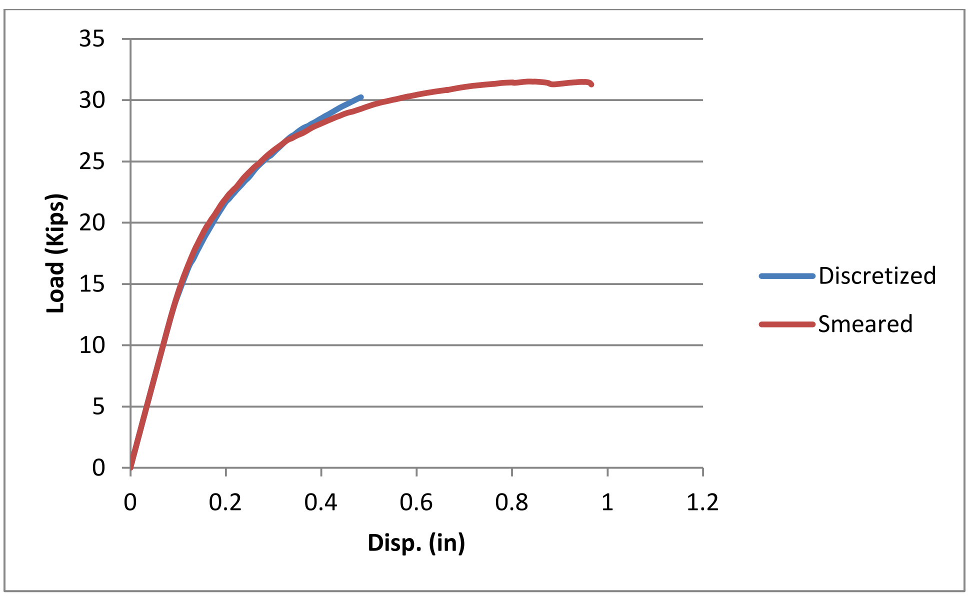

f) Comparison between FE Discretized and Smeared Models

Figure A2.5 Wall 2 (1/2 Spacing Mesh) Results

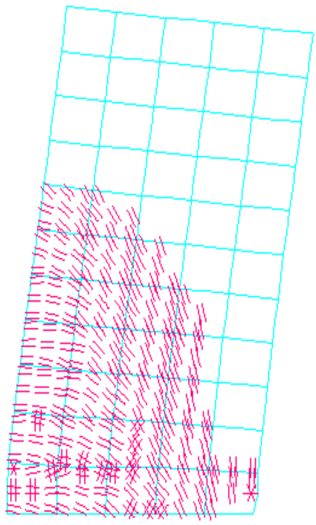

a) Deflected Shape and Crack Pattern

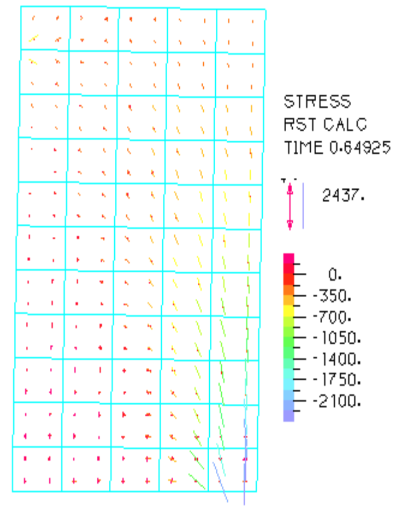

b) Masonry Principal Stresses

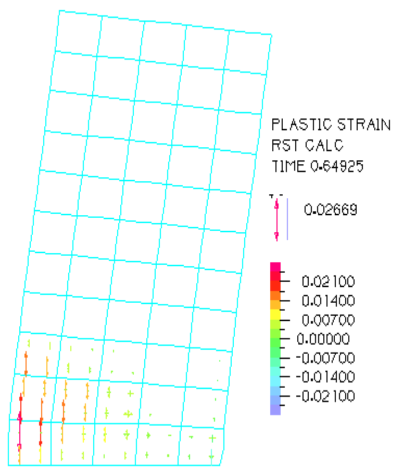

c) Steel Plastic Strain

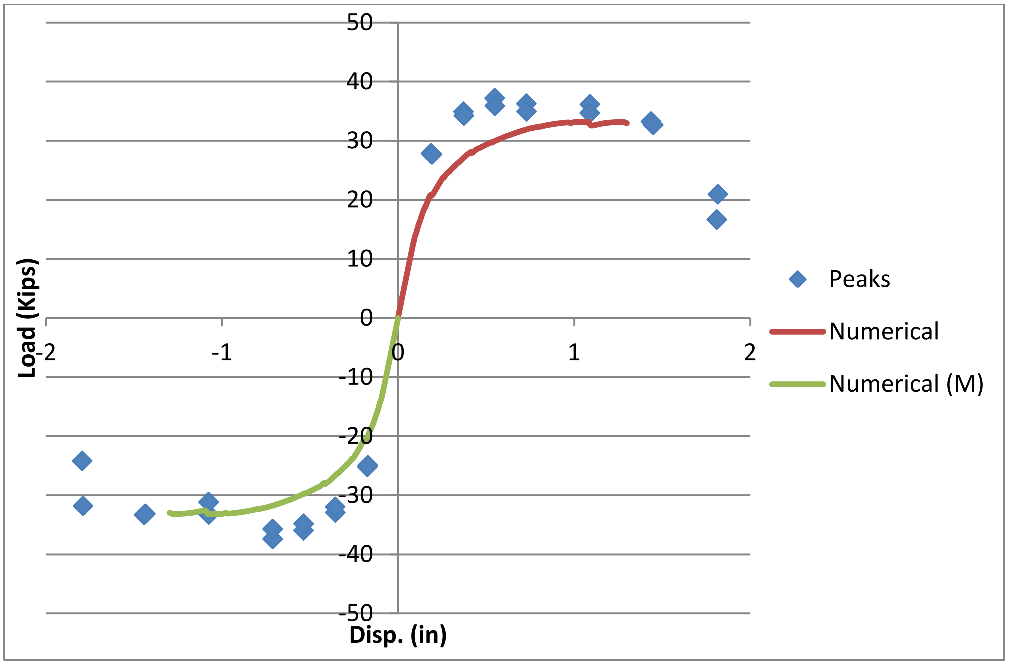

e) Comparison between FE and experimental results

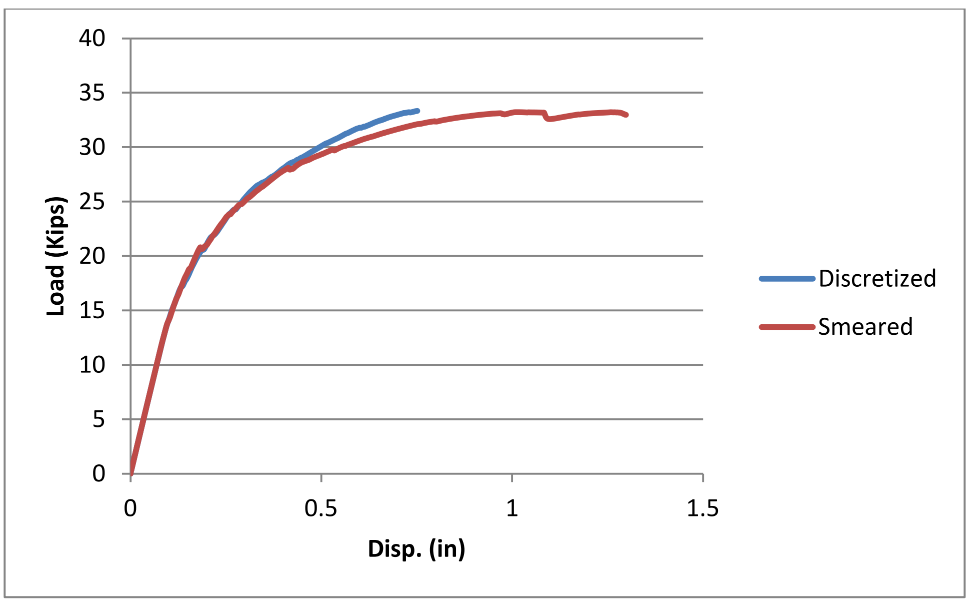

f) Comparison between FE Discretized and Smeared Models

Figure A2.6 Wall 2 (Spacing Mesh) Results

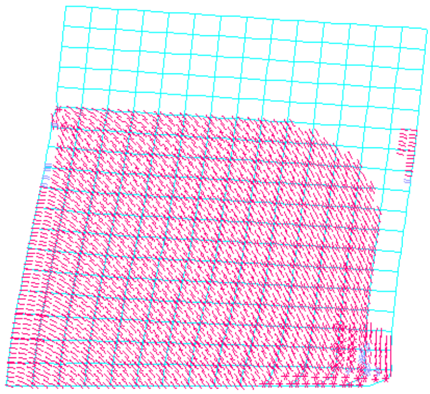

a) Deflected Shape and Crack Pattern

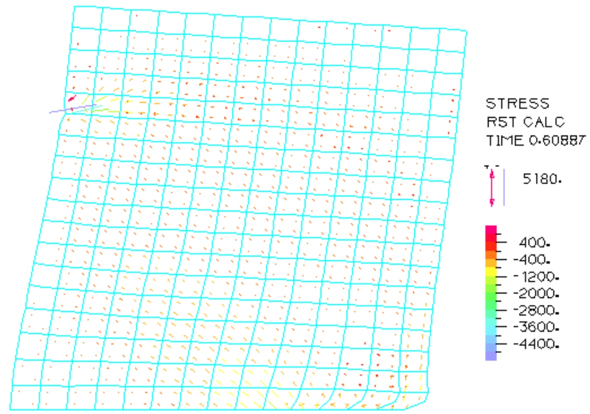

b) Masonry Principal Stresses

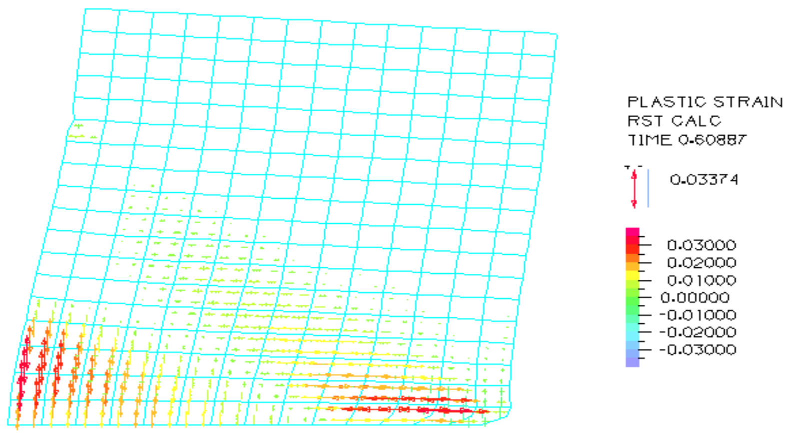

c) Steel Plastic Strain

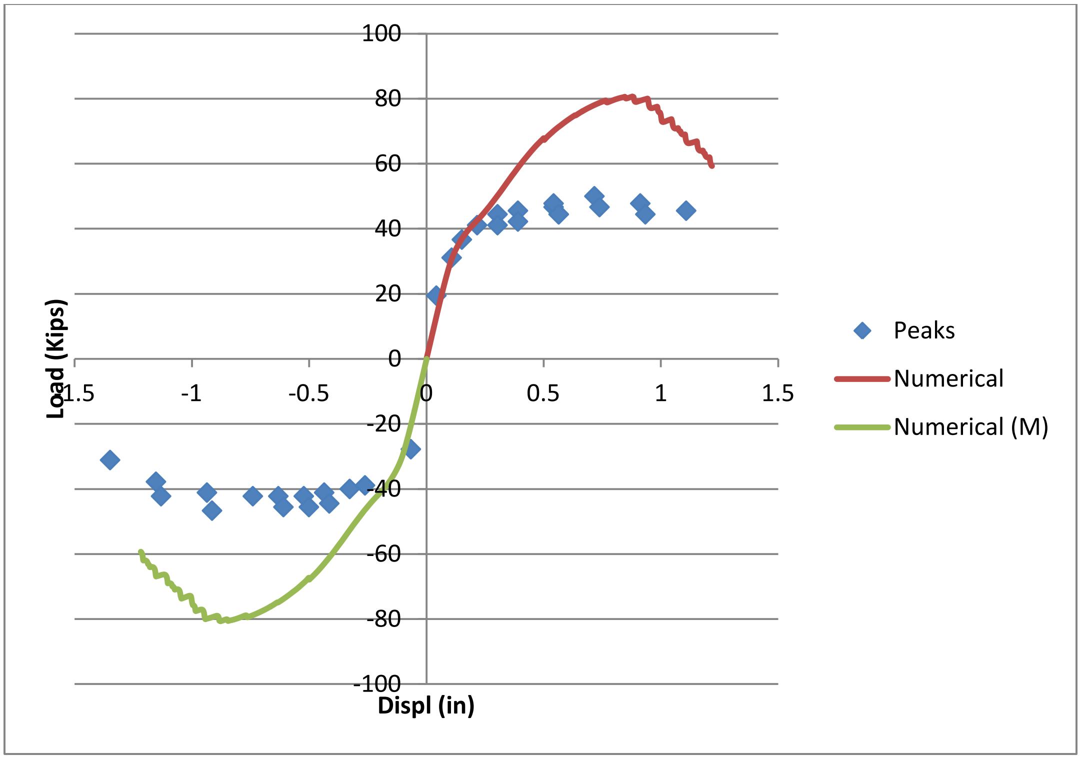

e) Comparison between FE and experimental results

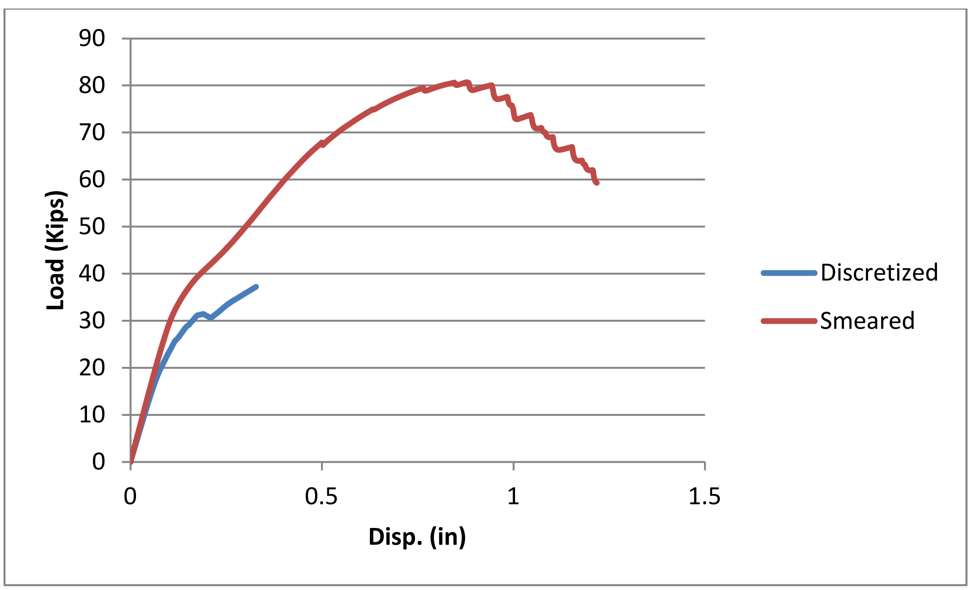

f) Comparison between FE Discretized and Smeared Models

Figure A2.7 Wall 3 (1/4 Spacing Mesh) Results

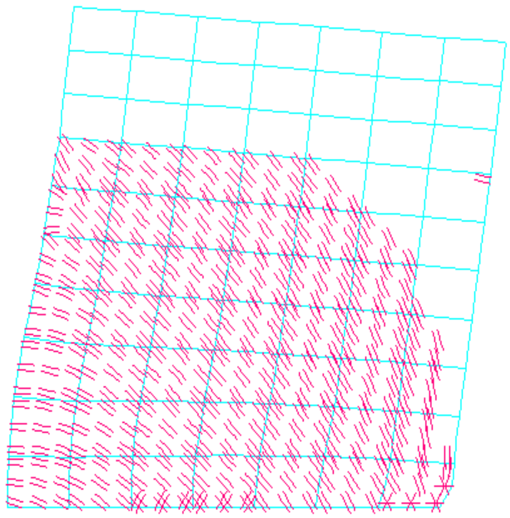

a) Deflected Shape and Crack Pattern

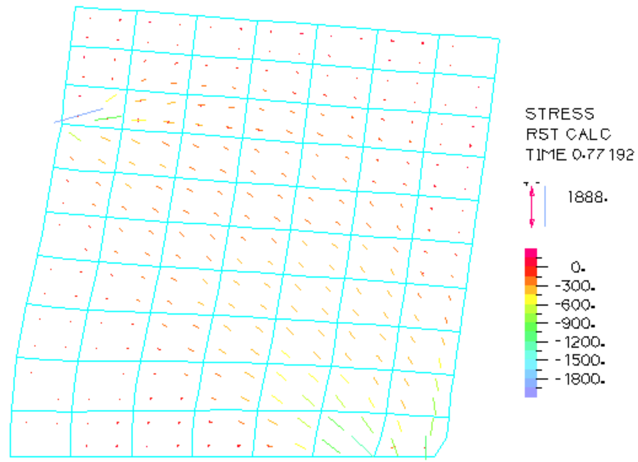

b) Masonry Principal Stresses

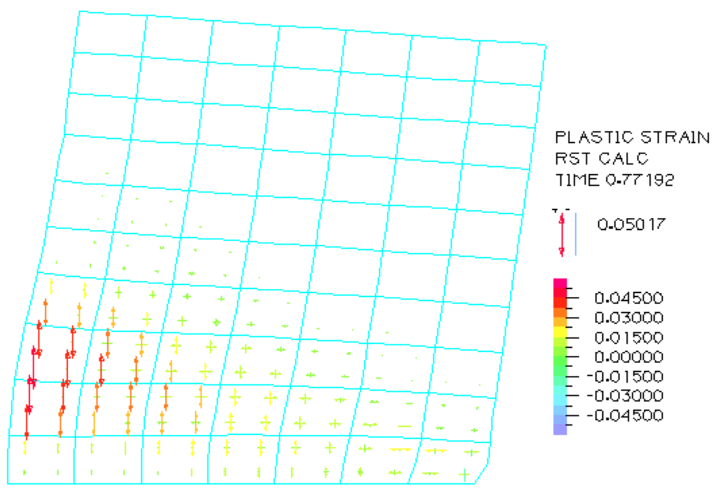

c) Steel Plastic Strain

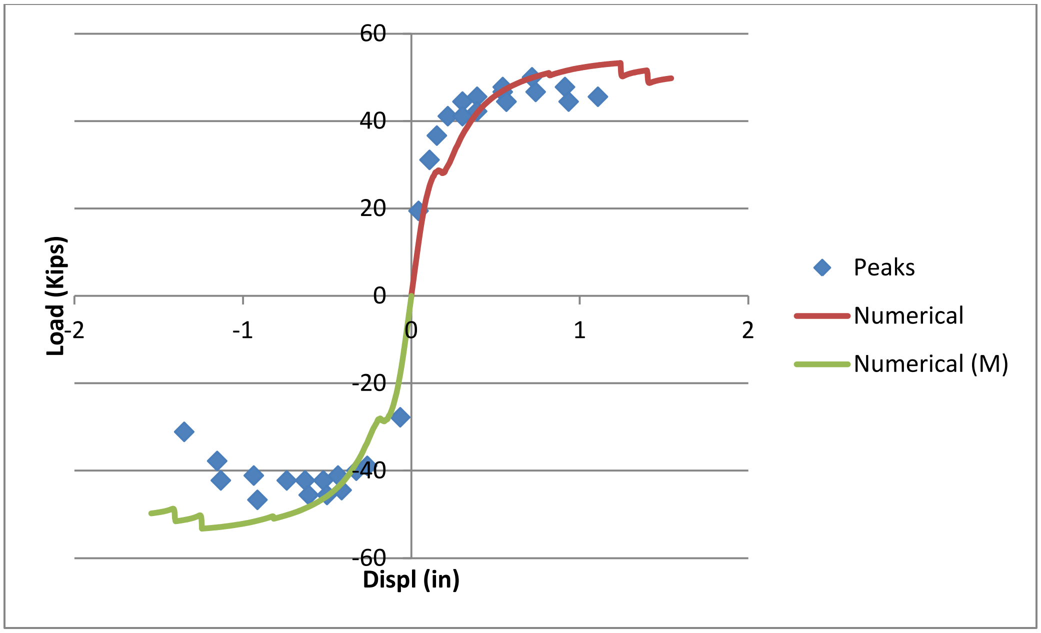

e) Comparison between FE and experimental results

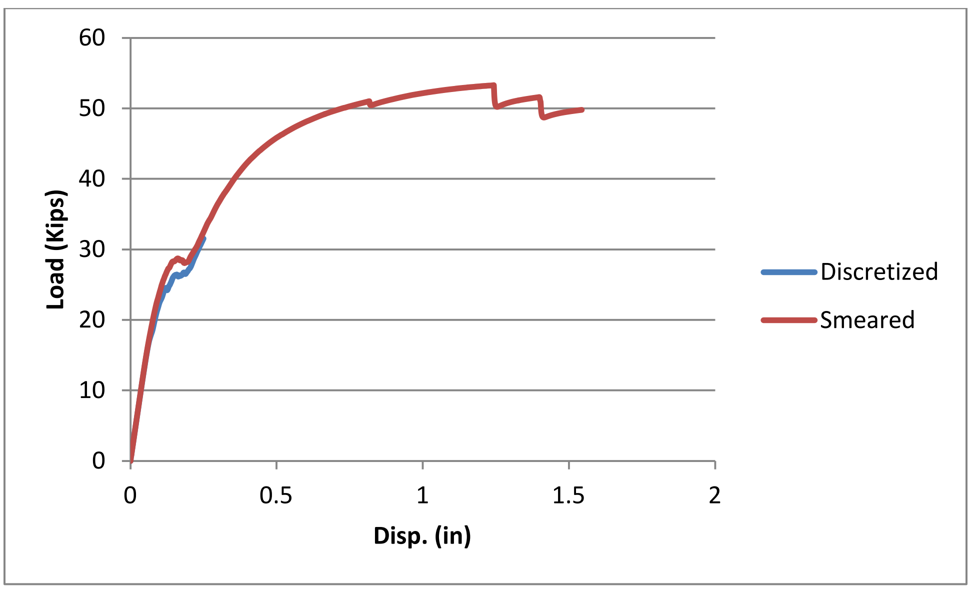

f) Comparison between FE Discretized and Smeared Models

Figure A2.8 Wall 3 (1/2 Spacing Mesh) Results

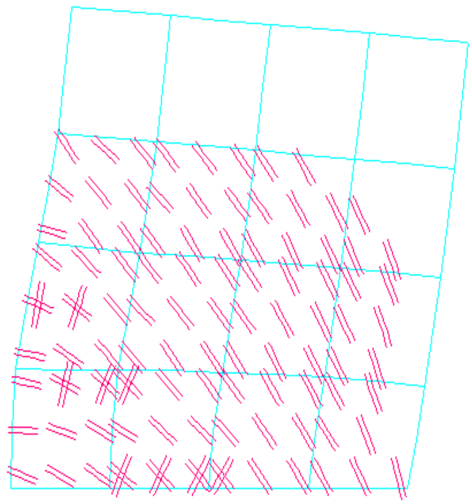

a) Deflected Shape and Crack Pattern

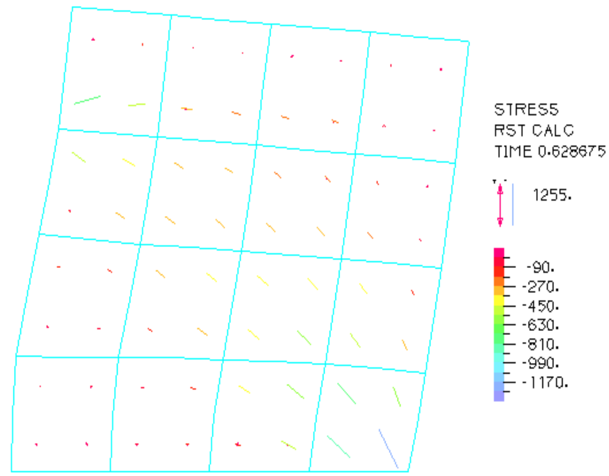

b) Masonry Principal Stresses

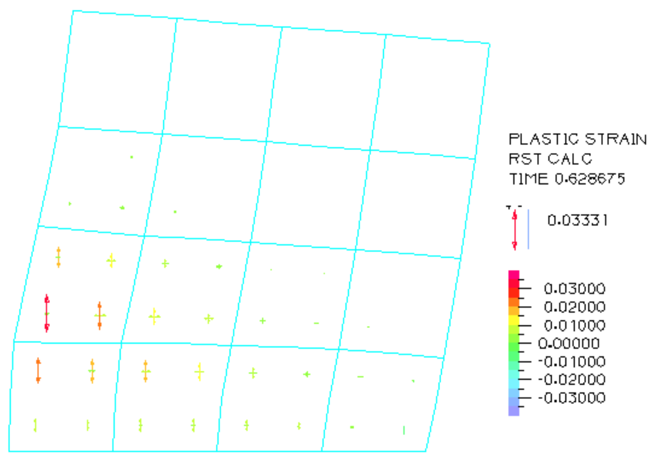

c) Steel Plastic Strain

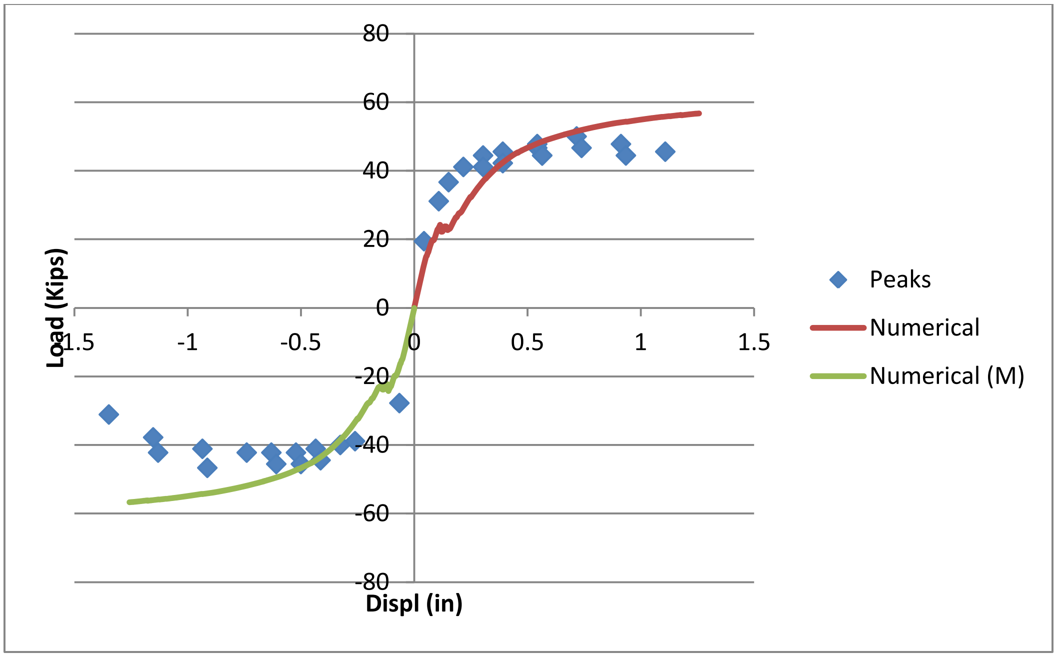

e) Comparison between FE and experimental results

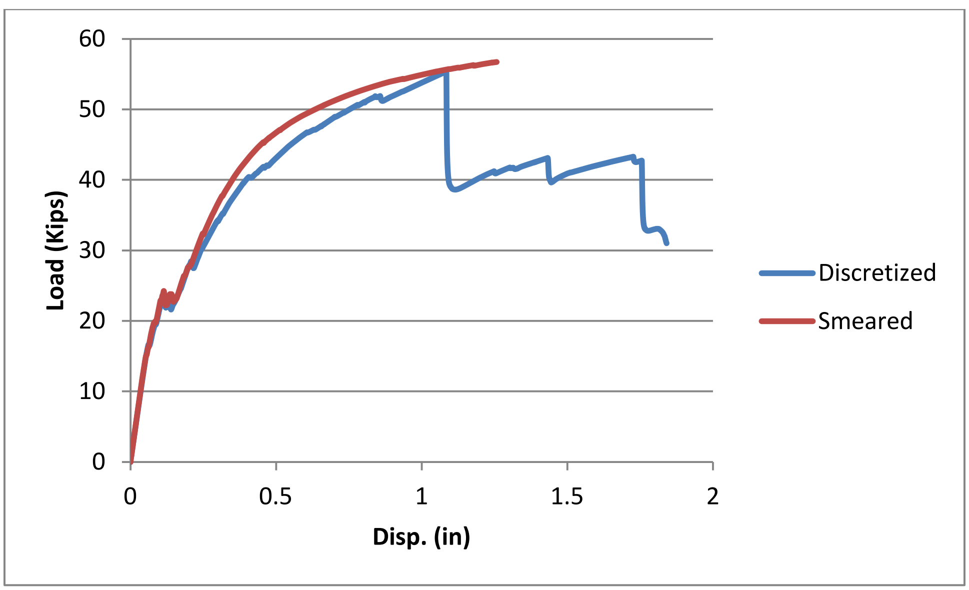

f) Comparison between FE Discretized and Smeared Models

Figure A2.9 Wall 3 (Spacing Mesh) Results

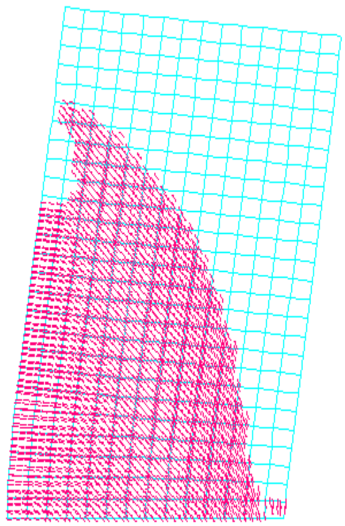

a) Deflected Shape and Crack Pattern

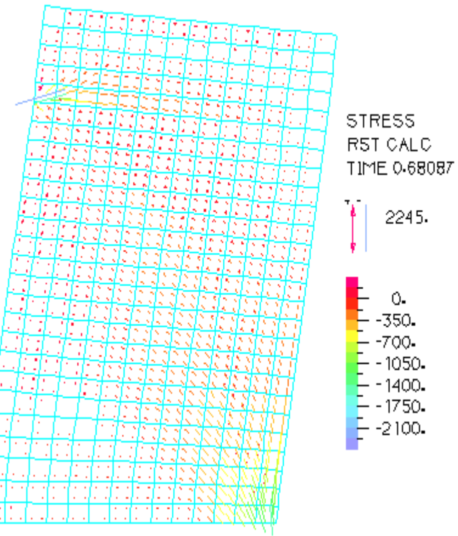

b) Masonry Principal Stresses

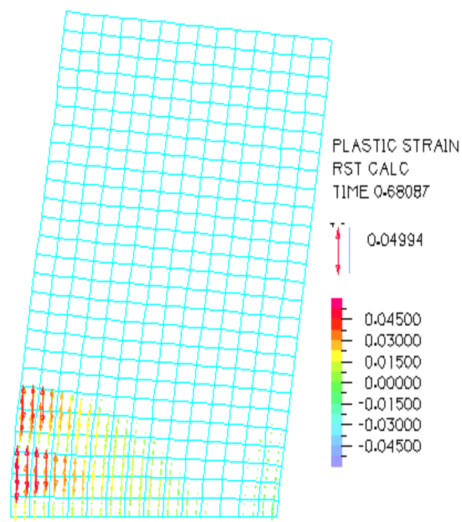

c) Steel Plastic Strain

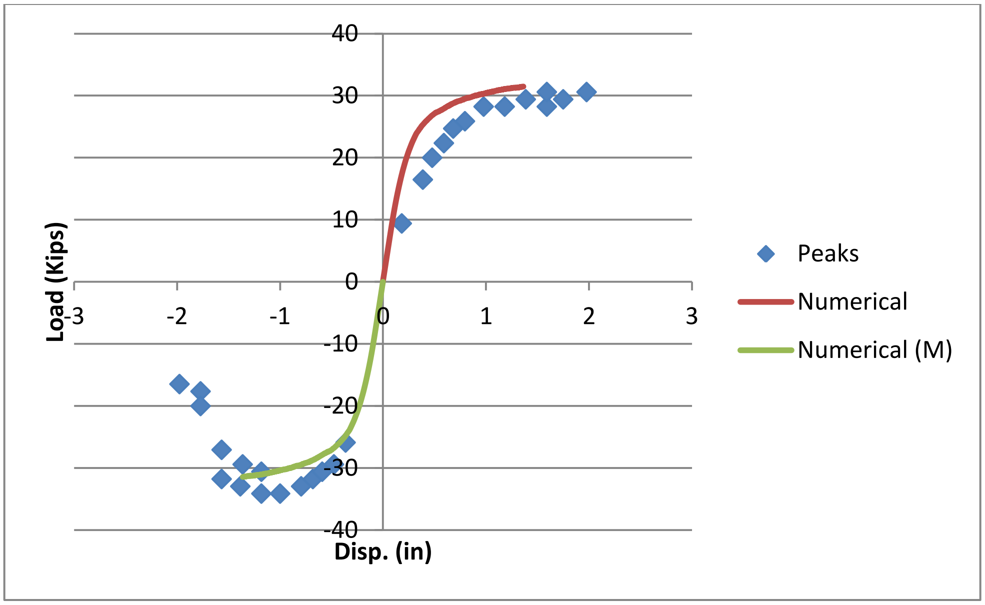

e) Comparison between FE and experimental results

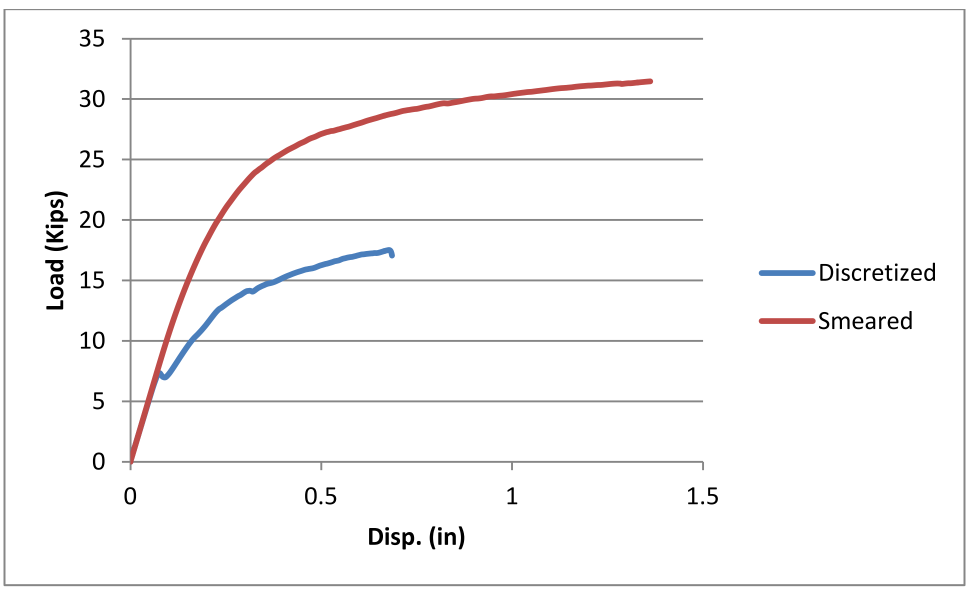

f) Comparison between FE Discretized and Smeared Models

Figure A2.10 Wall 4 (1/4 Spacing Mesh) Results

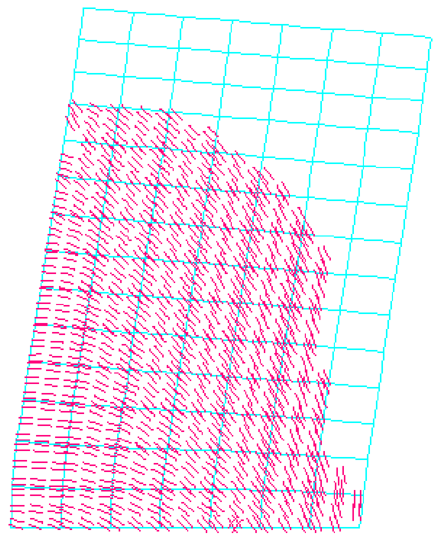

a) Deflected Shape and Crack Pattern

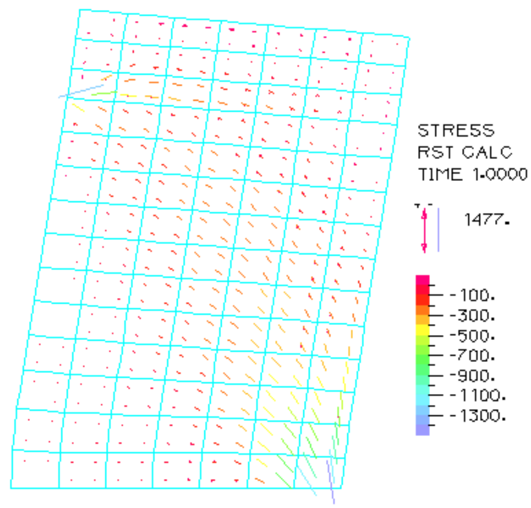

b) Masonry Principal Stresses

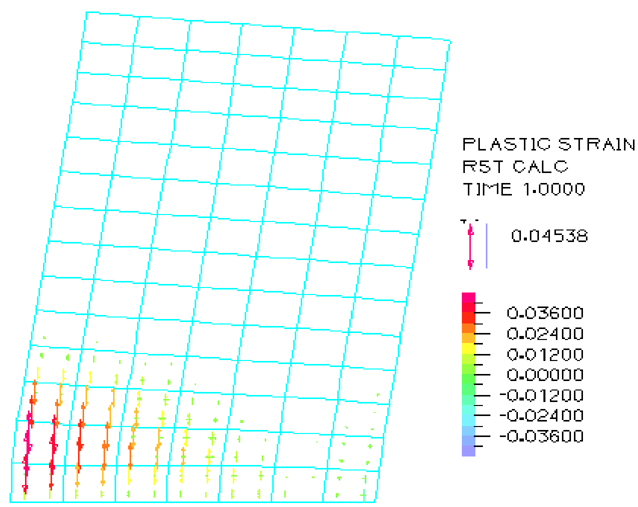

c) Steel Plastic Strain

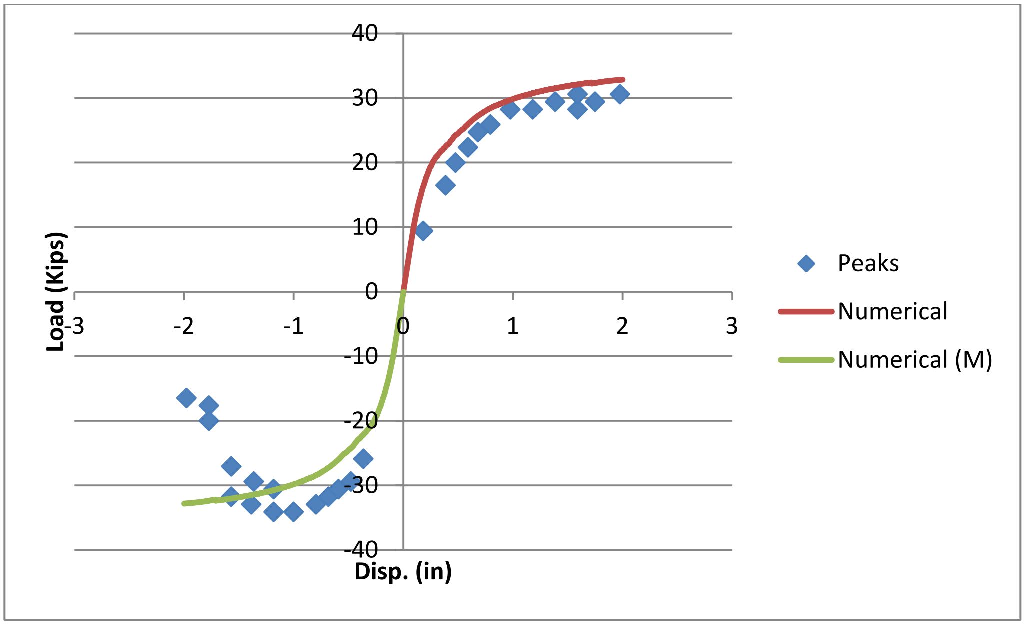

e) Comparison between FE and experimental results

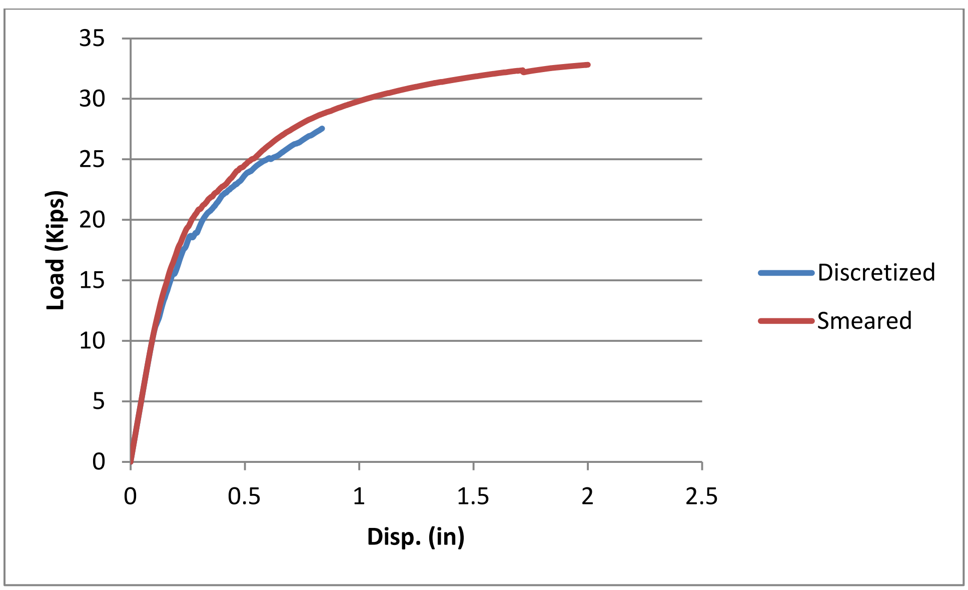

f) Comparison between FE Discretized and Smeared Models

Figure A2.11 Wall 4 (1/2 Spacing Mesh) Results

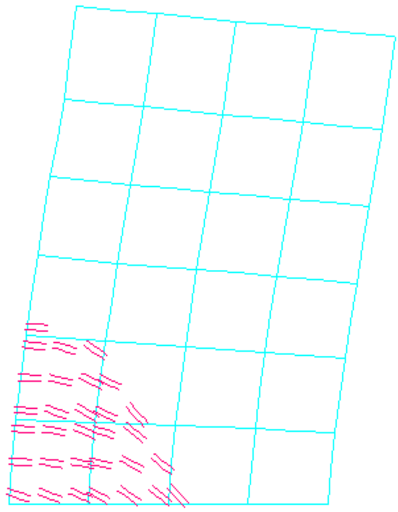

a) Deflected Shape and Crack Pattern

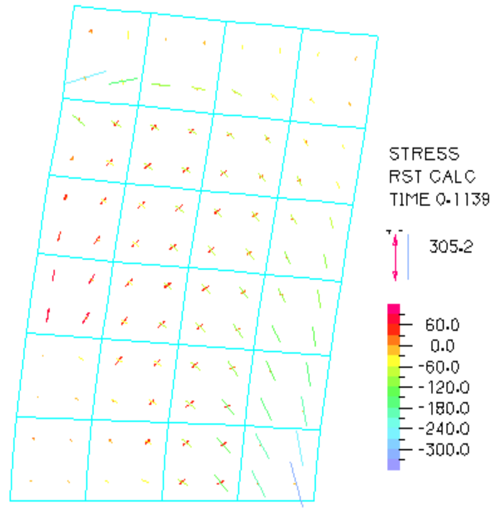

b) Masonry Principal Stresses

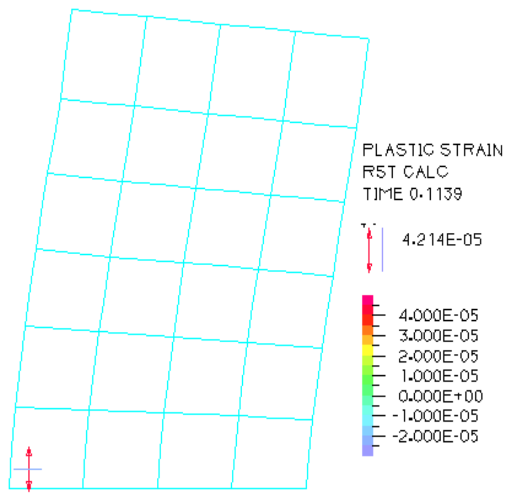

c) Steel Plastic Strain

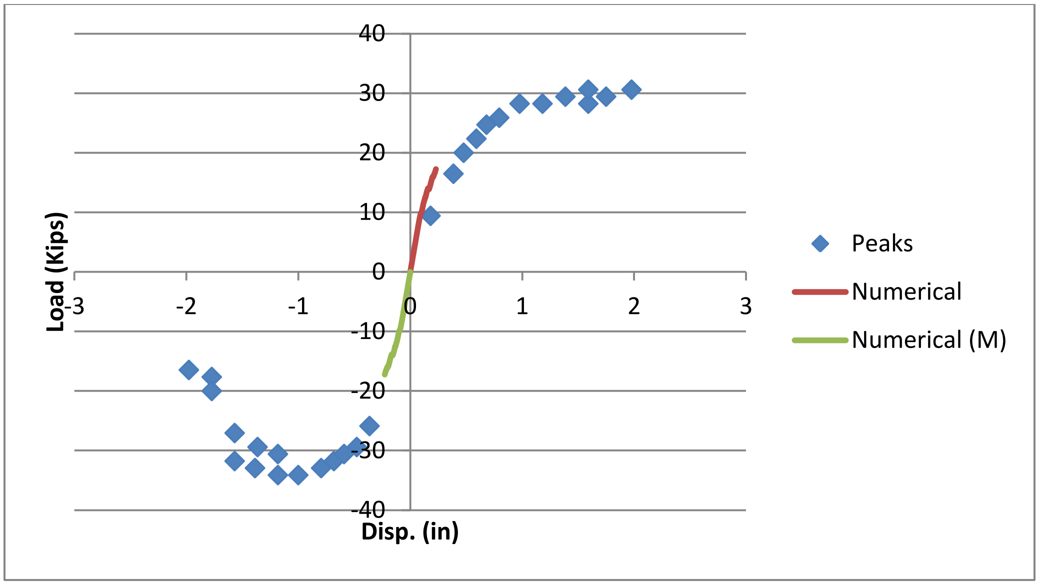

e) Comparison between FE and experimental results

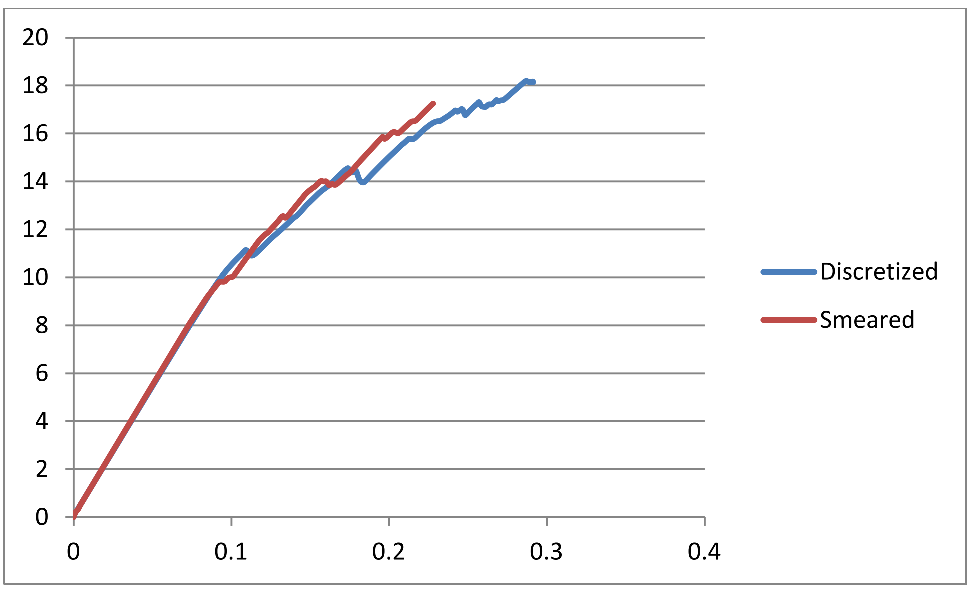

f) Comparison between FE Discretized and Smeared Models

Figure A2.12 Wall 4 (Spacing Mesh) Results

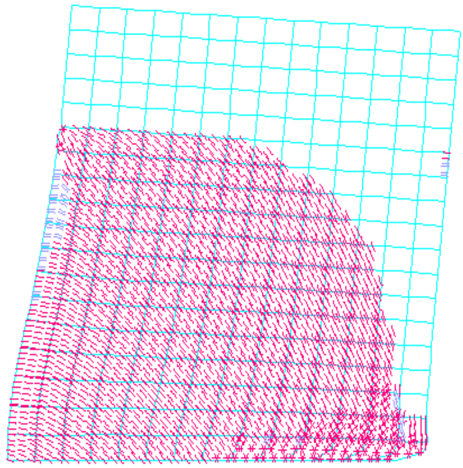

a) Deflected Shape and Crack Pattern

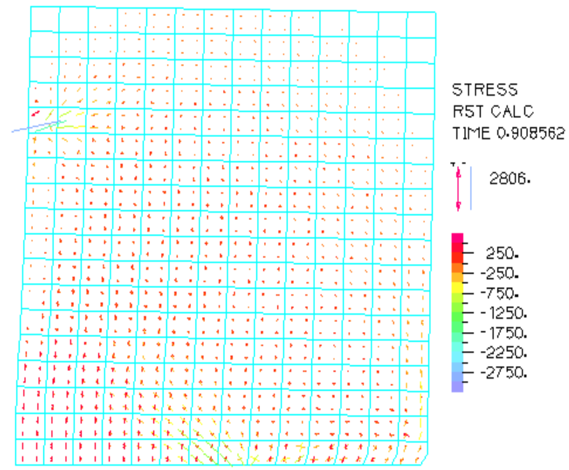

b) Masonry Principal Stresses

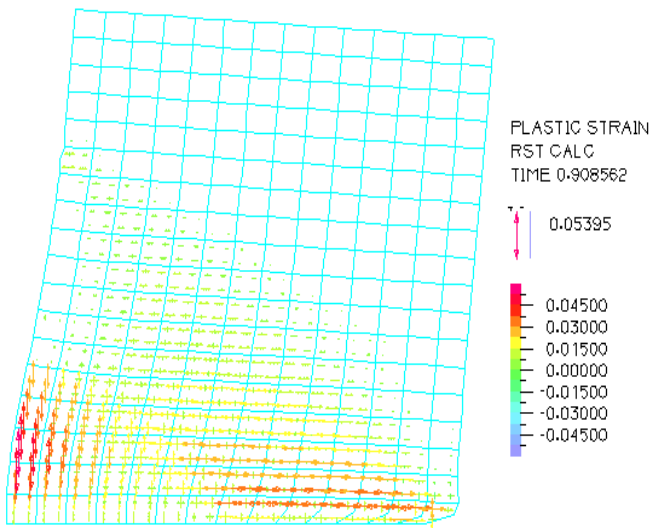

c) Steel Plastic Strain

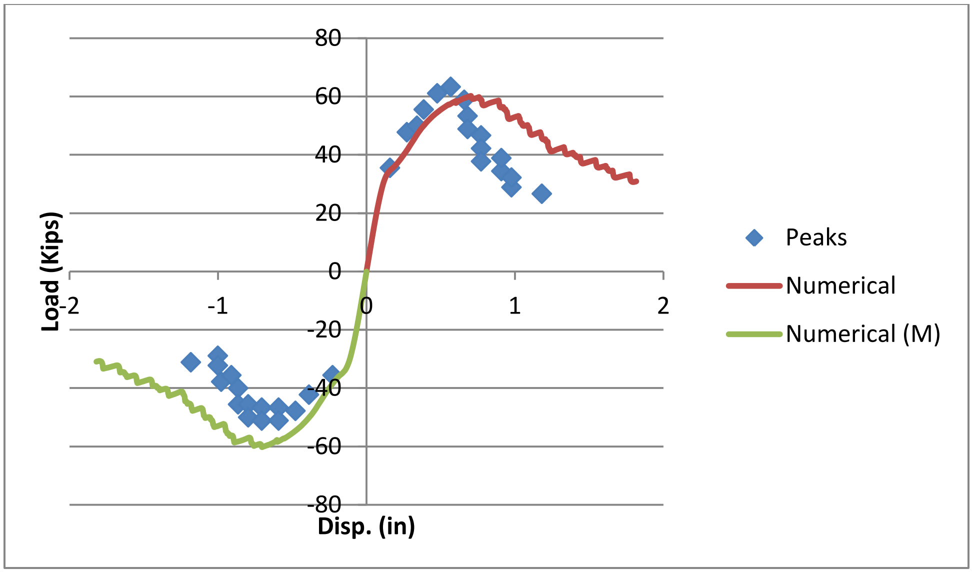

e) Comparison between FE and experimental results

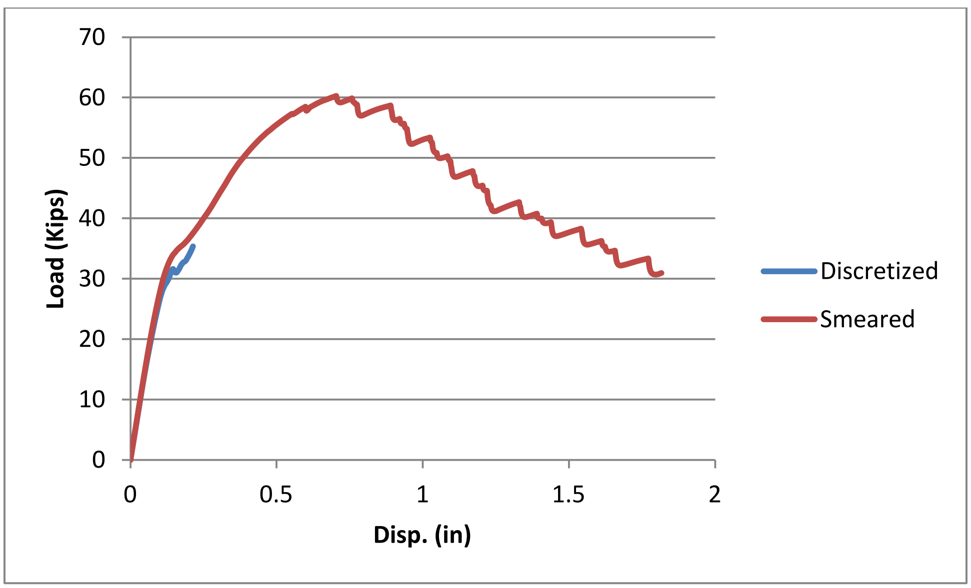

f) Comparison between FE Discretized and Smeared Models

Figure A2.13 Wall 5 (1/4 Spacing Mesh) Results

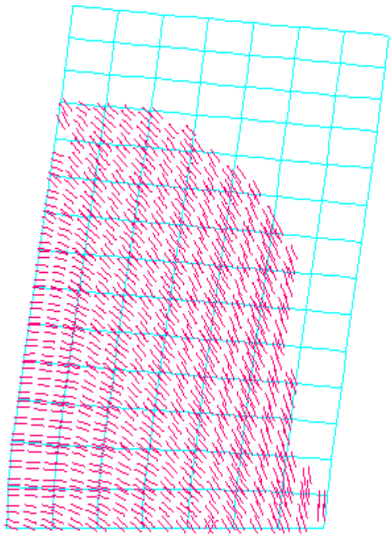

a) Deflected Shape and Crack Pattern

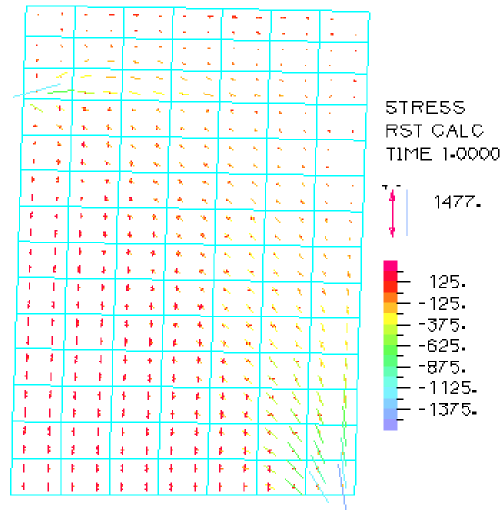

b) Masonry Principal Stresses

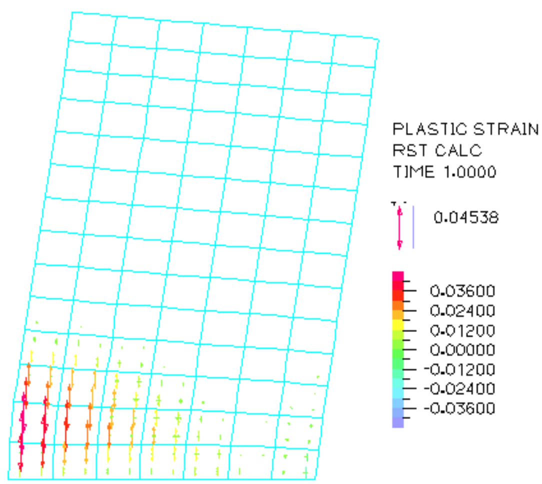

c) Steel Plastic Strain

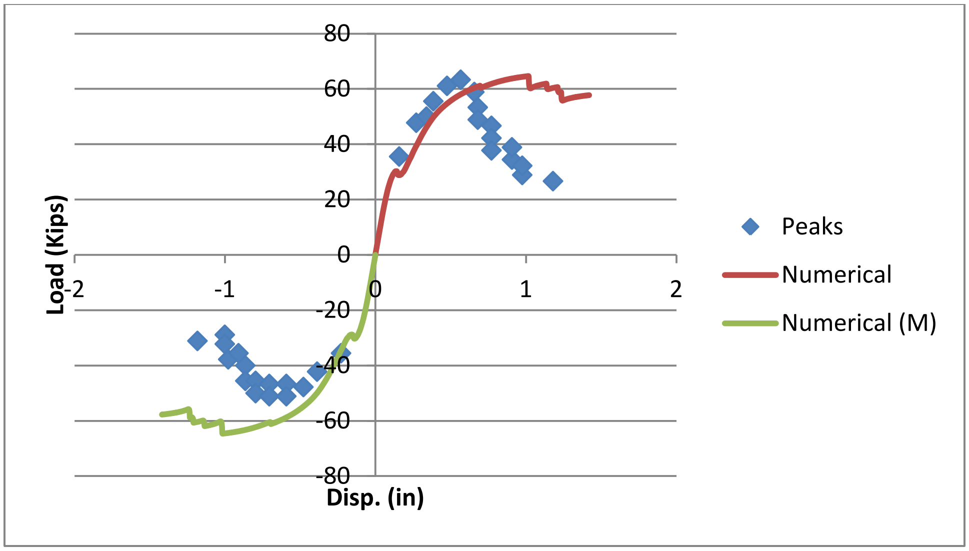

e) Comparison between FE and experimental results

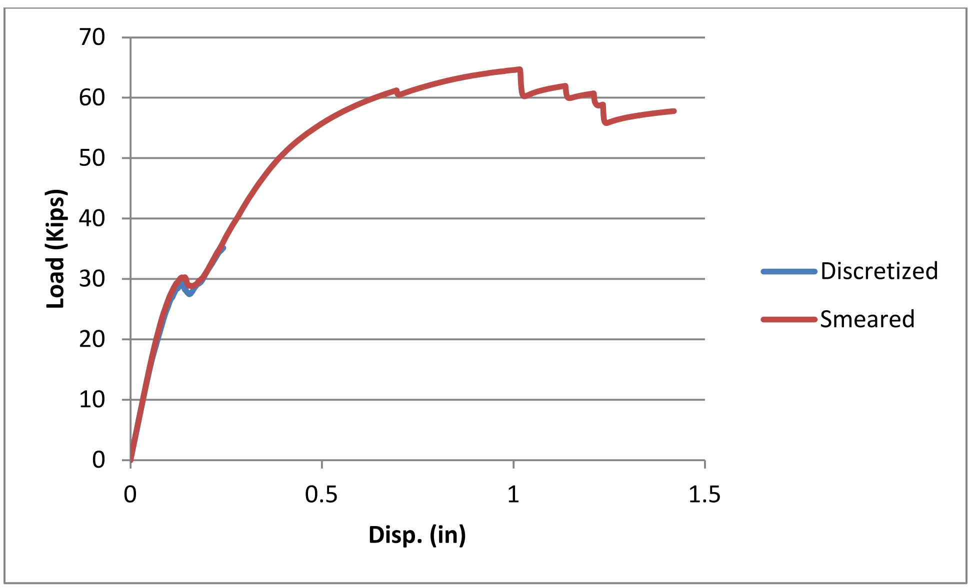

f) Comparison between FE Discretized and Smeared Models

Figure A2.14 Wall 5 (1/2 Spacing Mesh) Results

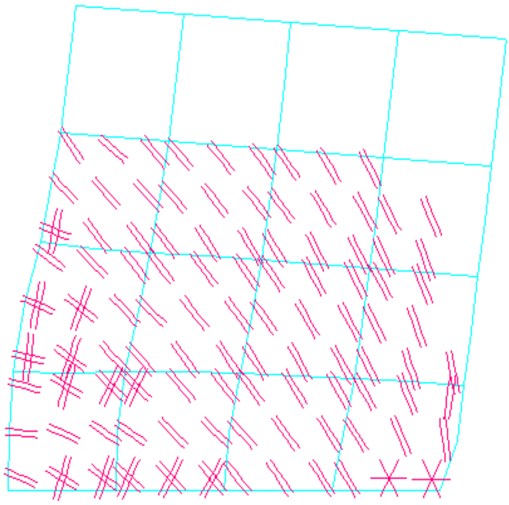

a) Deflected Shape and Crack Pattern

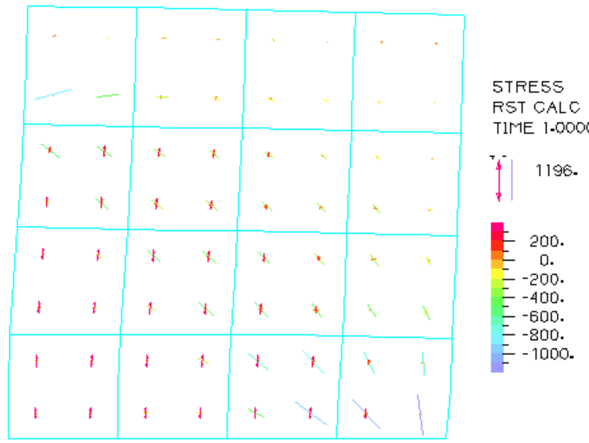

b) Masonry Principal Stresses

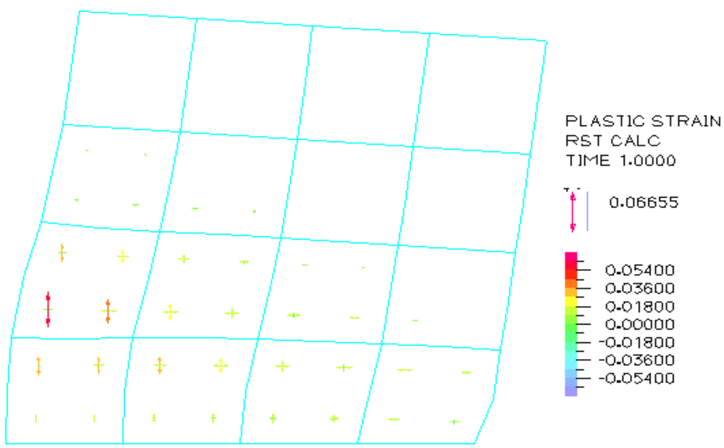

c) Steel Plastic Strain

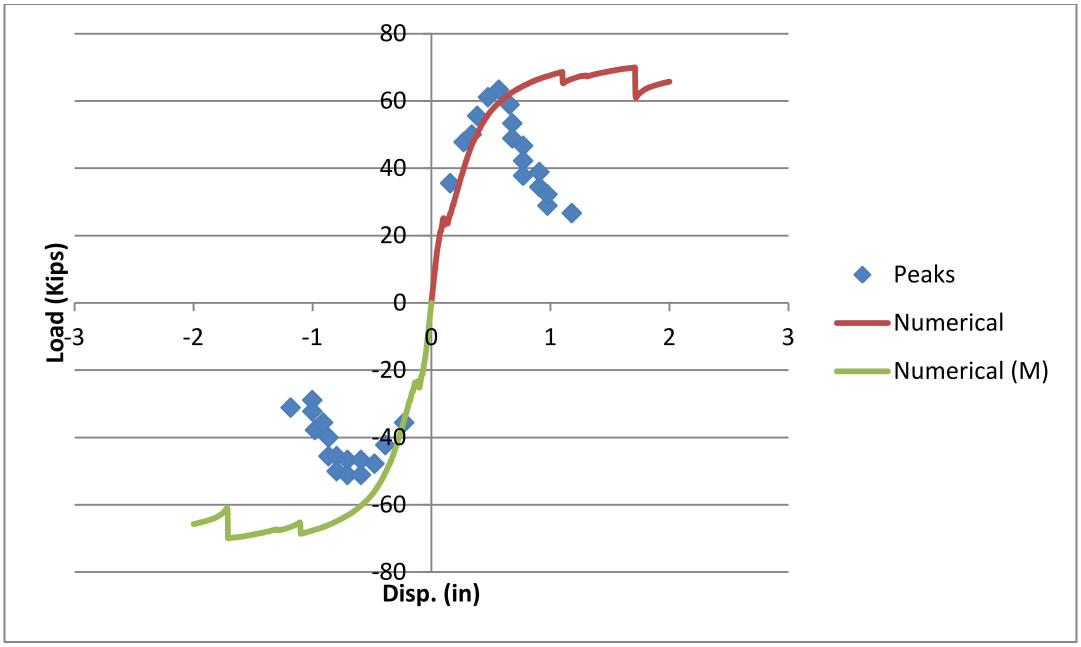

e) Comparison between FE and experimental results

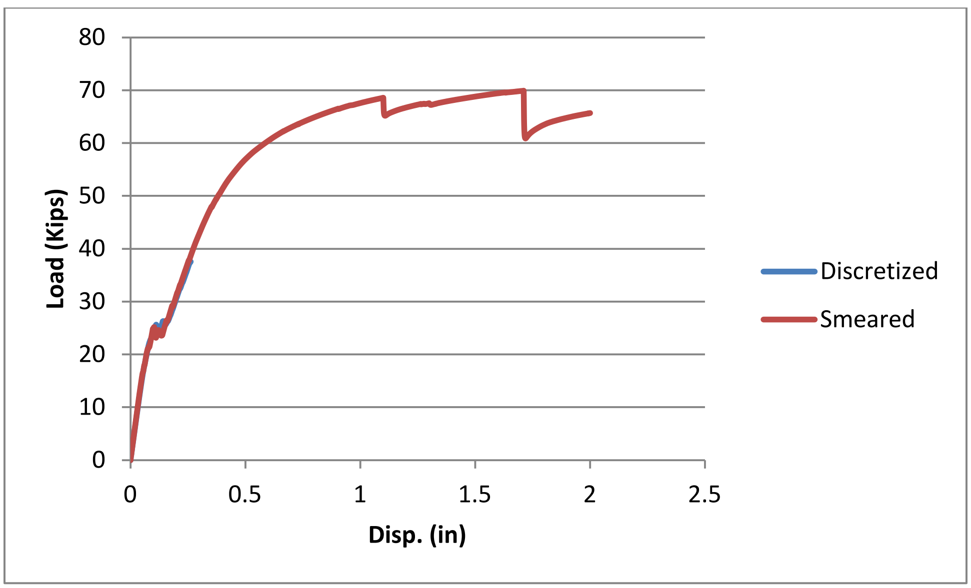

f) Comparison between FE Discretized and Smeared Models

Figure A2.15 Wall 5 (Spacing Mesh) Results

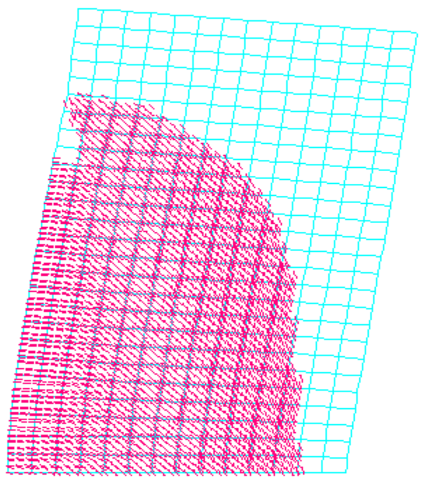

a) Deflected Shape and Crack Pattern

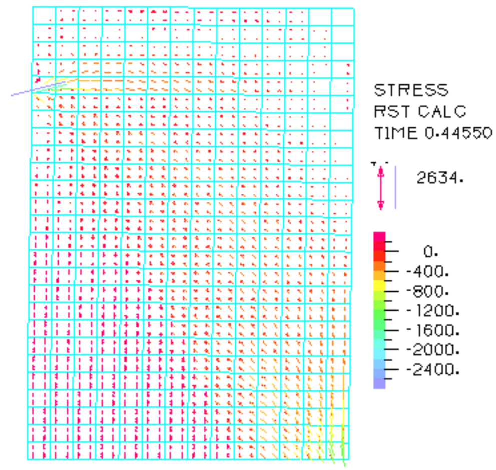

b) Masonry Principal Stresses

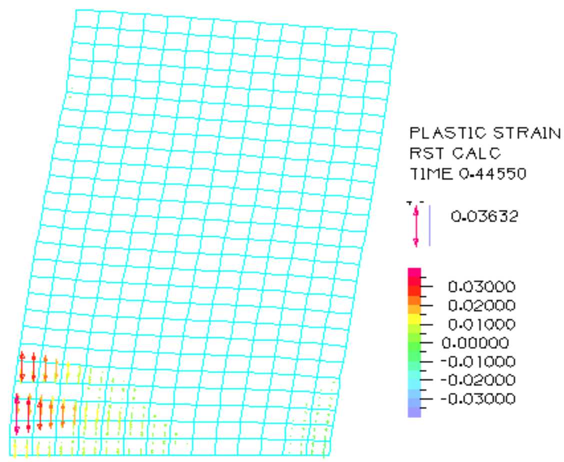

c) Steel Plastic Strain

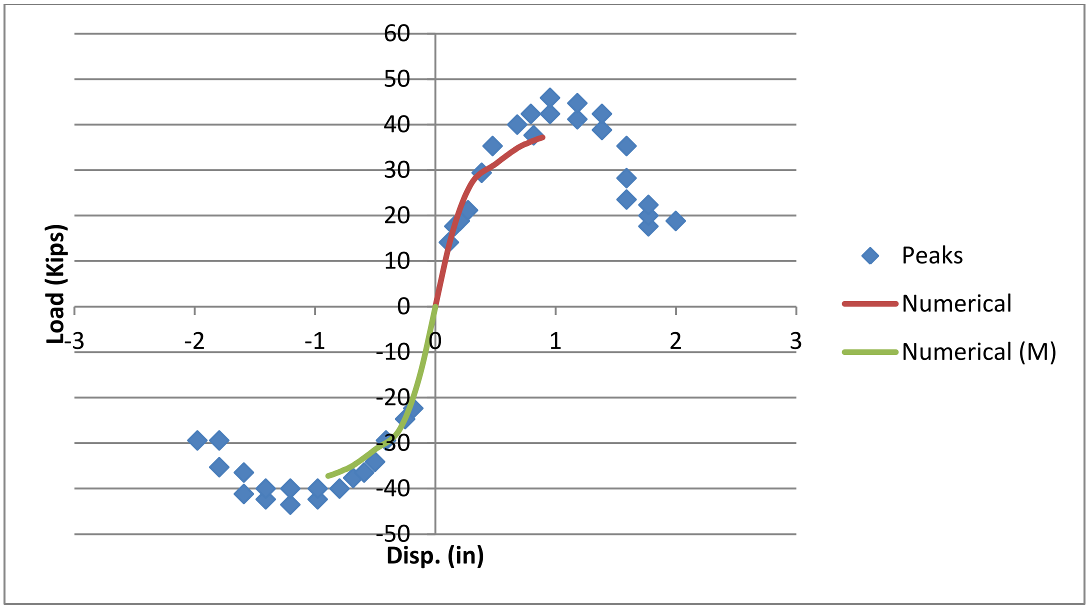

e) Comparison between FE and experimental results

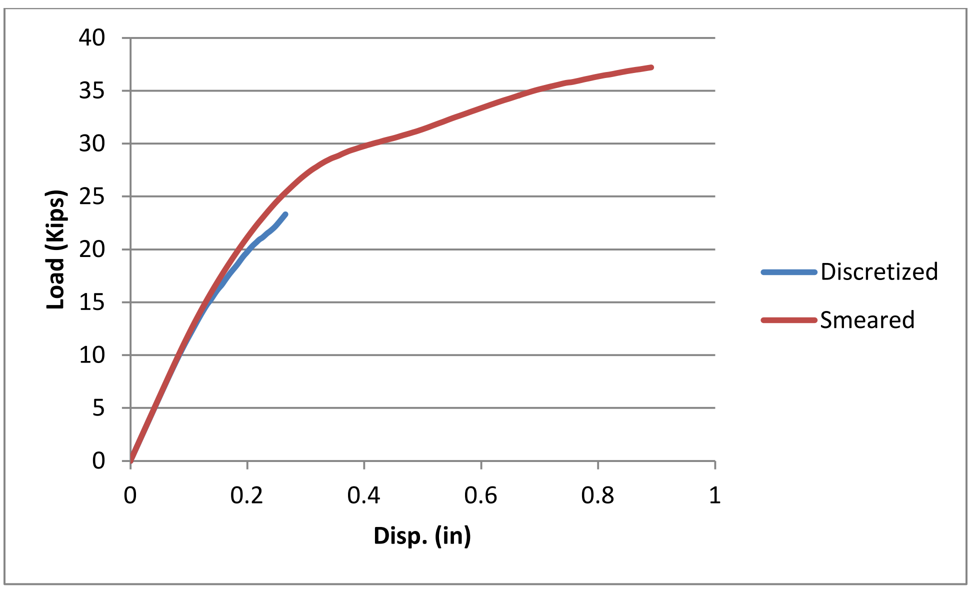

f) Comparison between FE Discretized and Smeared Models

Figure A2.16 Wall 6 (1/4 Spacing Mesh) Results

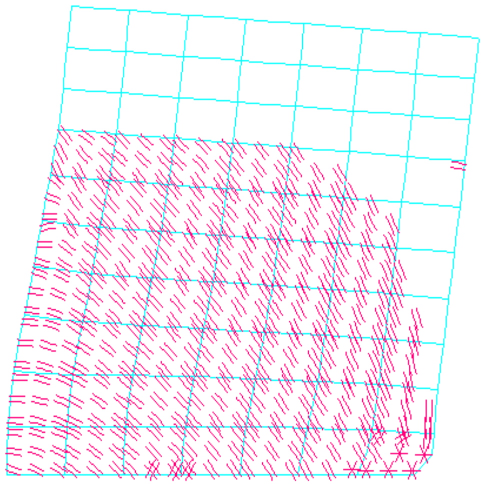

a) Deflected Shape and Crack Pattern

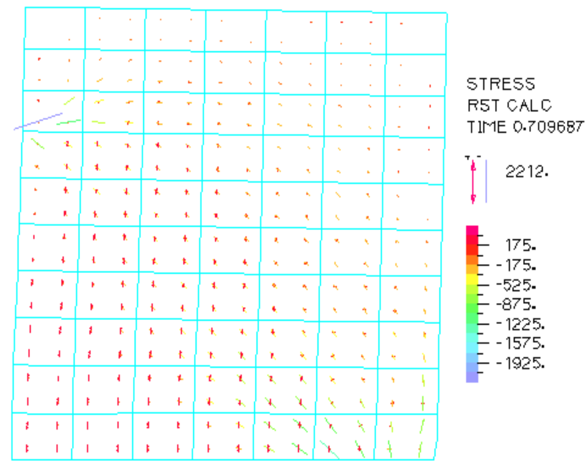

b) Masonry Principal Stresses

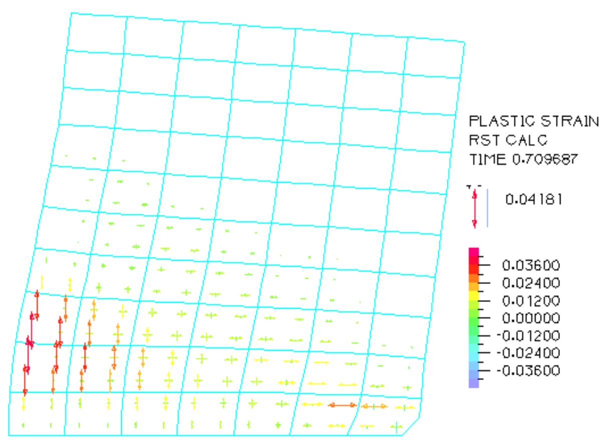

c) Steel Plastic Strain

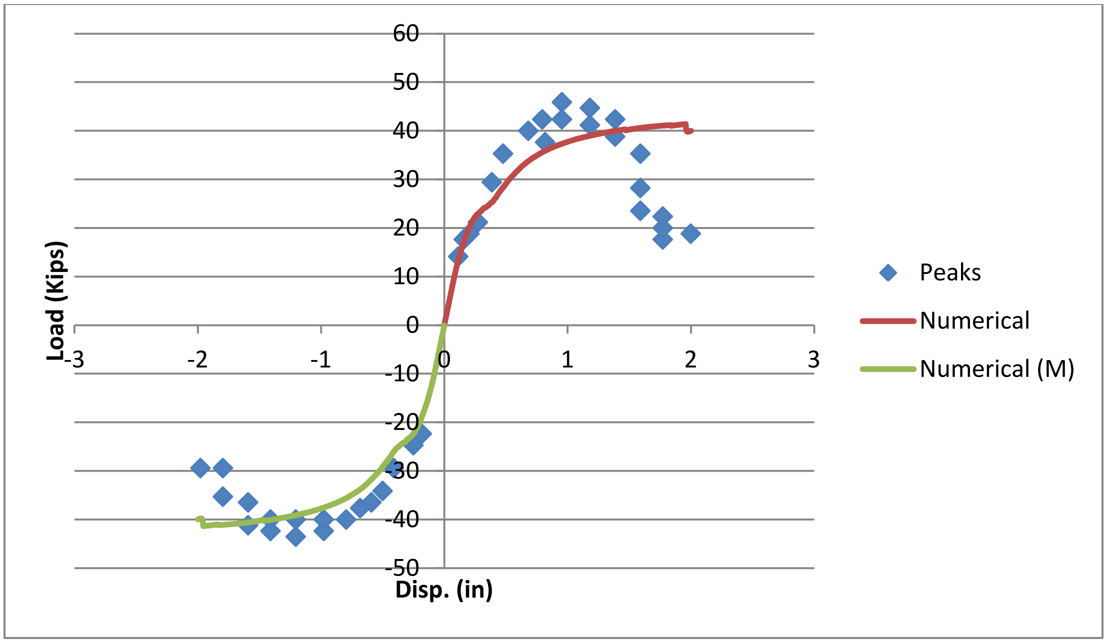

e) Comparison between FE and experimental results

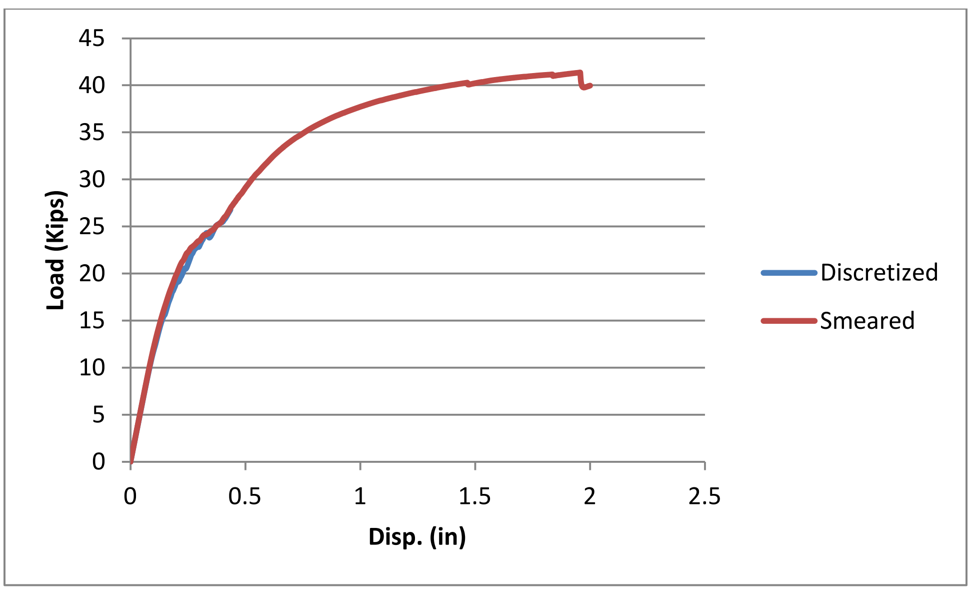

f) Comparison between FE Discretized and Smeared Models

Figure A2.17 Wall 6 (1/2 Spacing Mesh) Results

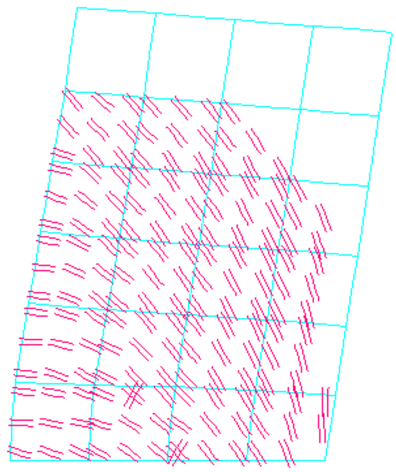

a) Deflected Shape and Crack Pattern

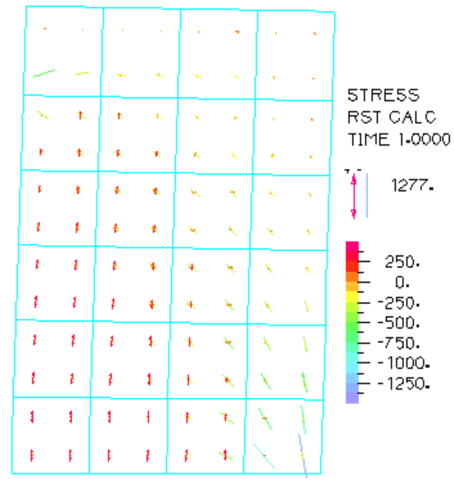

b) Masonry Principal Stresses

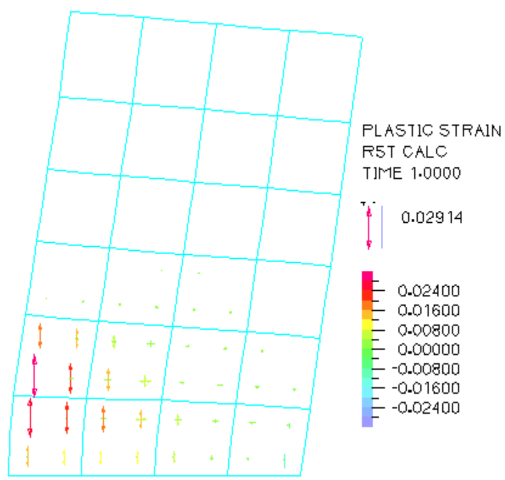

c) Steel Plastic Strain

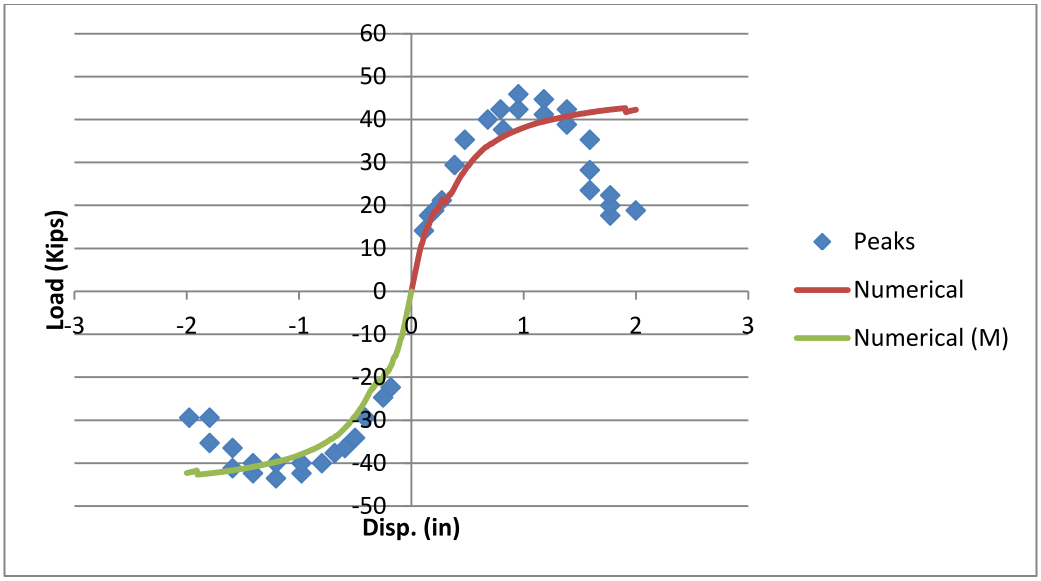

e) Comparison between FE and experimental results

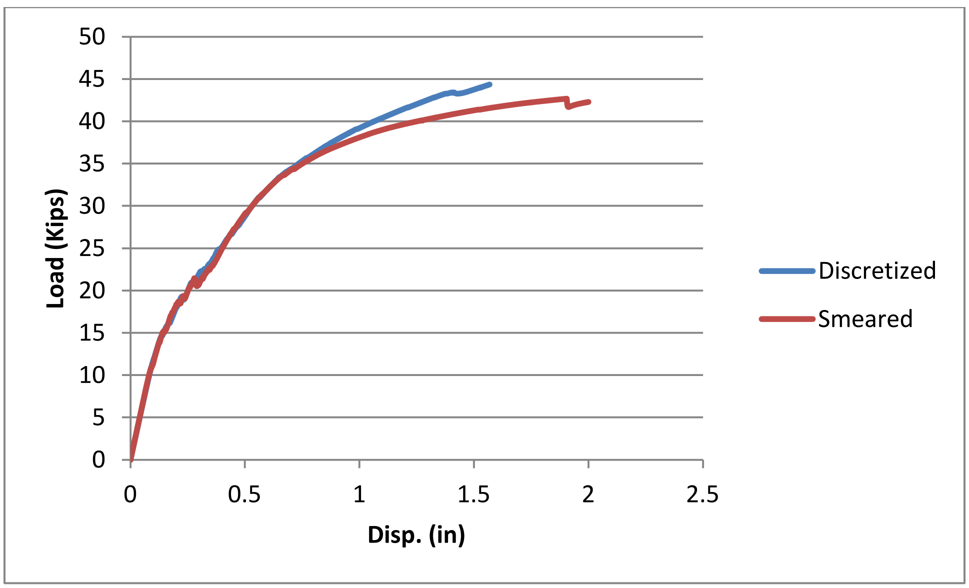

f) Comparison between FE Discretized and Smeared Models

Figure A2.18 Wall 6 (Spacing Mesh) Results

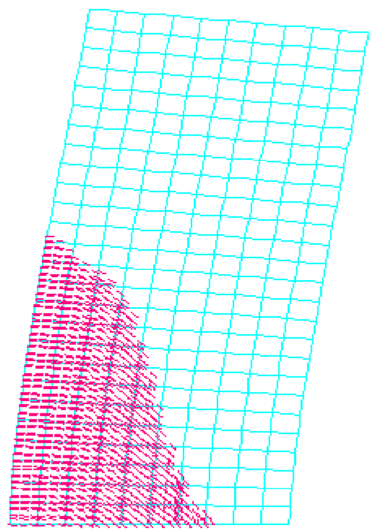

a) Deflected Shape and Crack Pattern

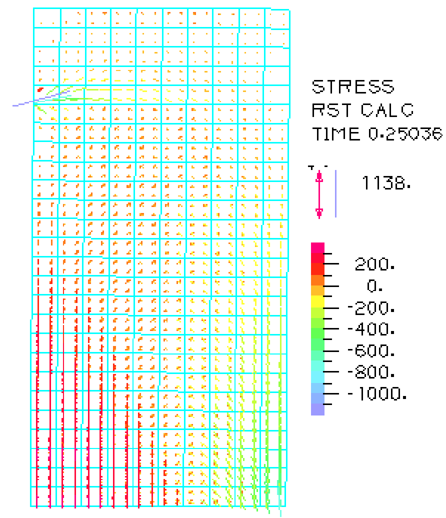

b) Masonry Principal Stresses

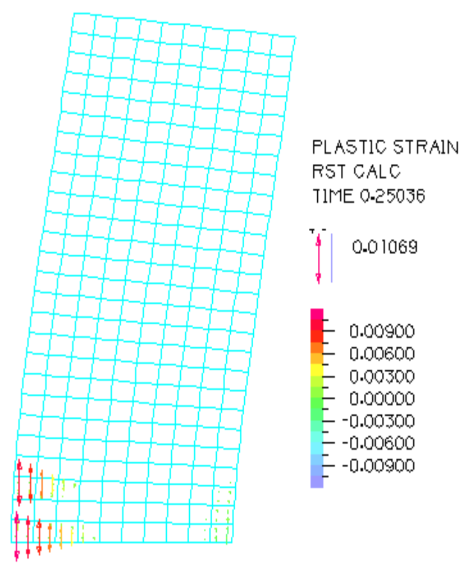

c) Steel Plastic Strain

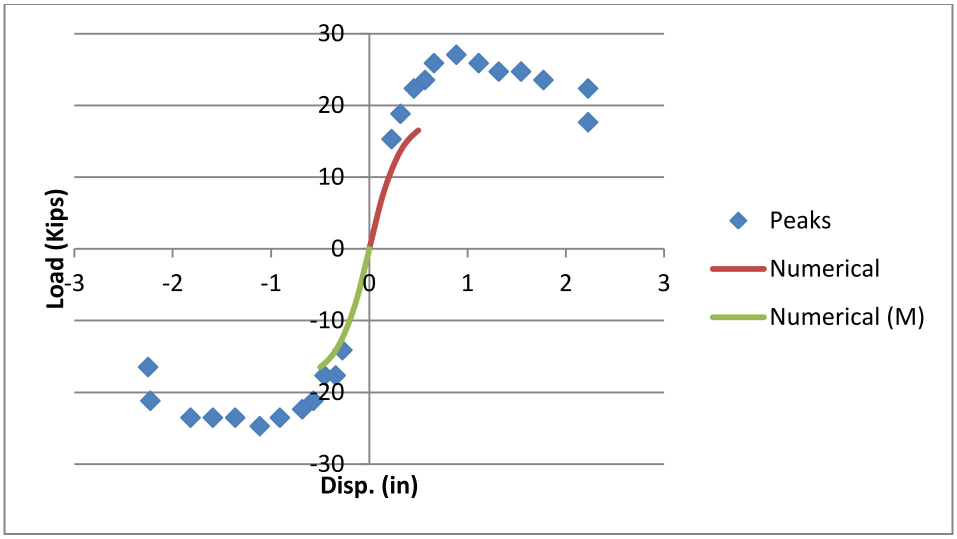

e) Comparison between FE and experimental results

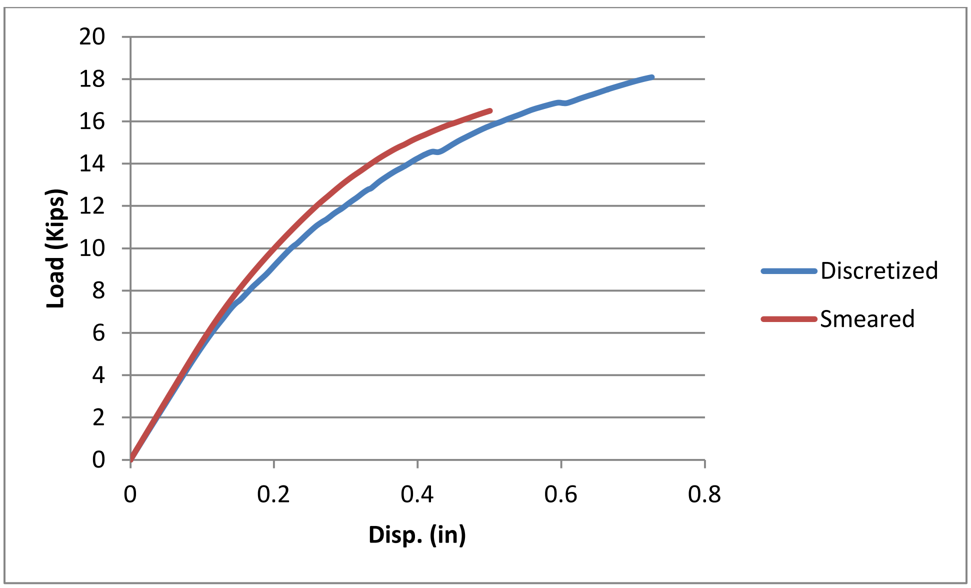

f) Comparison between FE Discretized and Smeared Models

Figure A2.19 Wall 7 (1/4 Spacing Mesh) Results

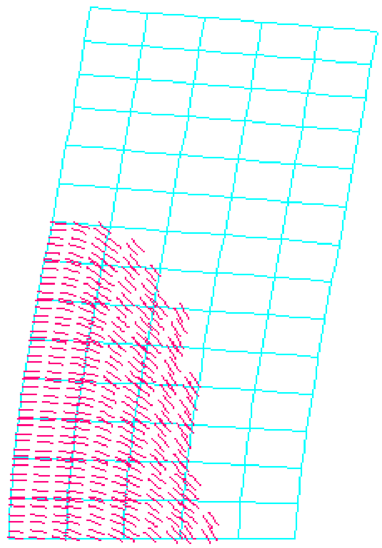

a) Deflected Shape and Crack Pattern

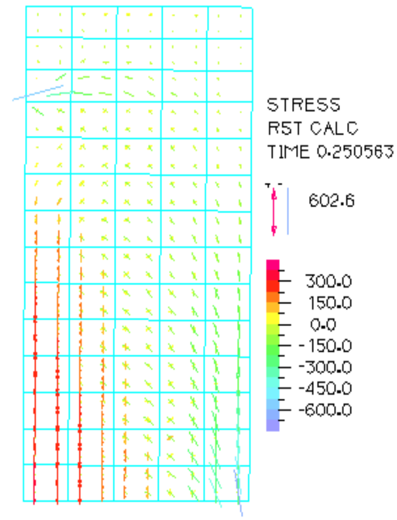

b) Masonry Principal Stresses

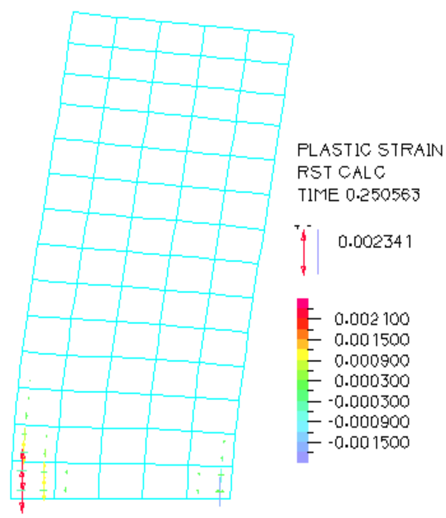

c) Steel Plastic Strain

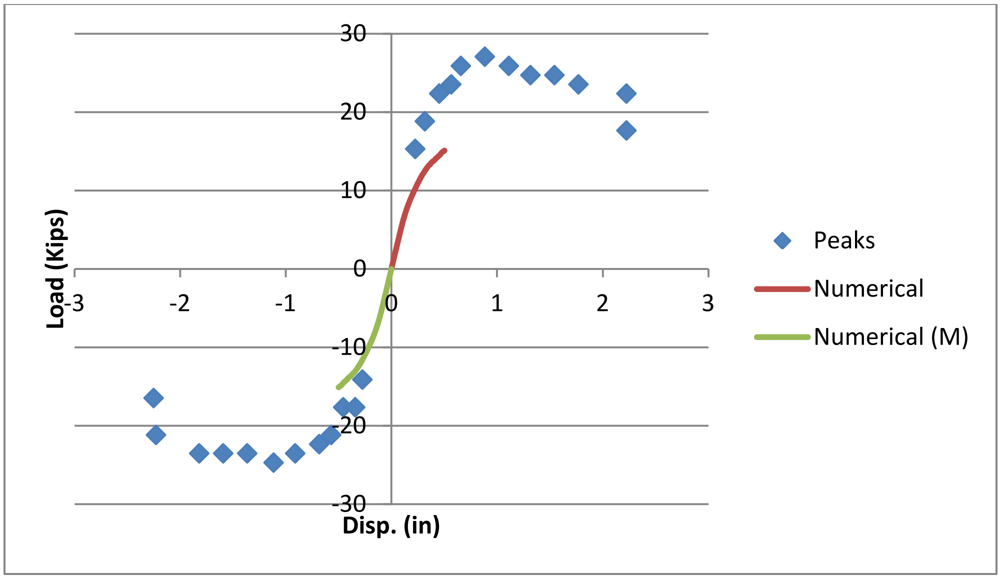

e) Comparison between FE and experimental results

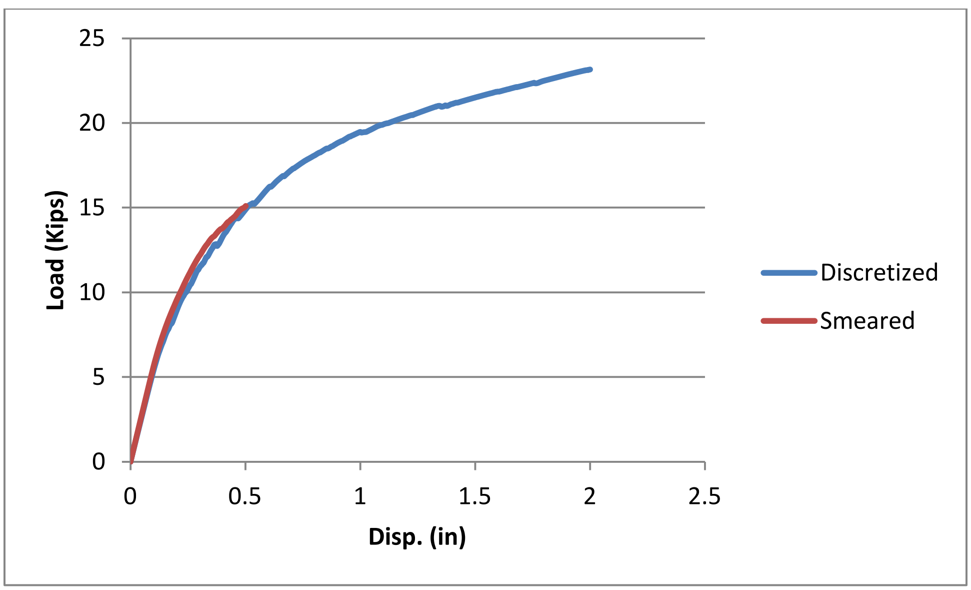

f) Comparison between FE Discretized and Smeared Models

Figure A2.20 Wall 7 (1/2 Spacing Mesh) Results

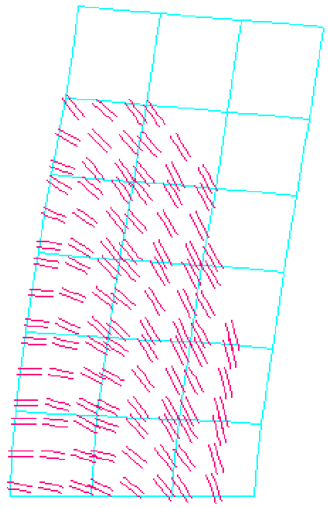

a) Deflected Shape and Crack Pattern

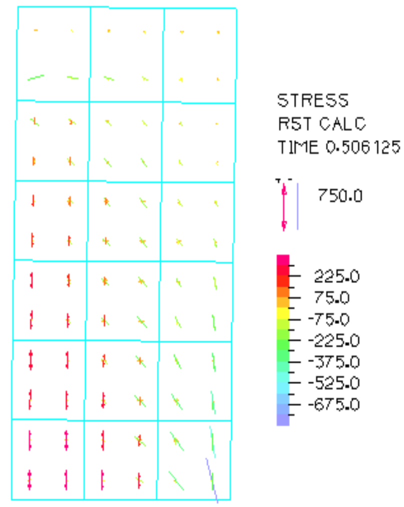

b) Masonry Principal Stresses

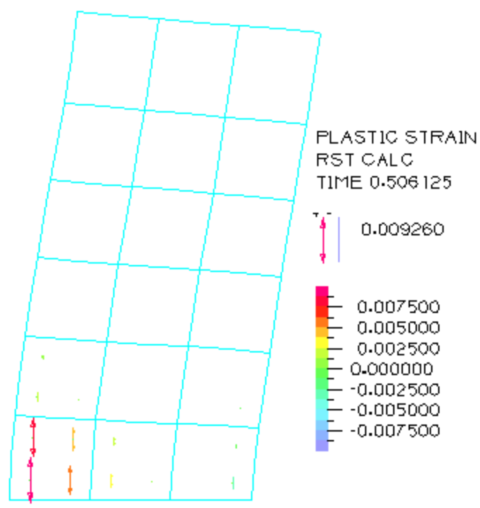

c) Steel Plastic Strain

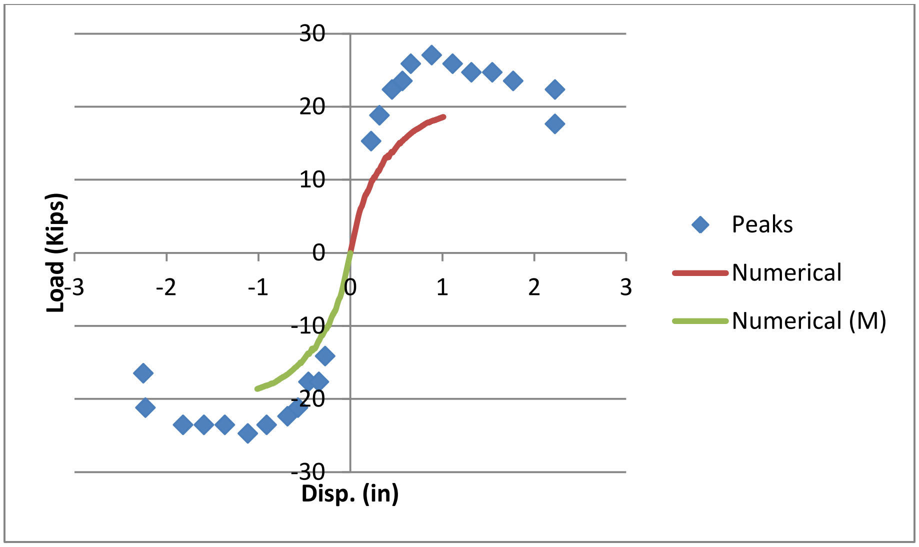

e) Comparison between FE and experimental results

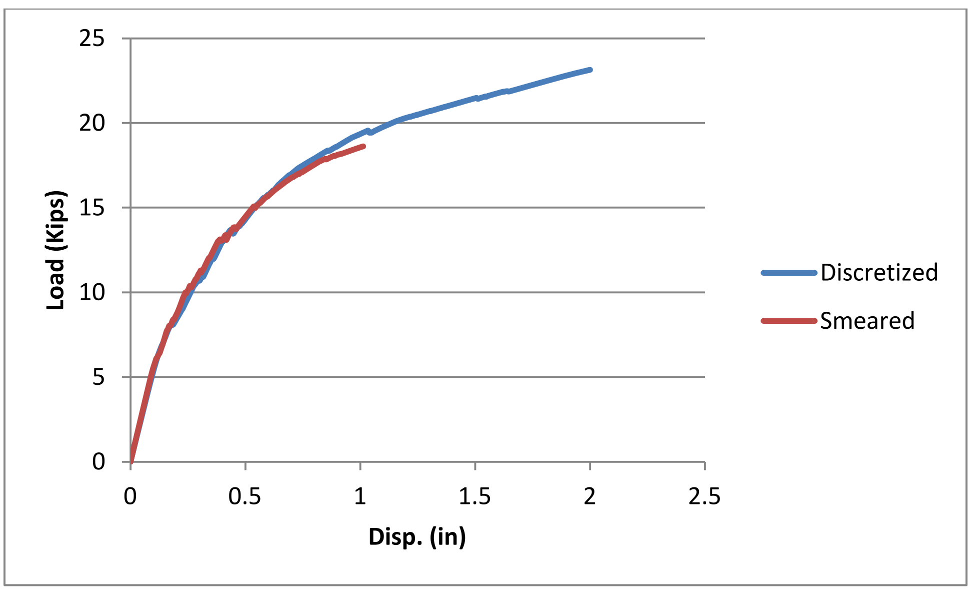

f) Comparison between FE Discretized and Smeared Models

Figure A2.12 Wall 7 (Spacing Mesh) Results

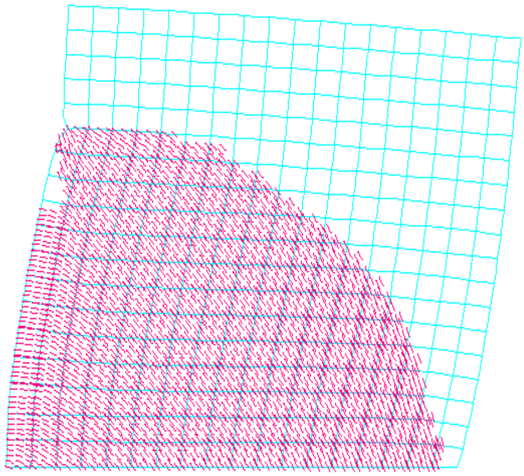

a) Deflected Shape and Crack Pattern

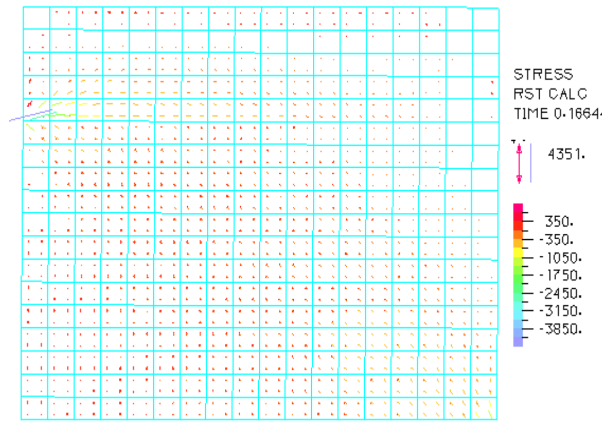

b) Masonry Principal Stresses

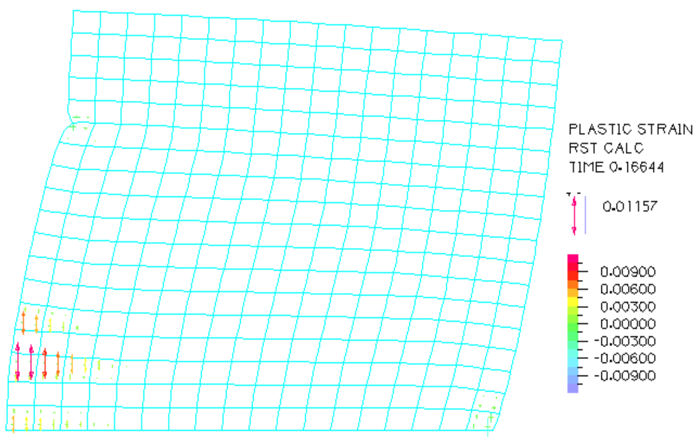

c) Steel Plastic Strain

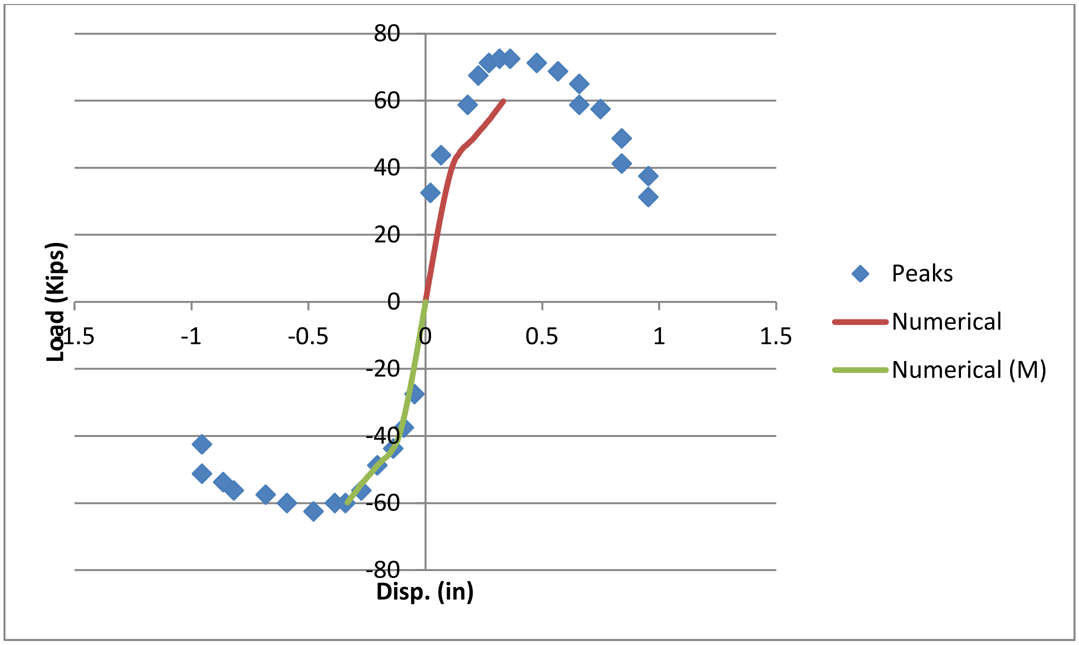

e) Comparison between FE and experimental results

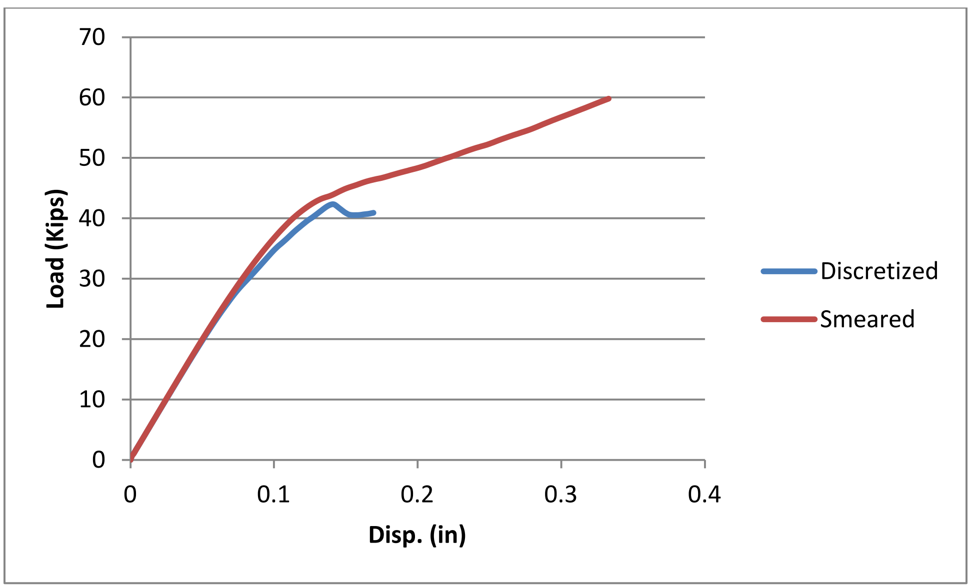

f) Comparison between FE Discretized and Smeared Models

Figure A2.22 Wall 8 (1/4 Spacing Mesh) Results

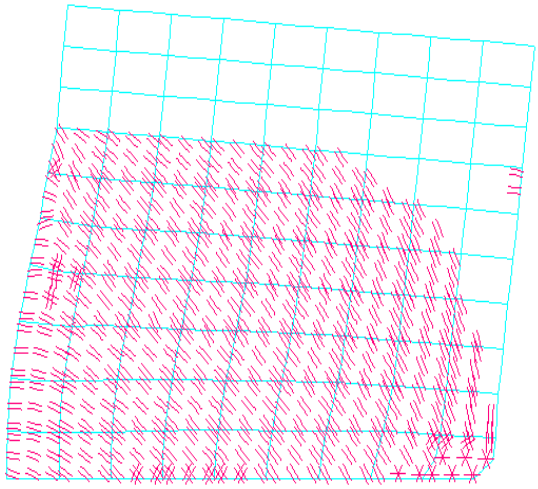

a) Deflected Shape and Crack Pattern

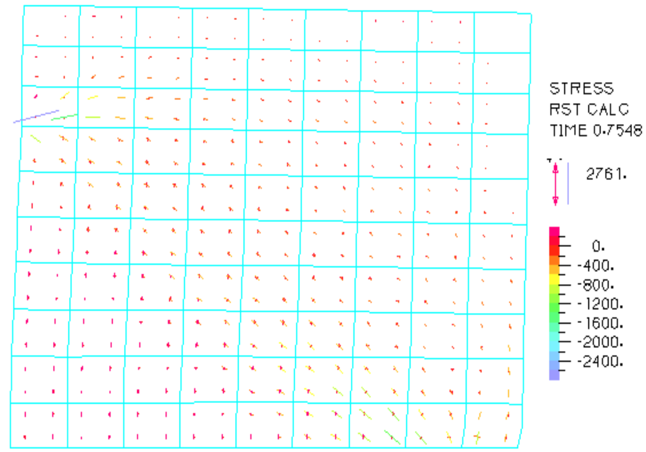

b) Masonry Principal Stresses

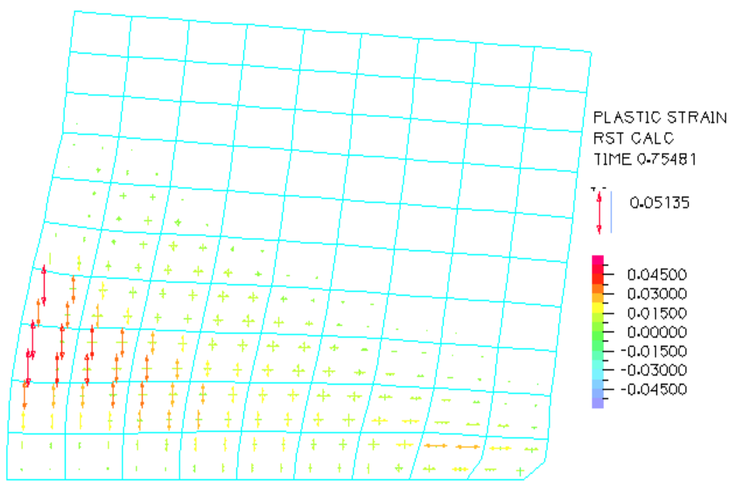

c) Steel Plastic Strain

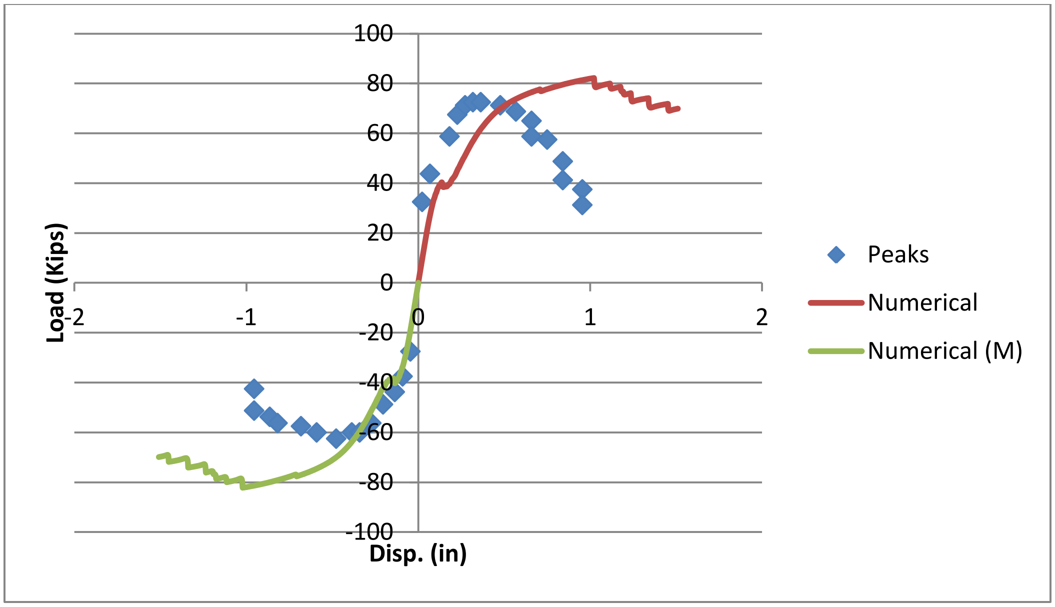

e) Comparison between FE and experimental results

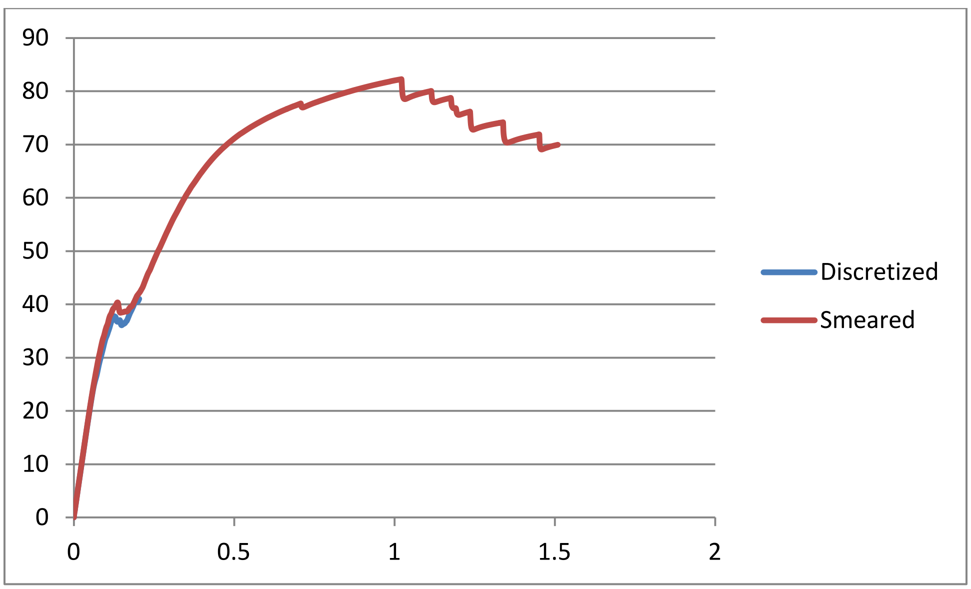

f) Comparison between FE Discretized and Smeared Models

Figure A2.23 Wall 8 (1/2 Spacing Mesh) Results

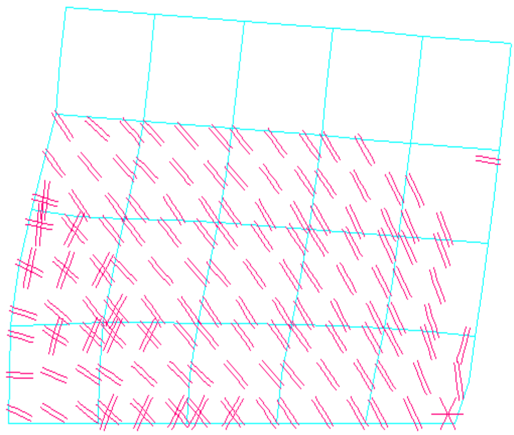

a) Deflected Shape and Crack Pattern

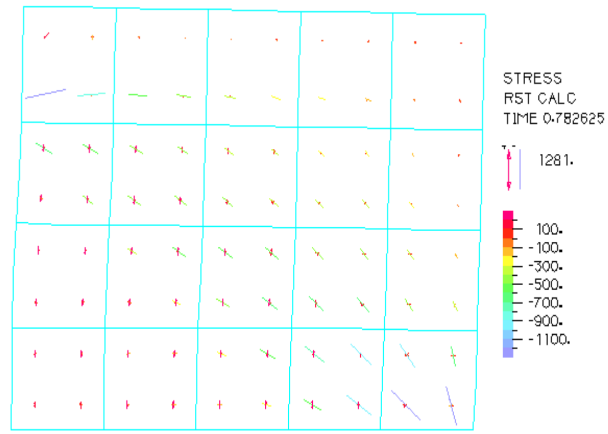

b) Masonry Principal Stresses

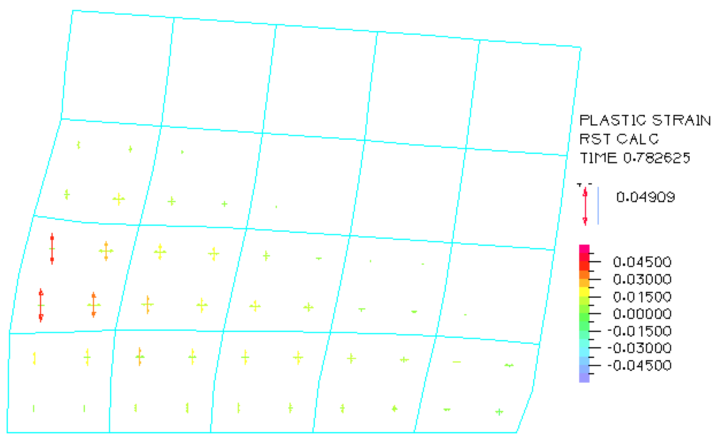

c) Steel Plastic Strain

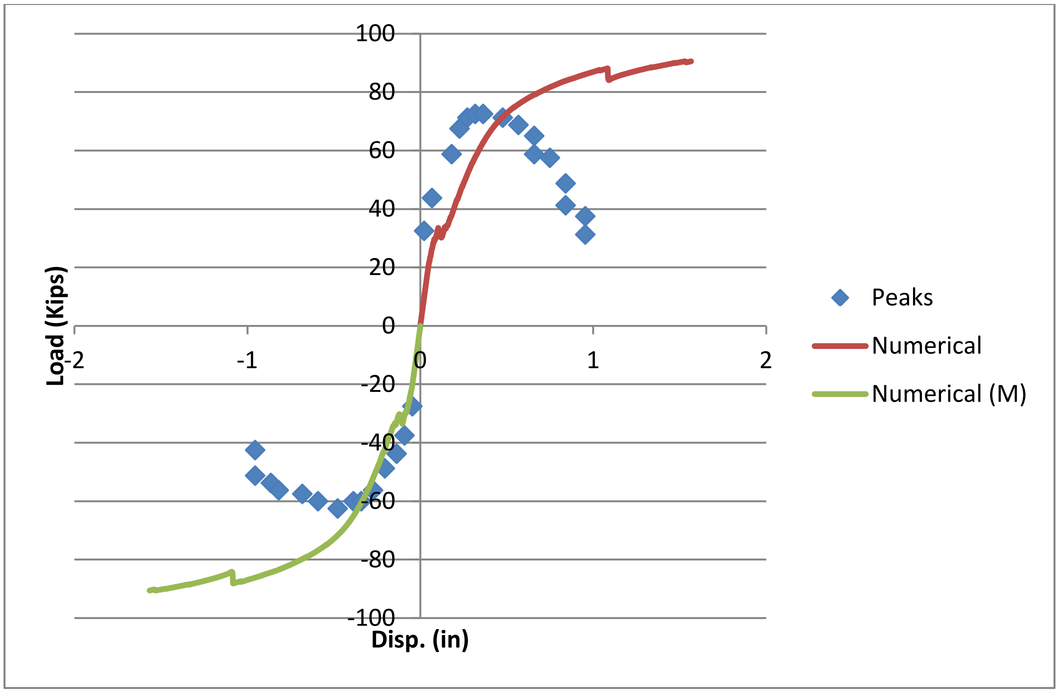

e) Comparison between FE and experimental results

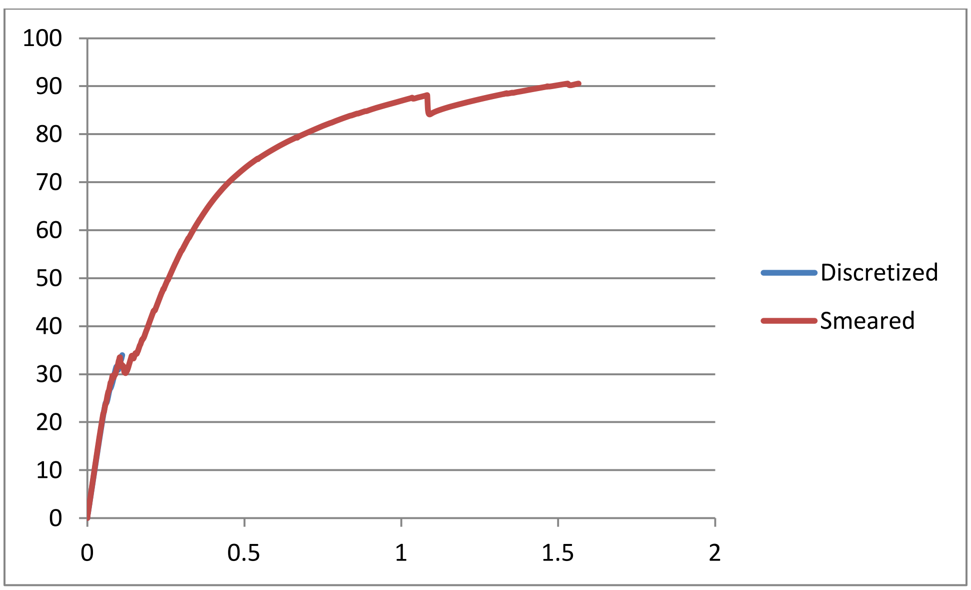

f) Comparison between FE Discretized and Smeared Models

Figure A2.24 Wall 8 (Spacing Mesh) Results